UNIVERSITAT ROVIRA I VIRGILI

FROM MONONUCLEAR TO DINUCLEAR: MAGNETIC PROPERTIES OF TRANSITION METAL COMPLEXES

Sergi Saureu Artesona

ADVERTIMENT. L'accés als continguts d'aquesta tesi doctoral i la seva utilització ha de respectar els drets de la persona autora. Pot ser utilitzada per a consulta o estudi personal, així com en activitats o materials d'investigació i docència en els termes establerts a l'art. 32 del Text Refós de la Llei de Propietat Intel·lectual (RDL 1/1996). Per altres utilitzacions es requereix l'autorització prèvia i expressa de la persona autora. En qualsevol cas, en la utilització dels seus continguts caldrà indicar de forma clara el nom i cognoms de la persona autora i el títol de la tesi doctoral. No s'autoritza la seva reproducció o altres formes d'explotació efectuades amb finalitats de lucre ni la seva comunicació pública des d'un lloc aliè al servei TDX. Tampoc s'autoritza la presentació del seu contingut en una finestra o marc aliè a TDX (framing). Aquesta reserva de drets afecta tant als continguts de la tesi com als seus resums i índexs.

ADVERTENCIA. El acceso a los contenidos de esta tesis doctoral y su utilización debe respetar los derechos de la persona autora. Puede ser utilizada para consulta o estudio personal, así como en actividades o materiales de investigación y docencia en los términos establecidos en el art. 32 del Texto Refundido de la Ley de Propiedad Intelectual (RDL 1/1996). Para otros usos se requiere la autorización previa y expresa de la persona autora. En cualquier caso, en la utilización de sus contenidos se deberá indicar de forma clara el nombre y apellidos de la persona autora y el título de la tesis doctoral. No se autoriza su reproducción u otras formas de explotación efectuadas con fines lucrativos ni su comunicación pública desde un sitio ajeno al servicio TDR. Tampoco se autoriza la presentación de su contenido en una ventana o marco ajeno a TDR (framing). Esta reserva de derechos afecta tanto al contenido de la tesis como a sus resúmenes e índices.

WARNING. Access to the contents of this doctoral thesis and its use must respect the rights of the author. It can be used for reference or private study, as well as research and learning activities or materials in the terms established by the 32nd article of the Spanish Consolidated Copyright Act (RDL 1/1996). Express and previous authorization of the author is required for any other uses. In any case, when using its content, full name of the author and title of the thesis must be clearly indicated. Reproduction or other forms of for profit use or public communication from outside TDX service is not allowed. Presentation of its content in a window or frame external to TDX (framing) is not authorized either. These rights affect both the content of the thesis and its abstracts and indexes.

Sergi Saureu Artesona

From Mononuclear to Dinuclear:
Magnetic Properties of Transition Metals Complexes

PhD Thesis

Supervised by

Dr. Coen de Graaf
Dr. Vincent Robert

Department of Physical and Inorganic Chemistry
Quantum Chemistry Group

UNIVERSITAT ROVIRA i VIRGILI

Tarragona
May 2016

UNIVERSITAT
ROVIRA I VIRGILI

DEPARTAMENT DE QUÍMICA FÍSICA
I INORGÀNICA

Campus Sescelades
Marcel·lí Domingo, s/n
43007 Tarragona
Tel. +34 977 55 81 37
Fax +34 977 55 95 63
www.quimica.urv.es

FAIG CONSTAR que aquest treball, titulat "*From mononuclear to dinuclear: Magnetic properties of transition metal complexes*", que presenta Sergi Saureu Artesona per a l'obtenció del títol de Doctor, ha estat realitzat sota la meva direcció al Departament de Química Física i Inorgànica d'aquesta universitat i que acompleix els requeriments per poder optar a Menció Internacional.

Tarragona, 4 d'Abril de 2016

Els directors de la tesi doctoral

Coen de Graaf

Vincent Robert

Agraïments

Farà cosa d'un mes, el Coen em va dir: Què us fa por del capítol de mètodes que sempre el deixeu pel final? Doncs jo em pregunto alguna cosa semblant: Què tenen els agraïments que sempre els deixem pel final? Tot i saber a qui li estic agraït i perquè ho estic, crec que feia temps que no entrava en un bucle tant difícil de superar: escriure, esborrar, escriure, esborrar... Perquè cada paraula compta, perquè de vegades em costa molt demostrar el que sento, perquè vull que tot surti gairebé perfecte (sóc d'aquells que considera que la perfecció no existeix), i perquè no m'agradaria deixar-me ningú, ni els que ja no hi són.

Comencem.

Ja han passat més de 5 anys des de que vaig començar una beca de col·laboració amb el Coen. He de reconèixer que va ser un canvi força gran, un salt de la catàlisi cap al mon del magnetisme, però les ganes constants d'aprendre que tinc, juntament amb la forma que te el Coen d'entendre el dia a dia, han fet que consideri aquesta etapa com una de les més importants a nivell formatiu i a nivell de maduresa personal. Agrair-te la confiança que has depositat en mi, la paciència que has tingut en tot moment, i sobretot, els consells que m'has pogut donar quan més ho he necessitat. També t'he de dir que ens queda pendent una sortida de *running*, ja que encara recordo com el Xavi (també et tocaran unes paraules) i tu em vàreu deixar enrere a Mulheim, quin nivell físic! Un altre cop, gràcies. Parlant del Xavi, el dia de la defensa no estarem damunt d'una bicicleta o corrent, però també et tindré davant com sempre quan fèiem les sortides, quines tardes i quines rutes! M'alegro molt d'haver compartit tantes estones d'esport i desconnexió. A la resta de gent que formen part del Grup de Quàntica, Toni, Jordi, Rosa, Mar, Poblet, Anna, Gerard, Moisés, Jose, Elisenda, sempre és d'agrair el tenir un grup de gent que facin possible les enriquidores estones a l'hora del cafè, els dinars que hem fet plegats, o si més no, que t'ajudin en petits detalls que solen aparèixer durant un camí com aquest.

Als meus companys de grup, durant aquests 5 anys hem compartit estones per a tot, tant de bones com de dolentes. Però que coi, les dolentes no cal recordar-les (per molts $ $ $ que siguin). Agrair molt el fet que la Sónia i la Jess em vinguessin a buscar a la sala de terminals per oferir-me un lloc al seu despatx, el D201. A l'Àlex per l'ajuda que em va oferir els primers mesos de tesi per resoldre els problemes que anaven apareixent, tot i estar enfeinat amb la seva defensa. A més a més, em va facilitar molt la meva adaptació al grup d'Estrasburg. Des de llavors, he tingut la sort de compartir molt bones estones amb ell (recordant també, a l'Agnès i el Salva), i junts hem demostrat que la música electrònica també crea amistats. Al Pablo, la Jess i a la Magda, són moltes hores les que hem passat dins el despatx, a més de compartir-ne unes quantes fora, sempre us tindré un record especial, això si, espero que no hem recordeu únicament pel: Què passa mestre! Magda, després de gairebé 5 anys, això ja s'acaba! Ves pensant a qui li cedeixes la comissió de l'estilisme. A la Núria i al Xavi, el glamour al grup ja no és el mateix sense vosaltres, a més us agraeixo tots els consells que m'heu donat quan ho he necessitat. Al Pablito, tot i ser merengue, hem fet moltes rises plegats xafardejant el Facebook. Laura, haurem d'anar a fer algun partidet de pàdel en breus, no?. Roser, tot i fer poc que has arribat, ja t'has fet un lloc dins el grup, sobretot, vigila'm a aquell parell!!! Marc, pel que necessitis. Hem compartit reflexions, festes, feina,… ara ens queda una gran amistat (encara que només facis que enviar fotos prenent el solete). Al Diego i l'Albert, des de que vàreu arribar, he compartit moltes estones amb vosaltres, tot i acabar, espero compartir-ne més en el futur. Sou dos tios de *p. mare* que qualsevol persona estaria encantat de tenir al costat. Tete, anant a la teteria era el nom més adient que et podia dir, cap ben alt i palante, tot es supera! I finalment a la resta amb qui he compartit algun moment, Ximo, Pep, Mariano, Jaume, Khalid, Gerard, Mercè, Montse, Juan Carlos, Gian, John, Mireia, espero que tingueu molta sort i tot us vagi molt bé en el futur.

Coen, I give you thanks for considering Strasbourg as the most appropriate place to develop the thesis stay. I spent there three superb months and I took with me a lot of good memories. Thanks to all people of the Laboratoire du Chimie Quantique of the University of Strasbourg. Vincent, thanks for offering me the possibility of starting two new projects, and also thank you for your friendship. I think that your personality is one of the most important pillars of the Labo. Emmanuel and Gabriel thanks for going with me to the Ososphère nights. Àlex (for second time) and Thiago (crazy Brazilian man), I think that both of you are excellent people, the stay in Strasbourg would not have been the same without you. And thanks to all the other people I met there, the other people of the group and some crazy people from Spain.

Als meus dos tatos de la ciutat de Tarragona. Arribar a Tarragona sent fill únic i marxar amb dos germans no ho pot dir qualsevol. Crec que sense vosaltres aquests 10 anys no haguessin estat igual. Xavier “*Monty*” has sigut un gran company de viatge. D’ençà ens vam conèixer aquell dia a la residència, he trobat en tu un veritable amic. De vegades ens hem pogut enfadar, no hem estat d’acord en algunes decisions, però t’agraeixo tot el que has fet per mi, sempre has estat allí. I Joan “*Guasch*”, crec que la vida ens tenia un espai guardat per compartir aquests anys i crear aquest vincle que tenim. El fet de viure junts ens deixa un mon ple de records, em superat obstacles personals i ens hem intentat ajudar en tot moment. La química em deixa un altre gran amic, en el qual he pogut, i hi podré confiar, tant en els bons com en els mals moments, n’estic ben segur. Lore, la *bussiness* woman del grup, hem compartit molts bons moments, i ens hem aconsellat mútuament per tal d’actuar de la millor manera possible en cada situació. No oblidar-me dels altres *qumifabulosos*, el Pau i Ribo, amb els quals he tingut l’oportunitat de compartir pis i veritables aventures.

No vull deixar-me els meus amics de la Terraferma. Joel, Dídac, Alfo, Edu, Simón, Caubet i Farré, us agraeixo cada una de les mostres de suport que he rebut en els moments que pitjor ho he passat. Se que darrerament no he pogut reunir-me tant amb vosaltres, però us tinc present en tot moment! Tenim una colla difícil de superar i això ens fa molt grans.

En moments així, sempre penses en si t'has deixat algú. Crec que a qui li he d'estar agraït, ja ho sap. Disculpeu-me si no us he mencionat.

I a la meva família. Mare, gràcies per tot el que m'has donat i per la capacitat de lluita que m'has inculcat. Ja sé que de vegades sóc un desastre i no et demostro les coses, però et dec molt, perquè gràcies a tu, estic aquí. A la resta de la família, gràcies pels dinars que fem plegats i pels consells que em neu donant cada vegada que ens veiem. A tu, Alba, gràcies per recolzar-me i fer-me aixecar cada vegada que caic, gràcies per conviure amb mi el dia a dia, per haver deixat que et conegués, i el més important, per la paciència que tens amb mi. Ja ho saps, junts serem invencibles, i superarem tota dificultat que se'ns fiqui davant. I finalment, als que no hi son, Padrí, Pare i Joan, aquest llibre també és per vosaltres, perquè m'hagués agradat entregar-vos-el en mà, espero que estigueu orgullosos de mi. Un petó, on sigueu.

"Ever tried. Ever failed. No matter.
Try again. Fail again. Fail better."

— Samuel Beckett

Contents

CHAPTER 1

Introduction

The study of magnetic interactions in molecular systems has been subject of an intense interdisciplinary effort over the last decades [1–4]. Particularly important in this field of research are spin-crossover (SCO) systems [2, 4] and molecule-based magnets [1, 3, 5] in the different variants ranging from extended one-dimensional single-chain magnets [3, 6], via discrete polynuclear single molecular magnets [7–9], to the more recent single-ion magnets, which only possess one magnetic center [10, 11]. SCO materials and molecule-based magnets are not only interesting from the fundamental point of view of understanding complex electronic structures but also for their technological applications which include medical devices, loudspeakers, microphones, sensors, nano-switches conductors or memory devices, among others [4, 6, 12–14].

One of the most important aspect of these technological applications is the appearance of a bistability, that is, the existence of two stable electronic states preferably under the same external conditions such as temperature, pressure or other external perturbations. Therefore, the synthesis of systems with bistability under standard conditions for which switching is fast and both states are sufficiently long-lived (*i.e.*, persistent) has become increasingly important over the last 50 years. In this area of research, the interconversion between two different spin states that can be triggered by light irradiation is especially important [15–23]. The bistability in molecular magnets involves the M_S components of a given spin state and the population of the bistable states can be controlled by the application of an external magnetic field. Unfortunately, the highest temperature for which bistability has been observed in

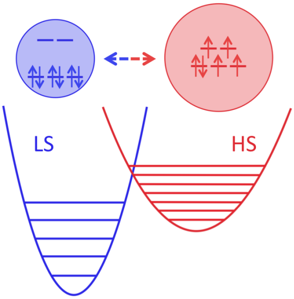

Figure 1.1: Schematic representation of the electron distribution of a $3d^6$ electronic configuration in a (quasi-)octahedral SCO complex.

molecular magnets is not much larger than 35 K [24–28].

1.1 Spin-crossover Systems

The spin crossover (SCO) phenomenon is rather common in compounds with transition metals (TM) of the first series with $3d^4$ to $3d^7$ electronic configurations and can be explained qualitatively by ligand-field theory and Tanabe-Sugano diagrams [29–36]. Depending on the strength of the field exerted by the ligands, the d-electrons of the TM can exhibit a high-spin (HS) electronic configuration at low ligand-field strengths or a low-spin (LS) configuration at higher ligand-field strength (see Figure 1.1).

A large number of SCO complexes known to date contain Fe^{2+} in a $3d^6$ electronic configuration surrounded by six N atoms in a

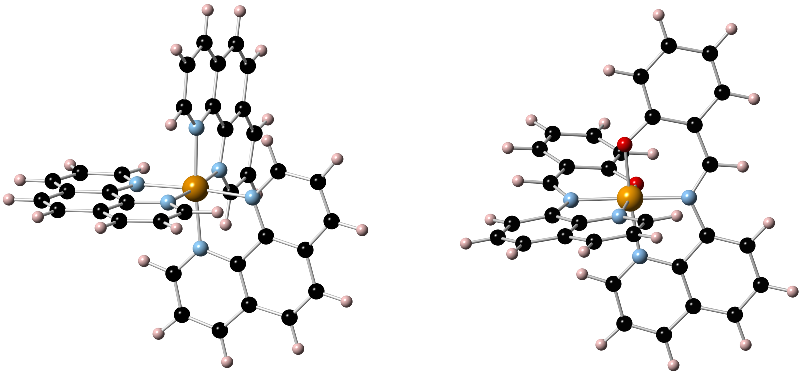

Figure 1.2: Ball and stick representation of typical SCO complexes of Fe(II), $[Fe(phen)_3]^{2+}$ (left), and Fe(III), $[Fe(qsal)_2]^{+}$ (right). Color code: orange for Fe, red for O, black for C, blue for N and pink for H.

quasi-octahedral coordination sphere. Let us mention that SCO is also observed in Fe^{3+} ($3d^5$) complexes, mostly with a N_4O_2 quasi-octahdedral environment (Figure 1.2). For Fe^{2+}-based complexes, the LS electronic state is a $^1A_{1g}$ ($t_{2g}^6e_g^0$) state and the HS state corresponds to a $^5T_{2g}$ ($t_{2g}^4e_g^2$) state. This changes to $^2T_{2g}$ ($t_{2g}^5e_g^0$) and $^6A_{1g}$ ($t_{2g}^3e_g^2$) for the LS and HS states of the Fe^{3+} complexes[1]. For both types of complexes, spin transition is accompanied by a substantial elongation of the metal-ligand bond lengths produced by the transfer of two electrons from the nonbonding t_{2g} orbitals to the antibonding e_g orbitals during the transition. This expansion of the coordination sphere is in most cases the dominant geometrical change although other distortions can also play a role [30].

---

[1] Symbols of the octahedral symmetry group are used because the quasi-octahedral coordination is maintained during the whole SCO process.

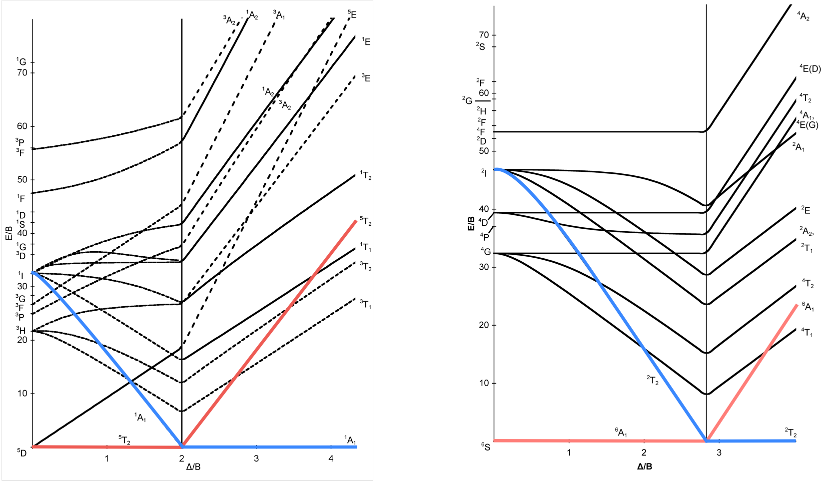

Figure 1.3: Tanabe-Sugano diagrams for d^6 configuration (left) and d^5 configuration (right) [33–35]. LS state is coloured in blue and HS state is coloured in red.

The Tanabe-Sugano diagrams of Figure 1.3 represent the relative energies of the d^5 (right) and d^6 (left) electronic configurations as function of the ligand-field strength expressed in Δ/B ratio. Here, Δ is the difference between the e_g and t_{2g} orbital energies and B is the Racah parameter for the repulsion among the d-electrons. At zero ligand-field (that is, the free ion case), the ground state is HS, sextet or quintet, following Hund's rule of maximum multiplicity. By placing the Fe^{3+} and Fe^{2+} ions in an octahedral field, the atomic Russell-Saunders terms are split and their energies evolve as shown in Figure 1.3. In the one-electron reasoning of the Tanabe-Sugano diagrams, this can directly be ascribed to the increasing difference of the energies associated with the 3d-orbitals. For strong fields, this splitting becomes so large that it is more favourable to pair the electrons in the lower d-orbitals and loose part of the exchange interactions. Hence, any SCO complex necessarily needs to have a ligand-field close to this turning point such that subtle changes induced by external perturbations can inverse the stability of the LS and HS states. However, during the spin transition, the Fe-N and Fe-O distances change, increase by 0.2 Å, and therefore Δ (parameter of the ligand field strength) is reduced, these changes also imply a conversion of LS to HS. Finally, SCO phenomenon results from the competition of mono-electronic and bi-electronic contributions and their modulation by means of structural changes.

Pressure-induced SCO

The easiest variant of SCO is the one induced by applying pressure on the sample. Starting with a HS ground state, the application of pressure compresses the structure leading to shorter metal-ligand bond lengths. This increases the ligand-field strength and for a given pressure, the LS state becomes lower in energy and a spin transition occurs. One example is the spin transition observed in the iron perovskite $CaFeO_3$ [37]. At ambient pressure and room temperature, the formally Fe^{4+} ions have a quintet ground state with four unpaired electrons but at pressures of approximately 30 GPa two electrons pair in a low-lying Fe-3d orbitals and the spin multiplicity of the ground state changes to triplet. A similar phenomenon was observed in $LaCoO_3$ [38], which changes from triplet to singlet when a pressure of 4 GPa is applied.

Thermal SCO

The description of SCO induced by temperature changes is slightly more involved since this process is entropy-driven [2, 4]. Apart from a very small thermal expansion, temperature changes do not directly affect the structure of the material, and therefore, the ligand-field strength hardly changes with temperature. However, the entropy is a temperature-dependent property and favors the HS state because of the higher spin degeneracy and the softer vibrational modes with respect to the LS state. A material that is LS at low enough temperature may eventually have a HS ground state when the temperature is raised due to increasing entropy contributions. In order to observe this thermal SCO, it is of course necessary that the LS and HS are nearly degenerate, that is the ligand field should be close to the crossing point of HS and LS in

Figure 1.3. Thermal SCO has a long standing history. In fact the first observation of thermal SCO was reported by Cambi in 1931 [39], surprisingly enough for an Fe^{3+} complex. The first member of the now prototypical Fe(II)N_6 family was described thirty years later with the discovery of SCO in Fe(phen)$_2$(NCS)$_2$ [40–43], one of the most studied SCO complexes [44–49]. Ever since, a huge amount of hexacoordinated Fe(II) and Fe(III) complexes has been synthesized and their magnetic properties have extensively been studied [2, 4, 50–53] . More recently, attention is shifting towards other metals and coordination modes [54].

LIESST

The third variant of SCO is the one induced by irradiation with light, faster and easier to control than the previous two SCO processes, but difficult to achieve at room temperature [55, 56]. It was discovered by McGarvey and Lawters [57] and Decurtins and co-workers [58] and shortly afterwards qualitatively explained by Hauser [59]. In the case of Fe(II) complexes, light irradiation induces metal centered or metal-to-ligand electronic transitions. The resulting excited state with singlet spin coupling decays through two intersystem crossings to a meta-stable quintet state accompanied by an expansion of the coordination sphere of the Fe(II) ion. If the experiment is performed at low enough temperature, the system is trapped in the HS state. This is the reason why this type of SCO is usually referred to as light-induced excited spin state trapping (LIESST). Whereas the HS state has lifetimes that range from hundreds of picoseconds to several days, the deactivation from excited singlet to HS state is extremely fast, typically on the order of 100 femtoseconds. This is one of the reasons why more than twenty years after its discovery, LIESST effect is still at the very center of the SCO research. The advances in short pulsed lasers enables researchers to extract information on the deactivation mechanism [15–23] and theoretical studies also contributed to the understanding of LIESST in octhedral Fe(II) complexes [60–62]. For Fe(III) complexes, the light irradiation induces ligand-to-metal charge transfer transition (LMCT). The decay process to the HS state is not well-known because of the lesser interest on Fe(III) complexes, due to the low efficiency of LS-HS conversion. Much less is known about the light-induced SCO in complexes with other metals or coordination numbers.

Other Mechanisms for SCO

Beside the above mentioned mechanism for SCO, there are many other mechanisms that are likely to influence the spin state of a complex. External magnetic or electric fields can be used to induce spin transition [2, 63–66], but especially interesting is the coordination driven SCO. A change in the coordination number of a metal ion can very well lead to a change in the most stable spin coupling. For example, Ni(II) is typically diamagnetic in nature when it is coordinated to four ligands in a square planar fashion. However, when an external perturbation can axially coordinate an extra ligand, the 3d(z^2) orbital is strongly destabilized and the triplet state may become competitive depending on the donor strength of the ligands. This mechanism has been shown to be effective to trigger a room temperature fully switchable SCO in a Ni(II) complex by the light-induced cis-trans isomerization of one of the ligands [66, 67].

Spin-crossover in Binuclear Complexes

Spin crossover is not restricted to mononuclear complexes but has also been observed in complexes with more than one transition metal center [68–73] and extended systems [74–76]. Among polynuclear species, binuclear complexes occupy a special place being the simplest systems to combine magnetic coupling with spin crossover properties. The number of systems that have been fully characterized is not very large and they present a tremendous challenge for theoretical studies given the subtle interplay of local and inter-site magnetic interactions, that is, a possible synergy of magnetic coupling and SCO phenomenon.

The first family of binuclear Fe(II) SCO complexes was synthesized using a μ-bipyrimidine (bpym) bridging ligand in the group of Real [68]. The general formula of the complexes is $(\mathrm{Fe(L)(NCX)_2})_2(\mathrm{bpym})$, where L = bpym or bt (bt = 2,2'bithiazoline) and X = S, Se. Figure 1.4 gives a ball and stick representation of the complex. The application of a collection of different experimental techniques revealed that these complexes not only show thermal spin crossover but are also photomagnetically active. The total spin state of the system can be changed by light irradiation.

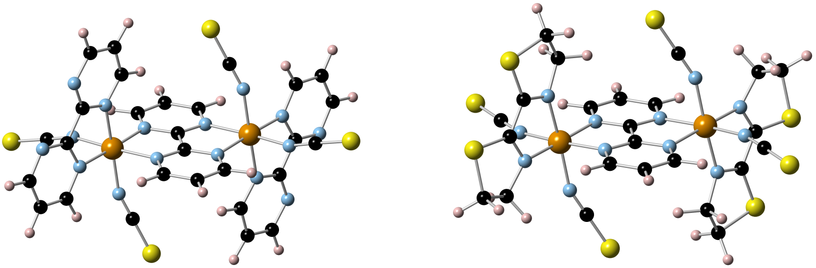

Figure 1.4: Ball and stick representation of the binuclear Fe(II) complexes synthesized by the group of Real [68]: (Fe(bpym)$(NCS)_2)_2$(bpym) (left) and (Fe(bt)$(NCS)_2)_2$(bpym) (right). Color code: orange for Fe, red for O, black for C, blue for N and pink for H.

The most common spin transition in these complexes is a one-step process from a diamagnetic state with LS coupling on both metals ([LS]–[LS]) to a double HS state ([HS]-[HS]), where the latter shows antiferromagnetic coupling of the two spin moments in most cases, although ferromagnetism cannot be excluded beforehand. In some cases, a two-step SCO was observed, which was ascribed to the population of an intermediate state with one HS and one LS center ([LS]-[HS]) [73, 77, 78]. Beside the L=bt; X=S member of the above mentioned family, ^{57}Fe Mössbauer spectroscopy also probes the existence of a two-step SCO in [Fe(phdia)$(NCS)_2]_2$(phdia) (phdia = 4,7-phenanthroline-5,6-diamine) and [Fe$(NCS)_2$(picen)] (picen= bis(2-pyridilmethyl)ethylenediamine) [79, 80]. No [LS]-[HS] state was observed in the Co dinuclear complex $[Co_2L(NCS)_2(SCN)_2]$ [81].

Theoretical Studies on SCO Complexes

The pioneering work of Paulsen and co-workers [82] established that standard density functional theory calculations are not accurate enough to predict the stability of high-spin state with respect to the low-spin state (ΔE_{HL}) in mononuclear SCO complexes. Over the past decade, it has been concluded that even the best current DFT functionals can display large errors for specific types of transition metal energetics. In particular, standard pure functionals (like LDA, BLYP, or PBE) systematically overstabilize low-spin states, while hybrid functionals (like B3LYP, or PBE0) overstabilize high-spin states overstabilize HS states due to the inclusion of Fock exchange in the functional. The B3LYP*, OPBE and TPSSh functionals have emerged as the most adequate options to describe the energetics of the spin states involved in transition metal SCO. The B3LYP* functional reduces the amount of Fock exchange in the standard B3LYP functional to 15% based on the observation of Reiher that ΔE_{HL} varies linearly when plotted against the percentage of Fock exchange in the functional [83, 84]. Good agreement with experiment was observed around 15% for $\mathrm{Fe(phen)_2(NCS)_2}$ in a first study and later confirmed for other compounds. Swart and co-workers studied different combinations of exchange and correlation functionals to design an optimal non-hybrid functional [85, 86]. They concluded that combining PBEc with the optimized exchange functional of Handy (OPTX) correctly describes the relative stability of the different spin states in a large collection of TM complexes and labeled the combination as OPBE. After a careful recompilation of the performance of different functionals, Kepp proposes, in addition to B3LYP*, the TPSSh functional for SCO [87]. Studies devoted to the SCO phenomenon using post Hartree-Fock methodologies were also reported. These strategies are based on a multiconfigurational description of the electronic structure and make it possible to manipulate pure spin eigenfunctions, to treat ground and excited states on an equal footing, and include spin-orbit coupling effects. A standard implementation of multiconfigurational self-consistent field (SCF) calculations is given by the complete active space (CASSCF) introduced by Roos and co-workers [88] in the 1980s. Combining CASSCF with multiconfigurational second-order perturbation theory (CASPT2) [89] results in a very successful computational scheme to treat transition-metal complexes. The CASSCF wave function gives a good description of the electron distribution but lacks important dynamic electron correlation effect. The effects do not strongly affect the electron distribution but may give rise to rather large changes in the relative energies of the different electronic states. The complete active space CASPT2 accounts for these effects in the case of multiconfigurational wave functions of medium to large sized systems.

Zein and co-workers [90] studied four binuclear compounds of the $(Fe(L)(NCX)_2)_2(bpym)$ series with DFT and were able to characterise the structure and relative energetic stability of [HS-HS], [LS-LS] and [LS-HS] states. Especially the last one is very difficult to extract from experimental methods. The magnetic susceptibility data of (bt,S) and (bt,Se) display complete spin transitions with a two-step character. For these compounds, the ground state is [LS-LS], confirming the experimental observation. Their calculations confirmed that the position of the intermediate [LS-HS] state is decisive for the appearance of a two-step spin transition. Its enthalpy must be lower than the halfway point between the enthalpies of [LS-LS] and [HS-HS]. ΔH being the enthalpy difference between the [LS-LS] and [HS-HS] states and W standing for the difference between the [LS-HS] and average enthalpies, $\rho = W/\Delta H$ must be negative to observe a two-step thermal SCO. To exist a two-step spin transition are necessary less negative ρ values that require stronger intermolecular interactions, being demonstrated by the negative ρ values of (bt,S) and (bt,Se) which experimentally show a two-step spin transition. In addition, a two-step transition requires a ground state in a [LS-LS] electronic state.

The number of theoretical studies on binuclear iron(II) systems is rather limited and most of them are based on DFT. The multiconfigurational wave function studies are computally expensive due to the large size of the system and the high number of unpaired electrons, which gives rise to large active spaces. Most studies on spin crossover in binuclear complexes were dedicated the thermal spin crossover.

1.2 Molecule-based Magnets

Molecule-based magnetic materials are of current interest because they provide fundamental insight into magnetic phenomena and are potentially applicable in magnetic devices. The history of molecular magnetism began in 1951 with the study of a dinuclear complex of copper(II) acetate [91], however it was not until the 1990s when it received a strong impetus with the discovery of the first molecule-based magnetic material, the $Mn_{12}O_{12}$, which exhibits spontaneous magnetization [24, 92]. The progress in the area has led to the discovery of single-molecule magnets, the single-chain magnets or the more recent single-ion magnets.

Single Molecular Magnets

Single molecule magnets (SMMs), or occasionally molecular nano-magnets, are polynuclear metal complexes whose structures consist of magnetic cluster of exchange coupled transtion-metal ions protected by a shell of ligands. The name "SMMs" reflects the ability of a single molecule to function as a magnet. Since the first synthesis of an Mn_{12} cluster in 1980 by Lis [93] and the posteriori study by Gatteschi *et al.* [24, 92], many research groups have been involved in the synthesis of new systems that may lead to smallest possible devices. A particularly attractive feature of SMMs is that they are amenable to engineering by chemical and self-assembly techniques to produce and control desirable properties in molecules and their mutual interactions.

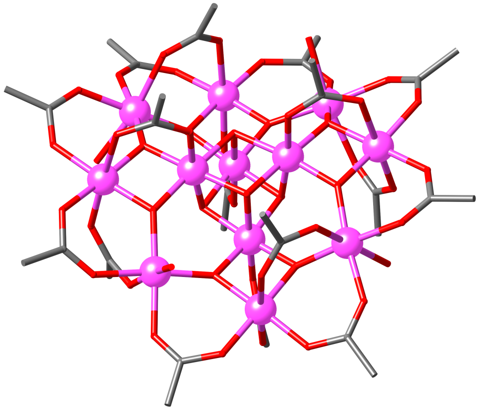

Figure 1.5: Ball and stick representation of the Mn_{12} cluster. Color code: Pink for Mn, red for O and dark grey for C.

SMMs are nano clusters in which each molecular unit can contain as few as two and up to several dozens of paramagnetic ions. A single molecular magnet has an appreciable potential barrier for reversal of the direction of magnetization. There are two basic requirements to function as SMM, (i) the ground state of the molecule should have a large spin, and (ii) a large and negative axial anisotropy D must be present. These two boundary conditions may cause slow magnetic relaxation below a characteristic blocking temperature, T_B. All SMMs introduce transition metal ions such as Fe, Mn, Ni and Co as the source of their magnetic properties. The magnetic core of each complex comprises multiple ions with unpaired electrons, which are strongly coupled to each other through intramolecular exchange interactions. Intramolecular exchange is the interaction between the ions within a molecule, and the bulky organic ligands that surround the magnetic core serve to isolate each molecule from the sorrounding neighbours. Thus, intramolecular exchange interactions are rather weak and there is no long-range ordering. The total spin angular momentum of a given SMM ranges from a few to many times that of an electron, so, the corresponding magnetization of the individual magnets is minuscule. At the same time, the SMMs are relatively far apart so that the magnetic exchange between them is small, and they interact only very weakly with each other.

The magnetic behaviour of SMMs is governed by the anisotropic zero-field splitting parameters, the axial (D) and the rhombic (E) anisotropy, both reflecting which type of symmetry there is around the magnetic centre. The sign of D is critical, since it determines the type of magnetic anisotropy associated with the S multiplet. A positive sign (easy-plane anisotropy) implies that the $M_S = 0$ state will have the lowest energy, therefore the magnetic phenomena associated with SMMs cannot be observed. By contrast, a negative value (easy-axis anisotropy) means that the $M_S = \pm S$ states will be the most stable, a situation that is fundamental for the magnetization in SMMs. The processes of magnetization and relaxation are illustrated in Figure 1.6, 1.6a reflects the situation when zero-field exists and all $M_S \neq 0$ levels form degenerate pairs. The barrier between the level with maximum M_S value and the equal M_S=0 is related with the axial anisotropy and the total spin of the molecule by $E_B = |D|S^2$. Figure 1.6b describes the situation after the application of an external field parallel to the magnetization axis, inducing a stabilization of the -M_S levels and a destabilization of the $+M_S$, if the magnetization value reaches its saturation value, then only the M_S = -S remains populated. Figure 1.6c describes a situation after removing the external field and the relaxation process to the thermal equilibrium of Figure 1.6a through tunneling processes.

In resume, the larger the E_B barrier, the longer the relaxation time and the better the funcionality of the system as memory storage. For a long time, the main goal of the researchers was to find molecules with enormous spin values, like $S = 83/2$ of the Mn_{19} [25], in order to increase the energy barrier. But it was Ruiz and coworkers [94] who compared two Mn_6O_2 compunds and questioned the possible coexistence of large magnetic anisotropy and high-spin values because the compound with the lowest spin presented a higher anisotropy parameter while the anisotropy becomes much smaller in the complex for the highest total spin. The impossibility to raise the blocking temperature beyond the one observed for Mn_{12} made researchers explore new routes to increase the anisotropy barriers, being the one-dimensional systems a interesting option.

Single-chain Magnets

Single-chain magnets (SCMs) are a class of molecular magnetic materials exhibiting slow magnetic relaxation, which arises from large uniaxial type magnetic anisotropy, strong intrachain and very weak or negligible interchain magnetic interactions, and which may also exhibit magnetic hysteresis of molecular origin. The original

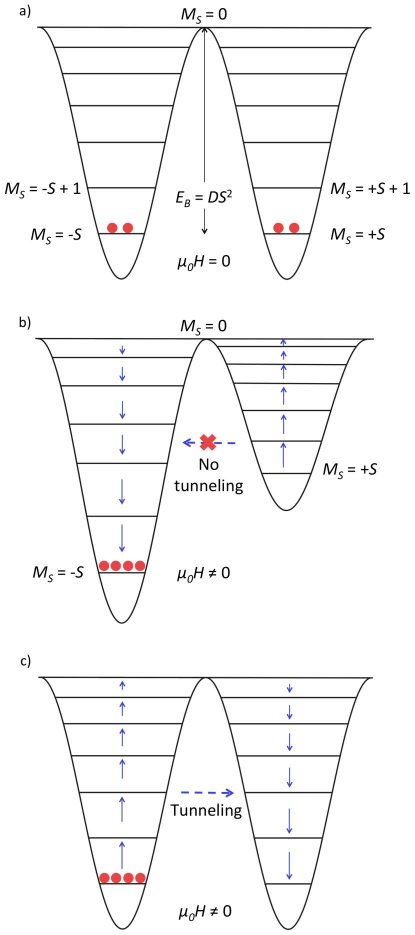

Figure 1.6: Schematic representation of the different situations that can occur during magnetization and magnetic relaxation processes of a single molecule magnet.

motivation for constructing SCMs is to increase the blocking temperature of the SMM so as to fulfill the condition for their future application as molecular memory devices or recording media.

The first prediction for SCM was made by Glauber in 1963 [95], but it was not after 38 years, in 2001, when Gatteschi and co-workers reported the first example of SCM [7] (Figure 1.7). The expression of single-chain was suggested later by Clerac *et al.* in 2002 [96]. The synthetic approaches to build SCM include two important facts: (i) to utilize appropiate bridging ligands as effective magnetic couplers to link, uniaxial, anisotropic spin carriers, such as Co^{2+}, Ni^{2+}, Mn^{3+}, Fe^{2+} and lanthanide ions, into 1D chains, and (ii) to use suitable diamagnetic separators to make these chains magnetically well isolated. Oxygen, cyano, oxalato, and organic radicals have been employed as bridging ligands because they can transport magnetic coupling efficiently. On the other hand, bulky co-ligands, long spacers or counter ions, have been used to reduce the interchain interactions, and some co-ligands themselves also serve as intrachain bridges. The various combinations of intrachain bridges, metal ions, and separators, have led to many SCMs with different spin structures.

SCMs can be seen as large number of magnetic centres correlated within the chain, resulting in high-spin ground state. The structural anisotropy of the chain associated with Ising type magnetic anisotropy of the spins, and, therefore, the analysis of the magnetization and relaxation processes relies on the model elaborated by Glauber [95].

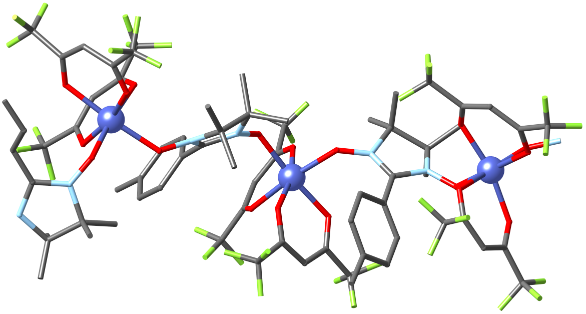

Figure 1.7: Ball and stick representation of the structure of CoPhOMe. Color code: Dark blue for Co, red for O, light blue for N, yellow for F and dark grey for C.

The magnetic behaviour is related with the main concept of the model which is the probability (Figure 1.8) for a spin to flip within the chain, taking into account only nearest-neighbours interactions, with the Hamiltonian $\hat{H} = -J \cdot \sum\limits_{k=1}^{N-1} \hat{S}_k \hat{S}_{k+1}$, α as the probability of reversal of an isolated spin and γ as a factor depending on the energy J of the nearest neighbours interactions.

The dynamics of the Ising system represented in the Figure 1.9 consist on: (a) the preparation of the sample until the saturated state is reached and (b) the relaxation starts when one spin thermally flips in the chain. Let us stress that the cost of a spin flip is only half at the extremes of the chain. After the first reversal, the spin flip on a neighboring center has zero energy cost. Comparing with the SMMs, the SCMs are able to show larger barriers because depend on the exchange coupling, with an anisotropy barrier of $4JS^2$.

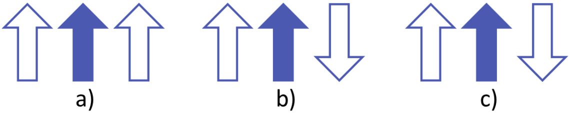

Figure 1.8: The three types of transitions that can occur depending on the orientation of the neigbouring spins. The probabilites depending on the strength of the nearest-neighbour: (a) $\frac{1}{2}\alpha(1\text{-}\gamma)$, (b) $\frac{1}{2}\alpha$ and (c) $\frac{1}{2}\alpha(1+\gamma)$.

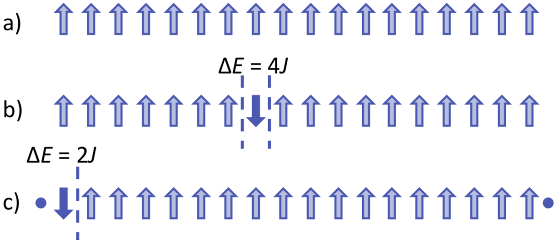

Figure 1.9: Schematic representation of the mechanism of single-spin-flip in 1D Ising systems.

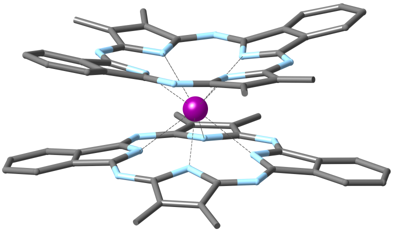

Figure 1.10: Ball and stick representation of the structure of $[\mathrm{Pc_2Tb}]^-$. Color code: Purple for Tb, light blue for N and dark grey for C.

Single-ion Magnets

The appearance of single-ion magnets implies the return to molecular complexes. The first prototypes, proposed by Ishikawa in 2003 [10], included atoms of the group of lanthanides (Figure 1.10), a favourable situation because they involve f-orbitals with large angular momentum and a large number of electrons, and also, a large spin-orbit coupling. These properties in combination with the anisotropy of the ligand field can produce large negative D values and high blocking temperatures.

More recently, research has been focused on the incorporation of 3d-TM atoms in single-ion magnets. In 2010, Chang and co-workers [97] reported a Fe system (Figure 1.11) exhibiting slow magnetic relaxation. Even though it seems counterproductive because their properties are poorly suited in comparison with the lanthanides to build effective systems, the d-blocks metal ions have the ability to create strongly coupled systems which is quasi forbidden by the

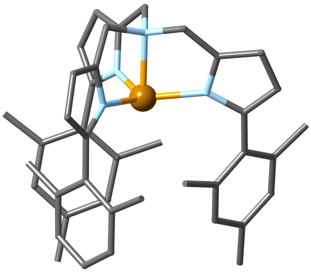

Figure 1.11: Ball and stick representation of the structure of $[(\mathrm{tpa}^{Mes})\mathrm{Fe}]^-$. Color code: Orange for Fe, light blue for N and dark grey for C.

f-orbitals. Rigid polydentate ligands force a highly symmetric environment that induces non-zero orbital moments, and hence, large spin-orbit coupling effect and magnetic anisotropy comparable.

Theoretical Studies of the Magnetic Properties of Molecule-based Magnets

Theoretical studies can provide understanding and analysis of the electronic structure, complement the experimental findings and offer a complete picture of the phenomenon. To perform a detailed analysis of the magnetic properties, the system should be represented by a spin Hamiltonian that can involve the parameters J_{ab} (isotropic coupling), D (axial anisotropy) and E (rhombic anisotropy), among others. Different methods are now available for the computational interpretation and analysis of the magnetic data, most of them based on the density functional theory

(DFT) [94, 98–104], with a special mention to the works of Pederson and Neese with different approaches to the zero-field splitting (ZFS) and the variants proposed to treat the spin-orbit coupling (SOC). Wave function based methodologies [105–119] have also been widely applied to TM-3d complexes and Ln-based systems. The scheme proposed by Maurice to extract the ZFS and the magnetic anisotropy using the effective Hamiltonian theory and the work of Chibotaru that calculates the anistropic magnetic properties directly from the matrix elements of $\hat{L}$ and $\hat{S}$ to a posteriori definition of the pseudospin Hamiltonians are two relevant works in multiconfigurational background.

Since the pioneering work of Noodleman in 1981 on the description of the coupling in transition metal dimers [120], DFT has been widely applied to calculate isotropic couplings between magnetic centers. DFT permits the treatment of molecules with a large number of atoms without modeling any part of the system. However, it relies on the broken symmetry approach (see Chapter 2) due to the impossibility to properly represent spin eigenfunctions with a single determinant. Wave function based methodologies have emerged as the most powerful and accurate way to analyze the magnetic anisotropy properties. The major handicap of these methods is the high computational cost as compared to DFT.

1.3 Objectives and Road Map

The planning, the development and, finally, the concluding remarks are real challenges when one opt to become part of a research group as PhD student. The results of the work during the years spend by a researcher doing its thesis are not only reflected in this book, but also in the knowledge and capacities acquired, and consequently, in its progress as a human being.

Over the last decades the world of technology and the development of new devices have become vital for our society. The aim of this thesis is to contribute to this research field with the study of magnetic materials by using computational tools, and in some cases combining it with experimental results. The objectives of the thesis can be summarized as follows:

1. Developing a reliable computational strategy to describe the electronic structure of spin crossover complexes that does not suffer from the large computational burden inherent to the CASSCF/CASPT2 approach. This lighter computational approach can be used to describe spin crossover in polynuclear complexes when the standard multiconfigurational methods are simply too demanding. We validate the B3LYP* functional for mononuclear complexes with Fe in different oxidation states.

2. Establishing the effect of the solvent on the transition energies in spin crossover complexes and relate the possible existence to changes in the dipole moment between initial and final states.

3. Extending the description of the LIESST mechanism from Fe(II) done in previous studies to Fe(III) complexes, for which much less experimental and theoretical data exist.

4. Careful analysis of the electronic structure of Fe(IV) in biomimetic complexes to contribute to the detailed understanding of the experimentally observed relation between reactivity and the Fe-S distance. The spin density is quantified and a valence bond analysis of the wave function is used to obtain new insights, which are complementary to experiment and DFT calculations.

5. Putting the variational wave function based methods to a stringent test describing the magnetic properties of a series of MnCr binuclear complexes, which show weak magnetic coupling. The experimental data is contradictory about the nature of the coupling; ferromagnetic or antiferromagnetic. Moreover, the role of the single ion anisotropy has never been studied in detail and this gap has to be filled to obtain a complete picture of the magnetic properties of these complexes.

These studies unite all the necessary ingredients to pave the way for the description of the light-induced spin crossover in binuclear complexes. Thermal spin crossover in Fe(II) binuclear complexes has been subject of theoretical studies but the light-induced variant is still to be explored, and other oxidation states or metals has not been considered so far. The present thesis lays all fundaments for such studies. Due to time limitations, we have unfortunately not been able to enter this highly interesting area of research in the time span of this thesis.

After the Introduction (Chapter 1) which introduces the reader to the world of magnetic molecular materials and the Methodology

(Chapter 2) where the theoretical framework is explained in detail, the following lines resume the main points of the forthcoming chapters: the goals of each chapter, the computational tools used, the results obtained and the conclusions drawn.

#***Chapter 3:*** The description of the results obtained in this thesis starts with a relatively simple, well-studied class of compounds, namely the Fe(II) spin-crossover complexes. We investigate the solvent effects on the electronic states of Fe(II) and Ru(II) complexes to verify the important solvent effects suggested by Tribollet *et al.* to explain the differences in the transient absorption spectroscopy study of the $[Fe(phen)_3]^{2+}$. The first step was to study the electronic states of the different spin states at DFT level in its time-dependent variant. Moreover, CASSCF/CASPT2 calculations were performed in order to make a comparison between the two methods and the experimental results. In our first investigation we found that TD-DFT/PBE0 does not compare very favorably with the experimental data, but the improvement of the computer resources let us extend the number of roots analyzed to finally find a better agreement with the experimental spectrum. The results obtained with the multi-configurational method and those obtained with TD-DFT/B3LYP* were in much better agreement with the experiment. However, both methodologies agreed on a nearly negligible effect of the solvent on the transitions of $[Fe(phen)_3]^{2+}$ due to the high symmetry of the complex. The solvent effects are significantly bounded with the change of the dipole moment during the transition. Supporting calculations on asymetric complexes, trans(Cl)-$Fe(bpy)Cl_2(CO)_2$ and trans(Cl)-$Ru(bpy)Cl_2(CO)_2$ were done to confirm our suppositions. Finally, an analysis of the wave function was performed using orthogonal Valence Bond theory obtaining two conclusions: (i) the wave function of the ground state does not suffer changes when the solvent effects are included and (ii) the weight of the ligand-to-metal charge transfer (LMCT) determinants is an indication of a possible thermal SCO. When the LS wave function has a contribution of approximately 45% of the LMCT, the complex is susceptible to thermal SCO.

#***Chapter 4:*** The most widely studied SCO complexes are based on the prototypical Fe(II)N_6 core, but other ions and coordination spheres are becoming more and more important in the field. Therefore, we changed topic and moved on to the less intensively studied Fe(III) complexes. We followed the strategy proposed by Papai *et al.* to study the electronic structure and the thermodynamic properties of Fe(II) spin-crossover complexes and validated it for two Fe(III) complexes, $[Fe(qsal)_2]^+$ and $[Fe(pap)_2]^+$. In this case, we used the B3LYP* functional for all DFT and TD-DFT calculations. We proved that the combination was suitable to obtain accurate geometries, vibrational frequencies and relative energies of the states involved in the thermal and light-induced spin-crossover of the two Fe(III) complexes. Additional TD-DFT/B3LYP* studies were done for two other Fe(III) complexes with a well-known experimental spectrum to establish the capacity of the functional to reproduce absorption spectra. Moreover, we performed a study of the LIESST mechanism combining TD-DFT/B3LYP* and CASSCF. Firstly, a two-dimensional scan of the energy surfaces of LS and HS states were produced to define an approximate minimal energy path (MEP). Then, the excited states were studied to clarify which states are involved in the process, and finally, the intersystem crossing rates were calculated with the time dependent formulation of Fermi's golden rule as done before in $[\mathrm{Fe(bpy)_3}]^{2+}$. The scenario obtained let us propose two competing pathways in the photocycle, namely the deactivation from ^{2}LMCT→IS→HS competes with the ^{2}LMCT→IS→LS pathway, in line with the low efficiency encountered in experiments.

#***Chapter 5:*** After studying over Fe(II) and Fe(III) SCO complexes, we extended the research increasing the oxidation state of iron to IV. In this case, we selected a biomimetic model of the widely studied P450-I and CPO-I, $(\mathrm{SCH_3})\mathrm{Fe^{IV}(O)(Porph)}$, not only to study the influence of the oxidation state on the energy ordering of the different spin-states, but also to contribute to the understanding of the different reactivity of both complexes. First, we used the same strategy as applied for the Fe(III) complexes with DFT/B3LYP* to obtain geometries, vibrational frequencies and relative energies of the LS, IS, and HS. The LS and IS states were found to be quasi degenerate, and the HS much higher in energy, indicating that the latter does not influence the properties of the complexes. Additional CASSCF/CASPT2 calculations were done to construct an energy surface of the LS and IS as function of the Fe-S and Fe=O distances. A flat valley was observed along the Fe-S distance of the LS PES, which is an indication of the difficulty to precisely determine the optimal bonding distance of Fe and S with computational tools. Furthermore, we found a very small ΔE(LS-IS) which confirms the quasi degeneracy obtained with the

B3LYP* calculations. The second step was to perform a detailed analysis of the electronic density. The results confirm the presence of 3 unpaired electrons, two of them situated in the Fe=O moiety, and the other one mostly resides on the sulphur ligand, with residual density on the porphiryn. Moreover, we found evidences that the metal center is not an exact Fe^{4+}, being better described as Fe^{3+}–$O^{\bullet}$. To complete the study, we have focused on the magnetic properties. Using diverse tecniques, like DDCI or Broken-symmetry we have analyzed the isotropic magnetic coupling and extracted the anisotropy parameters over the flat LS valley. The magnetic coupling (J) is strongly affected by the Fe-S distance, but the axial anisotropy (D) remains constant.

#***Chapter 6:*** Being the mononuclear iron complexes studied in the previous chapters, we switched to binuclear metal transition complexes as a first step towards the description of SCO in binuclear complexes. Three oxalate-based MnCr complexes were studied combining experimental and theory. The experimental part was carried out by the experimental group of Cyrille Train of the University of Strasbourg. Firstly, they synthesized and characterized the compounds, and after that, they studied the magnetic properties (see *Section: Experimental Part* of Chapter 6). They found ferromagnetic coupling for the three complexes and the structural differences hardly change the magnetic properties. Moreover, they confirm that increasing the number of ligands cordinated to the divalent Mn center from six to seven does not affect the magnetic coupling which remains ferromagnetic, in contrast to the earlier experimental studies done by Coronado *et al.* reporting a change in the magnetic behaviour from a ferromagnetic coupling for the hexacoordinated environment to a antiferromagnetic coupling for when Mn is heptacoordinated. After these findings, we complemented the studies using theoretical strategies. The theoretical part of the thesis was divided in three sections: a first part where we check the robustness of the Heisenberg Hamiltonian with the CASSCF, CASPT2 and variational methodologies. The CASSCF and variational methodologies show small deviations from the Heisenberg Hamiltonan, contrary to the large deviations of the CASPT2. The second one where we analyze the different variational methodologies with different active spaces to select the optimal combination MOs-distribution/method. We use the strategy that combines localized orbitals (DOLO program) and SEL+DDCI-2 which let us select the desired orbitals and eliminate the di- and tri-ionic configurations from the CASSCF wave function. The last part includes a complete study of the magnetic properties. The magnetic coupling parameters show a ferromagnetic behaviour and the strength of the couplings, although systematically underestimated, are in reasonable agreement with the experimental values. The non-negligible axial anisotropy may be at the origin of the deviation between theory and experiment. The strong exchange limit is possibly not valid due to the mixture between the sublevels of the S=3 and S=4 electronic states.

1.4 List of Publications

Publication 1: *"On the role of solvent effects on the electronic transitions in Fe(II) and Ru(II) complexes"* S. Saureu and C. de Graaf, *Chem. Phys.*, 2014, **428**, 59–66.

Publication 2: *"TD-DFT study of the light-induced spin crossover of Fe(III) complexes"* S. Saureu and C. de Graaf, *Phys. Chem. Chem. Phys.*, 2016, **18**, 1233–1244.

Publication 3: *"Delving into the Magnetic, Electronic and Geometrical parameters of P450-I and CPO-I"* S. Saureu, C. de Graaf and V. Robert. *In preparation.*

Publication 4: *"Amidinium-templated 2D [MnCr] Bimetallic Oxalate-Based Networks: The Influence on Structure and Magnetism Explored by Combining Experience and Theory"* C. Maxim, S. Saureu, C. de Graaf, S. Ferlay, M. W. Hosseini, V. Robert and C. Train. *Submitted.*

CHAPTER 2

Methodology

2.1 Density-based Methods

Density Functional Theory (DFT)

Calculations based on density functional theory (DFT) are among the most widely used approaches to study the electronic structure of many-body systems. DFT emerged as a powerful alternative to the wave function-based methods (see *Section 2* of the present chapter) due to the lower computational cost in the treatment of bigger size systems. Accurate descriptions of the electronic structure can be obtained at a cost similar to the mean-field Hartree-Fock method.

The origin of DFT lies in the model developed by Thomas and Fermi [121, 122]. The energy is written as a sum of three density-dependent terms

$$E_{TF}[\rho(r)] = T[\rho(r)] + V_{n,e}[\rho(r)] + V_{e,e}[\rho(r)] \tag{2.1}$$

where the potential energy terms $V_{n,e}$ and $V_{e,e}$ are represented with the classical expressions and the kinetic energy is derived from the homogeneous electron gas.

$$V_{n,e}[\rho(r)] = \sum_{\alpha} \int \frac{Z_{\alpha}}{r - r_{\alpha}} \rho(r) dr \tag{2.2}$$

$$V_{e,e}[\rho(r)] = \frac{1}{2}\int\int \frac{\rho(r_1)\rho(r_2)}{r_1 - r_2} dr_1 dr_2 \tag{2.3}$$

$$T[\rho(r)] = \frac{3}{10}(3\pi^2)^{\frac{2}{3}} \int \rho^{\frac{5}{3}}(r)d(r) \tag{2.4}$$

The big advantage of expressing the energy as a density functional is that the number of variables is reduced to three instead of the 3N when an N-electron wave function is used. Unfortunately, the Thomas-Fermi model is incapable of describing chemical bonding. The extensions of the model by Bloch, Dirac and Slater with expressions for the exchange interactions improved the model [123–126].

$$E_x[\rho(r)] = \frac{9\alpha}{8}\left(\frac{3}{\pi}\right)^{\frac{1}{3}} \int \rho^{\frac{4}{3}}(r)dr \tag{2.5}$$

with α=2/3 (Dirac and Bloch) or α=1 (Slater). However, the resulting X_α-method is still not precise enough for practical usage in modern quantum chemistry.

Modern DFT starts in 1964 when Hohenberg and Kohn [127] (HK) formulated two theorems that established that the energy is a functional of the electron density and that the electron density of the real system minimizes this functional.

#*Theorem 1:* The ground state expectation value of any physical observable of a many-electron system is a unique functional of the electron density ρ.

In other words, the Hamiltonian, the wave function of the ground state and the total energy are determined by the density ρ through an external potential:

$$\rho(r) \rightarrow V_{ext}(r) \rightarrow \hat{H} \rightarrow \Psi \tag{2.6}$$

The energy can be described as a functional of the density if this electron density is N-representable ($\rho \geq 0$ and ρ(r)dr=N) and V-representable (ρ(r) can be derived from an external potential $\hat{V}_{ext}$).

$$E[\rho(r)] = F_{HK}[\rho(r)] + \int \rho(r) V_{ext}(r) dr \tag{2.7}$$

being $F_{HK}[\rho]$, known as universal functional, the sum of the kinetic energy ($T[\rho]$) and the electron repulsion ($V_{ee}[\rho]$).

#*Theorem 2:* The total energy functional has a minimum, the ground state energy E_0, corresponding to the ground state density ρ_0.

It means that the functional that represents the ground state energy only delivers the lowest energy if the input density belongs to the ground state, ρ_0(r).

Combining both theorems and applying the N-representation restriction through the use of Lagrange multipliers (μ), we can obtain the fundamental equation of density functional.

$$\mu = \frac{\partial E_{\upsilon}[\rho(r)]}{\partial \rho(r)} = \upsilon_n(r) + \frac{\partial F_{HK}[\rho]}{\partial \rho(r)} \tag{2.8}$$

The HK theorems do not provide the explicit $F[\rho]$, and more theoretical development was needed to handle many-body systems. In 1965, Kohn and Sham (KS) presented an important breakthrough by introducing an auxiliary system of non-interacting electrons [128]. The exact wave function for a non-interacting system can be expressed as a single Slater determinant. Moreover, through the Born Oppenheimer approximatin, it assumes that the external potential reproduces the effects of the nuclear atraction and the interelectronic repulsion.

$$\hat{h}_{KS}(r) = -\frac{1}{2}\nabla^2 + \upsilon_{KS}(r) \tag{2.9}$$

The ground state electron density can be written as a set of one electron orbitals (the KS orbitals),

$$\rho(r) = \sum_{i}^{N} \left| \varphi_i^{KS}(r) \right|^2 \tag{2.10}$$

the exact exact expression for the kinetic energy for non-interacting systems,

$$T^{KS}[\rho] = \sum_{i}^{N} \left\langle \varphi_i \middle| -\frac{1}{2}\nabla^2 \middle| \varphi_i \right\rangle \tag{2.11}$$

and the energy of the system can be expressed as a functional of the density:

$$E_{KS}[\rho] = T_{KS}[\rho] + V_{n,e}[\rho] + V_{e,e}[\rho] + E_{XC}[\rho] \tag{2.12}$$

$V_{n,e}$ and $V_{e,e}$ are given in Eqs. 2.2 and 2.3(Thomas-Fermi) and $E_{XC}[\rho]$ is the exchange correlation energy collecting all unknown terms. More specifically, it contains the difference between the exact kinetic energy of the N-electron system and the one of auxiliary system plus all exchange and correlation effects.

The solution of the Kohn-Sham equation is performed in a self-consistent iterative process. An approximate form of the functional that describes the dependence of $E_{XC}[\rho]$ on the electron density is used to calculate $\upsilon^{KS}[\rho]$.

$$\upsilon^{KS}(r) = V_{n,e}(r) + \int \frac{\rho(r_2)}{|r_1 - r_2|} dr_2 + \frac{\partial E_{XC}[\rho]}{\partial \rho(r)} \tag{2.13}$$

The procedure is used to calculate an initial set of Kohn-Sham orbitals, and this set is used to calculate an improved density. This iterative method is repeated until $\rho^{KS} = \sum_i |\varphi_i(r)|^2 = \rho_0$ is satisfied. ρ_0 is related to the convergence criteria demanded, because the exact expression is not affordable and some approximations are used. To solve the problem in the best possible way, the choice of the approximate exchange correlation functional is, in general, the most important step to perform a calculation.

Exchange-correlation Functionals

As explained above, the exchange-correlation functional includes the correction to the kinetic energy and the exchange and correlation energy. An exact expression is not available but over the last decades, the development of functionals has been intense, being LDA, GGA, meta-GGA, hybrid and range-separated hybrid functionals the most frequently used.

#*Local Density Approximation (LDA)*[121, 122, 125]: This approach assumes that $E_{XC}(\mathrm{r})$ can be calculated from the value of $\rho(\mathrm{r})$, that is only local information is used. The exchange-correlation functional is the sum of two analytical expressions representing the exchange (ε_X) and correlation (ε_C) functionals. The expression of the exchange energy of a homogeneous electron gas is used for ε_X (see Eq. 2.5), while ε_C is a rather lengthy expression obtained by fitting accurate quantum Monte Carlo data [129].

$$\begin{gathered} E_{XC}^{LDA}[\rho] = \int \rho(r)\varepsilon_{XC}(\rho)\partial r \\ \varepsilon_{XC}(\rho) = \varepsilon_X(\rho) + \varepsilon_C(\rho) \end{gathered} \tag{2.14}$$

In open-shell systems, the densities of α and β electrons should be treated separately by using the *local spin density approximation* [130] and the exchange contribution is partioned.

$$\varepsilon_{XC}^{LSDA}(\rho^{\alpha}) = \varepsilon_X(\rho^{\alpha}) + \varepsilon_C(\rho^{\alpha}, \rho^{\beta}) \tag{2.15}$$

#*Generalized gradient approximation (GGA)*[131]: in this approach, the dependence of ϵ on the density is complemented with a gradient dependent term $\nabla\rho$.

$$E_{XC}^{GGA}[\rho] = \int f(\rho, \nabla\rho)dr \tag{2.16}$$

Further improvement was achieved in the *meta-GGA* by introducing terms in the functional that depend on the kinetic energy density $\tau(r) = \frac{1}{2}\sum_i |\nabla\psi(i)|^2$ and the second derivate of the density $\nabla^2\rho$.

$$E_{XC}^{m-GGA}[\rho] = \int f(\rho, \nabla\rho, \nabla^2\rho, \tau)dr \tag{2.17}$$

#*Hybrid functionals*: this approach mixes the exact Hartree-Fock exchange and the exchange correlation by means of the adiabatic connection method that reads $E_{XC} = E_X^{HF} + \gamma(E_{XC}^{DFT} - E_X^{HF})$. In this thesis the B3LYP* functional [83, 132], which reduces to 15% the HF exchange of the classical B3LYP[133–135], has been the most often used hybrid functional. In addition, the PBE0 has also been applied [136]. This functional uses a mixture of 25% of exact HF exchange with 75% of PBE exchange, and the correlation described by PBE.

$$\begin{aligned} E_{XC}^{B3LYP}[\rho] &= E_x^{LSDA} + 0.20(E_x^{Exact} - E_x^{LSDA}) + 0.72\Delta E_x^{B88} \\ &+E_c^{VWN} + 0.81(E_c^{LYP} - E_c^{VWN}) \\ E_{XC}^{B3LYP}[\rho] &= E_x^{LSDA} + 0.15(E_x^{Exact} - E_x^{LSDA}) + 0.72\Delta E_x^{B88} \\ &+E_c^{VWN} + 0.81(E_c^{LYP} - E_c^{VWN}) \end{aligned} \tag{2.18}$$

$$E_{XC}^{PBE0}[\rho] = 0.25E_x^{HF} + 0.75F_x^{PBE} + E_c^{PBE} \tag{2.19}$$

Time-dependent Density Functional Theory (TD-DFT)

The time-dependent DFT extends the basic ideas of the ground state density funtional theory to the treatment of excited states. The introduction of TD-DFT was done by Runge and Gross [137] with the publication of a theorem that permitted a generalization of the first HK theorem to the time-dependent framework. The first step is to demonstrate the existence of an unique time-dependent one-body density ρ(r,t) and the time-dependent potentials υ(r,t), RG demonstrated that the charge density depending on time determines the wave function. Then, a corresponding KS construction can be built:

$$i\frac{\partial}{\partial t}\varphi_i(r,t) = (-\frac{1}{2}\nabla^2 + \upsilon_{KS}(r,t))\varphi_i(r,t) \tag{2.20}$$

$$\rho(r,t) = \sum_i^N \left|\varphi_i(r,t)\right|^2 \tag{2.21}$$

$$\upsilon^{KS}(r,t) = \upsilon_{ext}(r,t) + \int \frac{\rho(r_2,t)}{|r_1 - r_2|}dr_2 + \upsilon_{XC}(r,t) \tag{2.22}$$

The orbitals φ_i(r,t) are the time-dependent Kohn-Sham orbitals which generate the density ρ(r,t). The υ_{KS}(r,t) is the time-dependent potential that let us obtain the real density when applied. The υ_{XC} is the correlation and exchange potential that depends on the density.

In the linear-response expression of the TD-DFT, a small perturbation is assumed and the exact response of the density $\partial\rho$(r,t) to the time-dependent perturbing potential can be expressed:

$$\partial\rho(r,t) = \int \chi_{KS}(rt, r't')d\upsilon_{KS}(r't')dr' \tag{2.23}$$

where the χ_{KS} is the response of the KS system. The equation can be expressed, in terms of time-dependent KS orbitals $\varphi_i^0(r)$ and its Fermi occupation f_i, after a Fourier transformation.

$$\chi_{KS}(r, r', \omega) = 2 \sum_{j,k} (f_k - f_j) \frac{\varphi_j^0(r)\varphi_k^{0*}(r)\varphi_j^{0*}(r')\varphi_k^0(r')}{\omega - (\epsilon_j - \epsilon_k) + i\eta} \tag{2.24}$$

$$\begin{gathered} \chi(r, r', \omega) = \chi_{KS}(r, r', \omega) + \int dr'' \int dr''' \chi(r, r', \omega) \\ \left[\frac{1}{|r'' - r'''|} + f_{XC}(r'', r''', \omega) \right] \chi_{KS}(r''', r', \omega) \end{gathered} \tag{2.25}$$

The expression χ_{KS} can be derived, obtaining the fundamental equation of the linear-response TD-DFT, through which, we can obtain the true excitation energies and oscillator strengths. The most widely used implementation of linear-response TD-DFT is based on the reformulation of this equation by Casida [138] in terms of a set of coupled eigenvalue equations.

$$\begin{pmatrix} A & B \\ B & A \end{pmatrix} \begin{pmatrix} X \\ Y \end{pmatrix} = \Omega \begin{pmatrix} -1 & 0 \\ 0 & 1 \end{pmatrix} \begin{pmatrix} X \\ Y \end{pmatrix} \tag{2.26}$$

where the matrices A and B contain the integrals of the exchange correlation kernel f_{XC} and the Kohn-Sham orbitals, Ω corresponds to the excitation frequencies, and X and Y are the corresponding eigenvectors of the excited states.

In open-shell systems, it has been found thath the neglect of B, the so-called Tamm-Dancoff approximation [139], leads not only to a significant speed-up, but also resolves the issue of the appearance of spurious triplet states below the ground state when the full equation is used.

Broken-symmetry Approach

In DFT-based methods, the most widely applied approximation to evaluate the magnetic coupling within a single determinant description of the spin-states is the Broken-symmetry (BS) approach. The J value can be extracted from the difference between the determinant with maximum M_S value and the so-called Broken-symmetry determinant with the lowest possible M_S value. In a two-electron example, $\Phi_{HS} = |\phi_1\phi_2|$ and $\Phi_{BS} = |\phi_1\overline{\phi}_2|$ where the barred orbital has an electron with beta spin since the single determinant nature of KS-DFT does not allow the use of pure spin eigenfunctions, the usual way to treat the systems is by using the unrestricted formalism where the spin orbitals have different spatial parts.

In order to correctly describe the low-spin state (the single determinant description of HS state is not a problem) it is necessary to force a BS solution [140, 141] in which the open-shell magnetic orbitals are localized in different centers and occupied by electrons with opposite spin moments. One of the most rigorous and famous relations between J and the energies of the different determinants is the Yamaguchi spin projection procedure [142]. This relation can be obtained by the projection of BS solutions onto the pure spin state of lowest multiplicity to eliminate the spin contamination.

$$J = \frac{2(E_{BS} - E_{HS})}{\left\langle S^2 \right\rangle_{HS} - \left\langle S^2 \right\rangle_{BS}} \tag{2.27}$$

2.2 Wave Function-based Methods

Multiconfigurational CASSCF/RASSCF

The single-determinant nature of DFT methods can give erroneous results when describing the electronic structure of excited states, of systems with (near-)degeneracies, of bond breaking processes, etc. In such situations, multiconfigurational (MC) approaches are employed to properly obtain the description of the electronic states. Generally speaking, the wavefunction is written as linear combination of single Slater determinants.

$$\Psi = \sum_i c_i \Phi_i = c_0 \Phi_0 + \sum_{a,r} c_a^r \Phi_a^r + ... \tag{2.28}$$

where Φ_0 is the Hartree-Fock determinant and Φ_a^r is a single excited Slater determinant replacing an electron in orbital a by an electron in orbital r. A popular MC method is the multiconfigurational self-consistent field (MCSCF), in which both the coefficients of the configurations and the orbitals of the wavefunction are optimized simultaneously through an SCF procedure. One of the most widely used defines the MC space as complete active space, the CAS [88]. The active space is contructed by dividing the orbitals in three subsets: (i) the inactive orbitals which are doubly occupied in all the determinants of the wavefunction expansion, (ii) the virtual orbitals which remain unoccupied, and (iii) the active orbitals and the corresponding number of electrons that generate all possible configurations compatible with the spin multiplicity.

The common problem of the CASSCF is the limit of orbitals-electrons that can be used. Depending on the spin, spatial symmetry and size of the system under study, the active space can become prohibitely large and a variant, the restricted active space (RASSCF [143]), should be explored. The method keeps the relevant properties of CASSCF but the computational cost is reduced due to the restrictions introduced in the active space, which is divided in 3 subsets: (i) the RAS1 allows a maximum number of holes, (ii) the RAS2 is the active space of a CASSCF calculation, and (iii) the RAS3 allows a maximum number of electrons.

CASSCF and RASSCF only give a small part of the correlation, the non-dynamic correlation. The dynamic correlation is included through perturbation theory (PT) or variationally with multireference configuration interaction (CI).

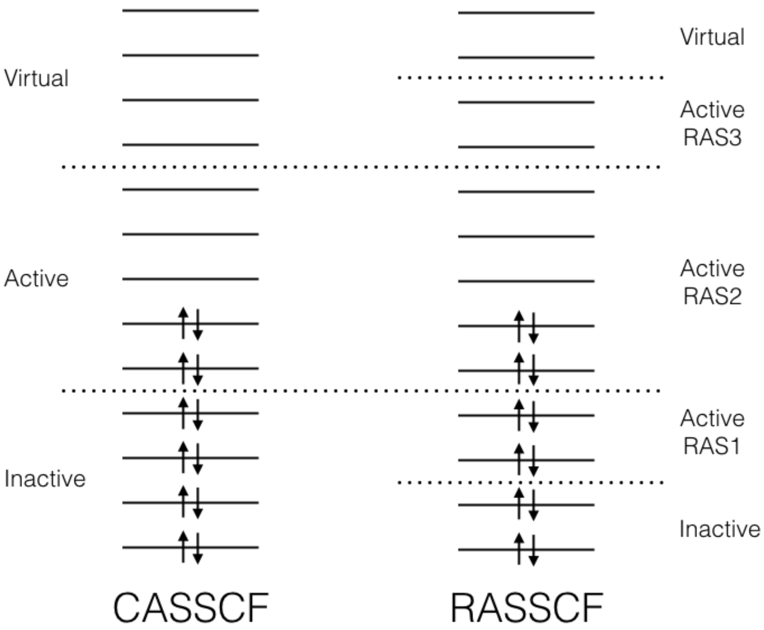

Figure 2.1: Scheme of the MOs classification in the CASSCF and RASSCF spaces.

Perturbation Theory CASPT2/RASPT2

CASPT2 [89, 144] (or RASPT2 [145]) combines the variational treatment of the MC space with of a perturbative correction of the energy using the CASSCF (or RASSCF) wave function as zeroth-order wave function and a Fock-type operator as zeroth-order Hamiltonian.

The first order correction $\Psi^{(1)}$ is constituted by the subspace generated by the single and double excitations from $\Psi^{(0)}$ (V_{SD}) because only these functions interact with $\Psi^{(0)}$. The first-order wave function is generated by applying single and double excitation operators on the CASSCF wave function as a whole. This so-called contracted expansion of the wave function greatly reduces the number of coefficients to be determined but makes more difficult to revise the relative importance of the determinants in the CAS.

$$\hat{E}_{pq}\hat{E}_{rs}\Psi^{(0)} \tag{2.29}$$

The CASPT2 zeroth-order Hamiltonian is defined as:

$$\hat{H}^{(0)} = \sum_{i} \hat{P}_i \hat{F} \hat{P}_i \tag{2.30}$$

where $\hat{F}$ is a Fock-type (monoelectronic) operator and $\hat{P}$ the projection operator onto V_{SD}. The first order function is:

$$\begin{gathered}\left|\Psi^{(1)}\right\rangle = \sum_{pqrs} c_{pqrs}\left|pqrs\right\rangle \\ \left|pqrs\right\rangle \in V_{SD}\end{gathered} \tag{2.31}$$

Afer obtained the first-order wave function, the energy can be obtained by using the second-order correction of energy and the final CASPT2 function is expressed:

$$\begin{gathered}\Psi_{CASPT2} = c_0\left|\Psi^{(0)}\right\rangle + c_1\left|\Psi^{(1)}\right\rangle \\ c_0^2 + c_1^2 = 1\end{gathered} \tag{2.32}$$

The perturbation theory has the problem of intruder states which are excited configurations with similar energy as the reference energy (CASSCF) but with small interactions with the reference space, generating discontinuities and incorrect evaluations of the corresponding contributions to the corrections. A pragmatic solution is using the level shift tecnique [146, 147] which adds a shift parameter to the $H^{(0)}$ and a posteriori correction of $E^{(2)}$.

Difference-dedicated Configuration Interaction

In principle, the difference-dedicated configuration interaction (DDCI) [148, 149] is one of the best computational methodologies to describe energy differences and electronic structures of excited states. It avoids the intruder state problem of CASPT2 and the spin contamination of DFT methods.

The DDCI methodology starts from a CASSCF wave function to generate a multireference configuration interaction (MRCI) space. A general CI wave function can be expressed as:

$$\Psi = c_0\Psi_{(0)} + c_M \cdot M + c_D \cdot D... \tag{2.33}$$

where the $\Psi^{(0)}$ is the reference and M, D, T... symbolize the sets of single, double, triple,... Slater determinants. The dynamic correlation, not included by CASSCF, is obtained by variational treatment. DDCI diagonalizes a subspace of this full CI space by selecting only those determinants that contribute to the vertical energy difference. The selection is made on the basis of second-order perturbation arguments. It is easily shown that determinants external to the CAS only contribute to the energy difference when they simultaneously interact with two different CAS determinants. The Figure 2.2 represents the excitations that are included in the different DDCI variants. The DDCI wavefunction is expressed as:

$$\Psi_k^{DDCI} = \sum_{i \in CAS}^{n} c_{ik}^{DDCI}\phi_i + \sum_{j \notin CAS}^{m} c_{jk}^{DDCI}\phi_j \tag{2.34}$$

where ϕ_i are all the determinants produced by all the possible excitations in active space, and ϕ_j, are all the determinants produced by all the excitations out of the CAS (mono- and diexcitations that include, at least, one orbital of the CAS). The determinants of the CAS should have considerable weight in the DDCI wavefunction, if not, more orbitals should be included in the active space in order to generate more excitations.

The problem of DDCI is the computational cost needed to perform a calculation. To reduce the computational cost without loosing accuracy one can use an extended CAS followed by CAS+S (only singles) or DDCI2 (ionic and neutral determinants: $1h$, $1p$, $1h-1p$, $2h$, $2p$) [119, 150]. In order to facilitate the selection of the orbitals that should be included in the space, localization tools are recommended to be used [151–153]. These procedures let to classify the orbitals as function of the importance that they have in the treatment of the electron correlation [109].

2.3 Model Hamiltonians

The Heisenberg Hamiltonian

The Heisenberg Hamiltonian describes in most cases the low-energy levels of polynuclear magnetic systems with remarkable accuracy. The isotropic and anisotropyc coupling of localized spin moments can be determined by using the general Hamiltonian:

$$\hat{H} = \sum_{i<j} -J_{ij}^{x}\hat{S}_i^x\hat{S}_j^x - J_{ij}^{y}\hat{S}_i^y\hat{S}_j^y - J_{ij}^{z}\hat{S}_i^z\hat{S}_j^z \tag{2.35}$$

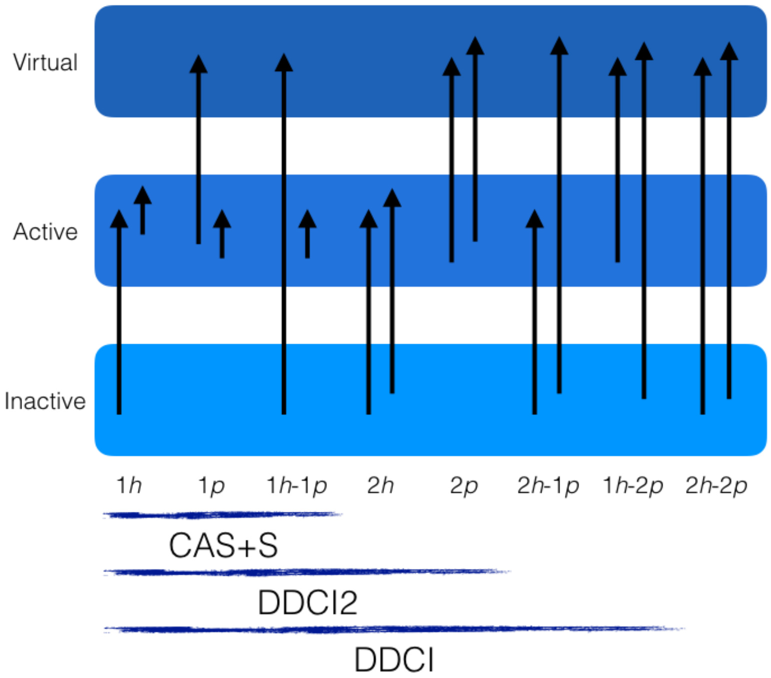

Figure 2.2: Classes of excitations to be added to the CAS space depending on the level of calculation folowing the number of holes (h) and particles (p).

In order to simplify the Hamiltonian, a pure isotropic coupling is considered ($J^x = J^y = J^z = J$), reducing the expression to the so-called Heisenberg Hamiltonian.

$$\hat{H} = \sum_{i<j} -J_{ij}\hat{S}_i\hat{S}_j \tag{2.36}$$

The Heisenberg Hamiltonian is expressed as the sum of exchange interactions between sites i and j, where the $\hat{S}_i$ and $\hat{S}_j$ are spin operators without preferential orientation in the three-dimensional space, and J_{ij} is the spin exchange parameter measuring the strength of the interaction between sites i and j. The eigenfunctions of the Heisenberg Hamiltonian are also eigenfunctions of $\hat{S}^2$, and consequently, there exists a relation between the computed energy eigenvalues of the different spin states and the magnetic exchange coupling parameter following the expression $E(S-1)-E(S) = SJ$.

The Ising Hamiltonian

We can simplify the model Hamiltonian using the Ising restriction which imposes that $J^x = J^y = 0$ and the Hamiltonian only depends on the z-axis.

$$\hat{H} = \sum_{i<j} -J_{ij}\hat{S}_i^z\hat{S}_j^z \tag{2.37}$$

The difference with the Heisenberg Hamiltonian is that the spin part of the wavefunction is not necessarily an eigenfunction of $\hat{S}^2$. This is of great use when considering extended systems (solids), where the spin eigenfunctions of the lower spin multiplicities cannot be written down anymore, and the Heisenberg Hamiltonian looses it significance.

The Zero-field Anisotropic Spin Hamiltonian

In some cases the spin moment is not isotropic as assumed in the Heisenberg Hamiltonian. The alignment of the spin moment along the different magnetic axes results in non-degenerate energy eigenvalues. The most important (but definitely not the only) source of spin anisotropy is the so-called single ion anisotropy described with the following model Hamiltonian:

$$\hat{H}_{ZFS} = \hat{S}D\hat{S} \tag{2.38}$$

where $\hat{S}$ is the total spin operator and D is the zero-field splitting (ZFS). Expanding $\hat{S}$ in its x, y, and z-components and assuming that the trace of D=0, the Hamiltonian can be rewritten in a more practical form as:

$$\hat{H}_{ZFS} = D(\hat{S}_z^2 - \frac{1}{3}\hat{S}^2) + E(S_x^2 - S_y^2) \tag{2.39}$$

where D is the axial anisotropy parameter (how different is z with respect to x and y) and E is the rhombic anisotropy parameter (how different are x and y). The derivation of this model Hamiltonian assumes that the electronic state has no first-order orbital moment and the splitting of M_S components arises from the spin-orbit coupling with excited states.

Other magnetic anisotropic interactions such as higher-order single ion anisotropy, the anisotropic and asymmetric exchange can also be described with well-established model Hamiltonians but this goes beyond the scope of the present thesis.

CHAPTER 3

On the Role of Solvent Effects on the Electronic Transitions in Fe(II) and Ru(II) Complexes

3.1 Introduction

Over the last decades important advances have been made toward the synthesis of systems with bistability under normal conditions for which the switching is fast and both states sufficiently long-lived to take profit of the bistability. A system capable of persistently changing its magnetic or electric properties upon some external stimulation has many potential technological applications, for example to make nano-switches or as memory devices. In this area of research, the compounds with an interconversion between two different spin states –spin crossover (SCO)– that can be triggered by a change in temperature, pressure or irradiation with light, form an important group. From the applicability point of view, the method that offers optimal control on the process is the light induced variant. This process, also known as light-induced excited spin state trapping (LIESST), was discovered in the 1980s [57, 58] and the basic mechanism was elucidated shortly afterwards [30, 154]. Important ingredients to explain the occurrence of LIESST are (i) the energy difference between the high-spin (HS) and low-spin (LS) states; (ii) the vertical excitation energies of the metal-to-ligand charge transfer (MLCT) and ligand-field (LF) states and (iii) coordination degree of the ligand; cooperativity, among other factors [155–157].

Theoretical investigations have focussed on many of these aspects, but especially the determination of the energy difference between the HS and LS state has attracted much attention. The pioneering work of Paulsen and co-workers [82] established that standard density functional theory calculations are not accurate enough to precisely predict the stability of the HS state with respect to the LS state (ΔE_{HL}) in mononuclear SCO complexes. Over the past decade, calculations have proven that even the best current DFT functionals can display large errors for specific types of transition metal energetics. In particular, standard pure functionals (like LDA, BLYP, or PBE) systematically overstabilize low-spin states, while hybrid functionals (like B3LYP, or PBE0) overstabilize high-spin states due to the inclusion of a portion of Hartree-Fock exchange. The B3LYP* and OPBE functionals have emerged as most likely candidates for use in SCO complexes. Reiher and co-workers [83] suggested a reduction of the amount of HF exchange to 15% in B3LYP functional, B3LYP*, but this change is not successful for all iron compounds. Swart and co-workers studied different combinations of the exchange and correlation functionals and found that the OPBE functional [85, 86] which is the combination of Handy's optimised exchange (OPTX) with the PBE correlation (PBEc) correctly predicts the lowest spin state in many transition-metal complexes. Therefore the appropiate amount of HF exchange is *a priori* unknown to be predictive for transition-metal complexes.

There are also several studies devoted to SCO based on post Hartree-Fock methodologies. These strategies are based on a multiconfigurational description of the electronic structure and allow one to consider pure spin eigenfunctions, to treat ground and excited states on an equal footing, and include spin-orbit coupling effects. A standard implementation of multiconfigurational self-consistent field (SCF) calculations is given by the complete active space (CASSCF) [88]. Combining CASSCF with multiconfigurational second-order perturbation theory (CASPT2) [89] results in a very successful computational scheme to treat transition metal complexes. The CASSCF wave function gives a good description of the electron distribution but lacks important dynamical electron correlation effects. This does not strongly affect the electron distribution but may give rise to rather large changes in the relative energies of the different electronic states. The complete active space second-order perturbation theory (CASPT2) accounts for dynamic electron correlation in the case of multiconfigurational wave functions of medium to large sized systems.

Since LIESST is intimately related to the local properties of the Fe(II) complex, especially to the first coordination sphere of the central metal, most theoretical studies rely on an isolated, *gas phase* molecule approach. The role of the environment (long-range electrostatic interactions, solvent effects) have been less studied, although the study of Robert and co-workers for thermal SCO is a nice example how theory can quantify the effect of interactions that go beyond the simple isolated molecule description [158]. One important ingredient of LIESST that is possibly strongly dependent on the description of the environment is the vertical excitation spectrum of the initial LS state. Actually, the study of the transient absorption spectroscopy study of Tribollet *et al.* on $[Fe(phen)_3]^{2+}$ (phen=1,10-phenanthroline) points to important solvent effects on the excitation energies [17]. This was based on the mismatch of approximately 0.3 eV between the relative energies measured in experiment and those calculated for the related compound $[Fe(bpy)_3]^{2+}$ (bpy=2,2'-bipyridine) with a multiconfigurational approach applied to the isolated complex [16, 60].

To settle the importance of the solvent effects on the vertical excitation spectrum and explain the difference in calculated and observed transition energies, we investigate the electronic states of $[Fe(phen)_3]^{2+}$, trans(Cl)-$Fe(bpy)Cl_2(CO)_2$ and trans(Cl)-$Ru(bpy)Cl_2(CO)_2$ (depicted in Figure 3.1), comparing vacuum results with those obtained in a model that accounts for solvent effects. Furthermore, we compare time-dependent DFT to CASPT2 results in order to establish the viability of the simpler, and computationally more efficient DFT based method. The second and third complexes do not belong to the class of SCO materials, but were chosen as benchmark models. The Ru-compound has recently been studied with TD-DFT and to some extent with CASPT2 [159]. Important solvent effects have been observed, along with blue-shifting of some specific MLCT states by approximately 1 eV.

3.2 Computational Information

All geometries were optimized using the hybrid functional PBE0 [136], which adds 25% of exact Fock exchange to the standard PBE functional. This functional has been used previously, giving good results for the geometrical parameters for related SCO complexes [62, 160]. The molecular orbitals were expanded with the default triple-ζ basis set with one polaritzation function (def2-TZVP) [161].

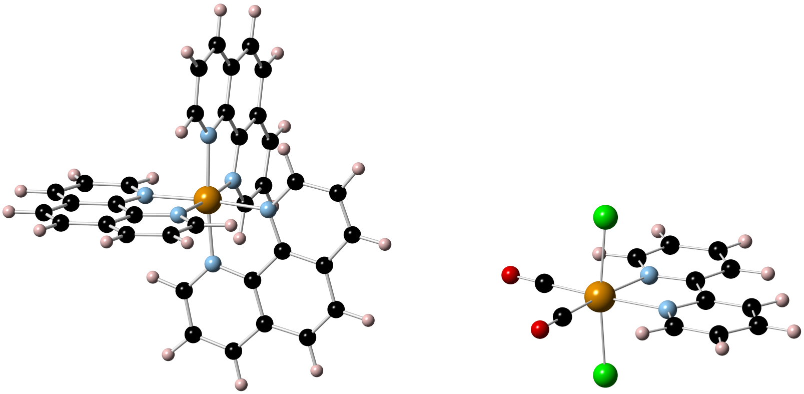

Figure 3.1: Ball and stick presentation of the complexes studied in this chapter: (left) $[Fe(phen)_3]^{2+}$**(1)**, (right) trans(Cl)-Fe(bpy)$Cl_2(CO)_2$**(2)** and trans(Cl)-Ru(bpy)$Cl_2(CO)_2$**(3)**. Color code: orange for Fe and Ru, red for O, green for Cl, black for C, blue for N and pink for H.

The optimal geometry of the HS and LS states of the three complexes was determined by optimizing all geometrical variables without symmetry constraints and characterized as minima by a vibrational frequency calculation. The geometries used to build the energy potential curves of the ground state around the LS DFT geometry were generated from restricted geometry optimizations, fixing the Fe-N distances at different values in an interval of 1.8 to 2.0 Å. Time-dependent DFT calculations were performed within the full random phase approximation (RPA) [162]. Additionally, calculations in solution were performed using H_2O or acetonitrile as solvent with the dielectric continuum model COSMO [163]. All DFT calculations were carried out using the TURBOMOLE package [164, 165] version 6.3.

CASSCF/CASPT2 calculations were performed as implemented in the MOLCAS 7.4 package [166, 167]. Atomic natural orbital (ANO) basis sets optimized for scalar relativistic effects and core correlation were applied for all atoms [168, 169]. For complex **1**, we used a (7s,6p,5d,4f,3g,2h) contraction for Fe, (4s,3p,1d) for N, (3s,2p) for C and (2s) for H. For complex **2**, the ANO basis is the same but for C and O, which is (4s,3p,1d) and the basis set for Cl is contracted to (5s,4p,1d). Complex **3** has the same basis set contraction. The Cholesky decomposition [170, 171] was used to reduce the computational cost associated to the calculation of the two-electron integrals. Scalar relativistic effects were included using Douglas-Kross-Hess Hamiltonian [172]. Spin-orbit coupling and oscillator strengths of the electronic transitions were calculated with the state interaction approach [173, 174].

Different active spaces were used to construct the CASSCF reference wave function depending on the complex or the transitions studied. For complex **1** three active spaces were used. The first active space contains 10 electrons distributed in all possible ways over 12 orbitals; five orbitals with mainly Fe–3d character, two σ-bonding orbitals with important contributions on the lone pairs of N, and five orbitals that account for the double shell effect of the 3d-shell, the so-called 3d' orbitals. This active space has been used in many applications on TM complexes before and provides a balanced description of all the important non-dynamic electron correlation [89, 174, 175]. The next active space extends the previous one with three ligand π^* orbitals leading to an active space of 15 orbitals and 10 electrons. The inclusion of these orbitals permits the study of MLCT states. Finally, the last active space was used to analyze the ligand-centered excitations in the π-system. It includes 12 ligand orbitals, six occupied ligand π orbitals and six unoccupied ligand π^* orbitals, for a total of 12 electrons. For complex **2** only one active space was used. It contains 10 electrons in 14 orbitals; the Fe-3d and 3d' orbitals, two σ-bonding ligand orbitals and two π^* orbitals of the carbonyl ligands. The inclusion of π^* orbitals of the pyridine ligand is unfortunately not possible without running into CAS spaces that are unmanageable in size. A similar problem occurs for **3**. The study of Escudero and González on trans(Cl)-Ru(bpy)$Cl_2(CO)_2$ showed that only with an active space of 22 electrons and 21 orbitals, excitations could be calculated involving the three different ligands. Here, we restricted ourselves to the excitations involving the pyridine ligand, which can be done with an active space of 14 electrons in 13 orbitals (5 Ru-4d orbitals, 4 pyridine π orbitals and 4 pyridine π^* orbitals). The active orbitals of al cases are graphically represented in the *Chapter3: Sup. Info.* of the ioChem-BD database [176] collection (DOI:10.19061/iochem-bd-2-3).

CASPT2 calculations account for the remaining electron correlation by correlating all the electrons except the deep core electrons ($1s^2$ for N and C and $1s^2 2s^2 2p^6$ for Fe). In order to exclude possible intruder states, we applied an imaginary level shift of 0.15-0.25 a.u. in CASPT2 [147]. The solvent effects were taken into account in the CASSCF/CASPT2 calculations with the polarizable continuum model (PCM) [177–179].

Finally, we have analyzed the wave function for all complexes in an orthogonal valence bond picture [180, 181]. For this purpose, the natural active orbitals are transformed into orthogonal localized orbitals with either exclusively Fe/Ru or ligand character following the procedure described in Ref. [182], which is based on pair-wise rotations of bonding and anti-bonding metal-ligand orbitals.

3.3 Results and Discussion

Geometries and Adiabatic Energy Differences

The geometry of the isolated complex **1** was optimized for the three lowest electronic states with different spin coupling of the $3d^6$ manifold of the Fe^{2+} ion: singlet (LS), triplet (IS) and quintet (HS). The DFT calculations for the triplet and quintet were performed within the spin-unrestricted formalism, and hence, the resulting electronic states are not necessarily eigenfunctions of the $\hat{S}^2$ operator. However, the spin functions considered here are essentially mono-determinantal and the spin contamination is very small. The expectation values of $\hat{S}^2$ for HS and IS, 6.02 and 2.03, are close to the formal values of 6 and 2.

In line with the findings of previous studies, the optimized bond lengths of **1** are slightly overestimated by 0.02 Å for LS and 0.05 Å for HS in comparison with the experimental values of 1.98 Å for LS and 2.15 Å, respectively [183]. This overestimation is caused by the hybrid functional used, the inclusion of 25% exact Fock exchange makes the bond slightly too weak [160]. Nevertheless, the bond elongation upon the LS to HS conversion of 0.2 Å is in agreement with experiment, as expected. The PBE0 adiabatic energies of the HS and IS states of -0.15 eV and 0.51 eV for **1**, and 0.12 eV and 0.58 eV for **2**. The fact that both compounds have a LS ground state at low temperatures shows that the PBE0 functional tends to overstabilize the open-shell configurations with respect to the closed shell singlet state [85, 86, 184].

Additional optimizations were done taking into account the solvent effects, but neither water nor acetonitrile introduces significant changes in the geometries or relative energies. The Fe–N distances remain practically the same and the overstabilization of the HS state is reduced only by 0.06 eV, which does not repair the erroneous behaviour of the hybrid functional, maintaining the HS as ground state.

TD-DFT Absorption Spectrum of $[\mathrm{Fe(phen)_3}]^{2+}$

The lowest part of the absorption spectrum of the LS state contains basically three types of excitations: (i) ligand-field or metal centered (MC) transitions involving electron replacements within the Fe-3d orbitals; (ii) metal-to-ligand charge transfer transitions (MLCT) in which an electron is transferred from Fe to an antibonding orbital on the ligands, and (iii) excitations entirely localized on the ligands, the ligand centered (LC) transitions involving the π

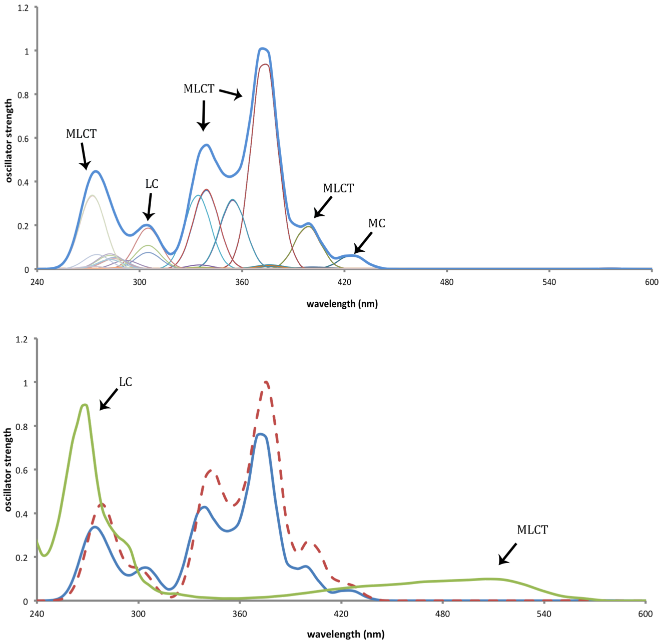

Figure 3.2: Top: TD-DFT PBE0/def2-TZVP absorption spectrum for $[Fe(phen)_3]^{2+}$ in vacuum representing the transitions by a Gaussian function. Bottom: Comparison between vacuum (solid blue line), water (dashed line) and the experimental spectrum [17] (solid green line).

and π^* orbitals of phenantroline. In addition to the relative energies and intensitites of these transitions, we also establish to what extent the spectrum is affected by the inclusion of solvent effects.

First, we will make a complete analysis of the 40 lowest singlet excitations of the complex in vacuum and in solution (H_2O) using the TD-DFT method[1]. Figure 3.2 summarizes in a graphical

---

[1] The increased computer resources made it possible to extend the num-

way the results by representing each transition with a gaussian-type function of full-width at half-maximum of 25 nm. The height of each peak is normalized to the peak with the largest oscillator strength. The top figure shows the results for **1** in vacuum, the colored thinner lines represent the individual transitions and the sum of these is represented with the thicker line. The calculated absorption spectrum shows three main absorption bands and also three less intense shoulders. The main bands are localized around 270, 340 and 370 nm, and correspond to MLCT transitions that involve electron replacements in the Fe-3d orbitals and π^* ligand orbitals. The intensity of these bands is in concordance with their dipole allowed character. The band centered at 310 nm is formed by a collection of nearly degenerate ligand-centered transitions among the π and π^* orbitals of the ligand. These excitations are also optically allowed. TD-DFT/PBE0 predicts a slightly less intense absorption with respect to the MLCT states, contrasting experimental data, which clearly point at more intense LC excitations [17]. Finally, the metal-centered Fe-3d transitions appear around 420 and 570 nm but they are very weak due to the nearly octahedral coordination sphere of the Fe^{2+} ion (forbidden d-d transition). Note that the absence of absorption at shorter wave lengths ~260 nm is due to the limiting the calculation to the first 40 singlet states. Determining more roots would most probably lead to finite intensities at these shorter wave lengths.

The lower part of Figure 3.2 compares the vacuum calculation to

---

ber of roots up to 200 singlets after the population of these results. The interpretation of the PBE0 results has changed somewhat, as discussed in the "Post-publication" section.

the results obtained with solvent effects modelled with a COSMO representation of water. As can be seen, the effect of the environment on the excitation energies and intensities is rather small. The basic features of the spectrum are maintained and at this stage, we conclude that the solvent effects on the geometry, and the adiabatic and vertical excitation energies are small. However, there is an important issue that still needs to resolved; the overall agreement between the TD-DFT and the experimental spectrum (green line in Figure 3.2, bottom) is not very satisfactory. Therefore, we checked the effect of the solvent on the excitation energies with CASPT2, which in principle should provide more accurate results.

CASPT2 Absorption Spectrum of $[\mathrm{Fe(phen)}_3]^{2+}$

From previous studies, it is well-known that the optimal CASPT2 Fe–N distance does not necessarily coincide with the one of the optimized DFT geometry [60, 175, 185, 186]. Since the excitation energies are rather sensitive to this parameter (especially the MC excitations), we have manually determined the optimal CASPT2 distance in the field of DFT relaxed ligand geometries by generating a set of DFT optimized geometries with different Fe–N distances and calculated the CASPT2 energy of the LS state at all points with a CAS(10,12) reference wave function. Note that a full CASPT2 geometry optimization is computationally too expensive, and would probably not provide extra information. The multiconfigurational character of the wave function is basically related with the electronic configuration of Fe and the Fe–N bond. The optimization of the ligand geometry with CASPT2 would not bring new information to that provided by DFT.

The scan of the Fe–N distance locates the optimal CASPT2 Fe–N distance at 1.92 Å, significantly shorter than obtained with DFT and determined from X-ray diffraction measurements. As can be seen in Table 3.1, the relative energies of the lowest d-d transitions strongly depend on the geometry. For shorter distances, the ligand field is stronger and the MC excited states become higher in energy. In addition, the $^{2S+1}\Gamma$ is not strictly degenerate, being slight splittings observed (*e.g.*, 0.1 eV in $^5T_{2g}$).

The full absorption spectrum was obtained in a two step procedure. In the first place, we used the CAS(10,15) reference wave function to obtain simultaneously CASPT2 estimates of the MC and MLCT excitation energies and intensities. The LC excitations were subsequently added by performing CASPT2 calculations with the CAS(12,12) reference wave function and the results are summarized in Table 3.2. The lowest MLCT states appear around 2.60 eV, slightly higher than the spin-allowed MC excitations. The oscillator strength of the latter is however two orders of magnitude smaller and is hardly detectable in the graphical representation of the CASPT2 absorption spectrum constructed in the same way as the TD-DFT/PBE0 spectrum discussed above. MLCT states are found in a rather broad interval ranging from 475 nm (2.61 eV) to approximately 330 nm (3.76 eV). At shorter wave length, we find very intense LC excitations. Again, the results in vacuum (solid

Table 3.1: CASPT2 vertical transition energies (in eV) of the lowest electronic MC transitions of $[\mathrm{Fe(phen)_3}]^{2+}$ at the DFT optimized Fe-N distance (2.00 Å) and the CASPT2 optimal distance (1.92 Å). The reference wave function is obtained from a CAS(10,12) calculation. Results in parenthesis correspond to those obtained with the PCM solvent model for water.

State	DFT optimized 2.00 Å	CASPT2 optimized 1.92 Å
$^1A_{1g}$	0.00 (0.00)	0.00 (0.00)
$^5T_{2g}$	0.92 (0.92)	2.43 (2.43)
	0.93 (0.93)	2.43 (2.43)
	1.02 (1.02)	2.43 (2.43)
$^3T_{1g}$	0.99 (0.99)	1.71 (1.72)
	1.03 (1.03)	1.74 (1.74)
	1.03 (1.03)	1.80 (1.80)
$^3T_{2g}$	1.51 (1.51)	2.27 (2.27)
	1.53 (1.53)	2.30 (2.30)
	1.61 (1.61)	2.36 (2.36)
$^1T_{1g}$	1.91 (1.91)	2.62 (2.62)
	1.96 (1.96)	2.66 (2.66)
	1.97 (1.97)	2.69 (2.69)
^5E	3.44 (3.44)	5.65 (5.65)
	3.45 (3.45)	5.66 (5.66)

line) were compared to the results obtained after including solvent effects through a PCM treatment of water or acetonitrile (dashed curve, no difference between the two solvents). Whereas the relative energies of the transitions are hardly affected by the solvent, the oscillator strengths of some states is somewhat diminished, most specifically the states that contribute to the peak around 400 nm. Nevertheless, the overall shape of the absorption spectrum is maintained and the solvent effects are also small for the CASPT2 calculations

This brings us to the last point; the comparison of the CASPT2 results with the experimental spectrum, represented by the green thick line in Figure 3.3. The overall agreement is rather satisfactory and much better than the one obtained with TD-DFT/PBE0. The main features of the spectrum are correctly reproduced and the only obvious discrepancy lies in the on-set of the bands. Experimentally, the MLCT band starts around 550 nm (2.30 eV) and the LC band around 275 nm (4.50 eV), while CASPT2 places the onset at 450 nm (2.60 eV) and 250 nm (4.96 eV), respectively. This behaviour is similar to the one observed in $[Fe(bpy)_3]^{2+}$, where an almost identical difference in the lowest MLCT excitation energy was found [60].

Solvent Effects for trans(Cl)-Fe(bpy)$Cl_2(CO)_2$ and trans(Cl)-Ru(bpy)$Cl_2(CO)_2$

Although the results discussed so far indicate that the solvent effects on the absorption spectrum of $[Fe(phen)_3]^{2+}$ are small, there

Table 3.2: CASPT2 vertical excitation energies ΔE (in eV) of the lowest electronic transitions of $[\mathrm{Fe(phen)_3}]^{2+}$ (**1**). MC and MLCT are calculated with a CAS(10,15) reference wave function, and LLCT with a CAS(12,12) reference wave function.

State	ΔE (vacuum)	ΔE (water)
^{1}A$_{1g}$	0.00	0.00
1 ^{1}MC	2.59	2.59
1 ^{1}MLCT	2.60	2.58
2 ^{1}MLCT	2.77	2.74
3 ^{1}MLCT	3.06	2.89
4 ^{1}MLCT	3.08	3.35
5 ^{1}MLCT	3.29	3.24
2 ^{1}MC	3.54	3.58
1 ^{1}LLCT	5.20	5.26
2 ^{1}LLCT	5.21	5.30
3 ^{1}LLCT	5.32	5.43
3 ^{1}MC	5.53	5.53
4 ^{1}MC	5.60	5.60
5 ^{1}MC	5.67	5.66
6 ^{1}MC	5.81	5.82
4 ^{1}LLCT	6.26	6.27
5 ^{1}LLCT	6.33	6.30

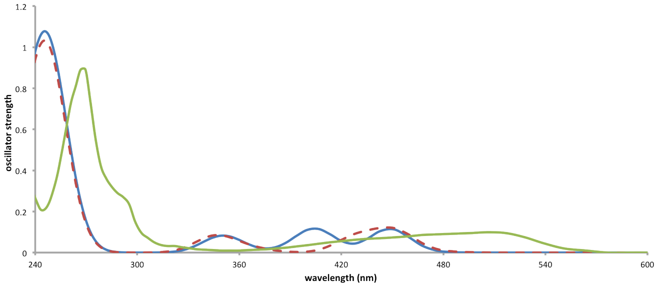

Figure 3.3: CASPT2 absorption spectrum of $[Fe(phen)_3]^{2+}$ (**1**) representing the transitions by a Gaussian function (solid blue line) in vacuum and (dashed lines) in water. The solid green line represents the absorption spectrum obtained experimentally.

are of course several cases where solvent effects play a very important role and cannot be omitted in the theoretical description of the electronic structure. A recent example is given by the calculations of Escudero and González on trans(Cl)-Ru(bpy)$Cl_2(CO)_2$ [159]. The TD-DFT results with and without solvent effects show differences in the excitation energies as large as 1 eV. To double check the computational strategy applied here for $[Fe(phen)_3]^{2+}$, we have applied it to the mentioned Ru complex (**3**) and to a variant of it, by changing Ru for Fe (**2**).

The geometry optimization of trans(Cl)-Ru(bpy)$Cl_2(CO)_2$ with PBE0/def2-TZVP gives accurate bond distances and angles (more information in Table S4.1 of *Chapter3: Sup. Info.* of the ioChem-bd, DOI:10.19061/iochem-bd-2-3). Hence, it is expected that the optimized geometry of the hypothetical complex trans(Cl)-Fe(bpy)$Cl_2(CO)_2$ is also reasonable. Table 3.3 lists the TD-DFT results for **2** and **3** with and without solvent effects. The results for the Ru complex are in close agreement with those obtained by Escudero and González and important solvent effects are observed for some of the states. The largest changes in the excitation energies occurs for the MLCT states and less important effects are observed for the LC and MC excitations. The excitations in which an electron is transferred from Cl or CO to bipyridine (ligand-to-ligand charge transfer (LLCT) are also affected, whereas the LLCT excitations among CO and Cl are not influenced by the solvent. A similar picture arises from the TD-DFT calculations on **2**: the relative energy for several MLCT states show large solvent effects, while this is less pronounced for the LC and MC states. As soon as the LLCT excitations involve bipyridine orbitals, the excitation energy is significantly blue-shifted. Note that in some cases the classification of the excitation as MLCT, LLCT, etc. is not straightforward, since the Kohn-Sham orbitals exhibit a certain degree of delocalization and are not easily identified as Fe or ligand orbitals. Moreover, many excitations show several contributions with similar weights.

Subsequently, we have applied the CASPT2 methodology to **2** and **3** and compared the vacuum results to those obtained with a PCM modelling of the solvent (water and acetonitrile). Table 3.4 summarizes the results obtained for both complexes. The MLCT states for **2** involve electron replacements from Fe to the antibonding orbitals of the CO ligands, while the excitations labeled as MLCT in **3** correspond to electron transfer from Fe to the π^* orbitals of pyridine. This is due to the impossibility to include empty orbitals of all the different ligands in the active space. The Ru-complex has low-lying pyridine orbitals, while for the Fe analogue the CO antibonding π^* orbitals enter the active space preferentially. In these complexes the LC and LLCT excitations have not been calculated. This would require a complete new CASSCF reference wave function as done for $[\text{Fe(phen)}_3]^{2+}$, but not essential to illustrate the solvent effects in **2** and **3**.

The solvent effects calculated with CASPT2 are similar to those observed in the TD-DFT calculations, varying from approximately 0.1 eV for MC states to nearly 1 eV for the MLCT states of **3**, which involve the bipyridine ligand orbitals. The MLCT states in **2** are due to electron replacements from Fe to π^*_{CO} and their relative energy remain nearly constant when the solvent is added. Hence, the computational scheme is capable of accounting for solvent effects when they are present and the absence of their manifestation in **1** is not due to artefacts in the method.

An important parameter to explain the energy shifts is the dipole moment. In Table 3.5, we summarize the dipole moments calculated as the expectation value of the CASSCF wave function and the effect of the solvent on the relative energies for a collection of states in the three complexes considered. It is clear that changes in the excitation energy are closely related to the difference of the dipole moment between ground and excited states. In the case of $[\text{Fe(phen)}_3]^{2+}$, the ground state has an almost zero dipole moment and none of the excited states gains a large dipole moment. This is expected for the MC states, but less obvious for MLCT states. The antibonding π orbitals on the phenantroline ligands in the active space (those that become occupied in the MLCT states) are delocalized over one, two or three ligands. In all cases, the MLCT states are linear combinations of single electron replacements such that the overall transfer from the metal to the ligands is symmetric in all three directions, and hence, no dipole is induced by the excitation. This explains the minimal effect on the excitation energies when the solvent is included in the calculation. On the contrary, the less symmetric complexes **2** and **3** with three different ligands coordinating the metal have a large dipole moment in the ground state pointing from the metal to the bipyridine ligand. The dipole moment is largely canceled when an electron is transferred from the metal to the bipyridine ligand. This induces a large response of the solvent, and hence, shifts the excitation energy in comparison to the value calculated in vacuum. When the electron is excited to the antibonding orbitals of the CO ligands, the change in the dipole moment is smaller, which explains the weaker solvent effects for these MLCT states.

Orthogonal Valence Bond Analysis of the Wave Function

Having confirmed that the solvent effects on the excitation energies are intimately related to changes in the dipole moment of the initial and final states involved in the transition, it is interesting to see whether the solvent has any effect on the electronic structure of the ground state. To this purpose, we analyze the wave function of the LS, with and without solvent in the framework of orthogonal Valence Bond. Instead of the more common natural orbitals, the

Table 3.3: TD-DFT vertical excitation energies ΔE (in eV) of **2** and **3**. XLCT indicate charge transfer excitations involving the Cl ligand.

	2		**3**	
State	ΔE (vacuum)	ΔE (water)	ΔE (vacuum)	ΔE (water)
Ground state	0.00	0.00	0.00	0.00
1^1XLCT/MLCT $n_{\mathrm{Cl}}/d_{t2g}\rightarrow\pi^*_{\mathrm{bpy}}$	2.66	3.71	2.36	3.33
2^1XLCT/MLCT $n_{\mathrm{Cl}}/d_{t2g}\rightarrow\pi^*_{\mathrm{bpy}}$	2.74	4.19	2.49	3.47
1^1XLCT/MC $n_{\mathrm{Cl}}/d_{t2g}\rightarrow\pi^*_{\mathrm{CO}}/d_{eg}$	2.95	3.17	3.95	4.28
2^1XLCT/MC $n_{\mathrm{Cl}}/d_{t2g}\rightarrow\pi^*_{\mathrm{CO}}/d_{eg}$	3.11	3.31	4.10	4.44
1^1LLCT $n_{\mathrm{Cl}}\rightarrow\pi^*_{\mathrm{bpy}}$	3.51	4.62		
1^1MLCT $n_{\mathrm{Cl}}/d_{\mathrm{t2g}}\rightarrow\pi^*_{\mathrm{CO}}$	3.60	3.61		
3^1XLCT/MLCT $n_{\mathrm{Cl}}/d_{t2g}\rightarrow\pi^*_{\mathrm{bpy}}$	3.62	4.81	3.29	4.28
4^1XLCT/MLCT $n_{\mathrm{Cl}}/d_{t2g}\rightarrow\pi^*_{\mathrm{bpy}}$	4.19	4.56	3.56	4.57
1^1XLCT/LLCT $n_{\mathrm{Cl}}/d_{t2g}\rightarrow\pi^*_{\mathrm{CO}}$ $\pi_{\mathrm{bpy}}\rightarrow\pi^*_{\mathrm{bpy}}$	4.46	4.76	4.48	4.42
2^1XLCT/LLCT $n_{\mathrm{Cl}}/d_{t2g}\rightarrow\pi^*_{\mathrm{CO}}$ $\pi_{\mathrm{bpy}}\rightarrow\pi^*_{\mathrm{bpy}}$	4.58	5.04		

Table 3.4: CASPT2 vertical transition energies ΔE (in eV) of **2** and **3**. The MLCT excitations in **2** correspond to excitations from Fe-3d(t_{2g}) to π^*_{CO} and in **3** to π^*_{bpy}

	ΔE **2**		ΔE **3**	
State	(vacuum)	(water)	(vacuum)	(water)
$^1A_{1g}$	0.00	0.00	0.00	0.00
1^1MC	2.34	2.30	4.15	4.24
2^1MC	3.76	3.85	4.01	4.24
3^1MC	3.38	3.53	4.51	5.19
4^1MC	4.15	3.99	5.14	5.51
1^1MLCT	4.38	4.50	3.87	4.84
2^1MLCT	4.61	4.60	3.90	4.64
3^1MLCT	5.29	5.30	4.59	5.39
4^1MLCT	5.92	5.92	n/a	n/a

Table 3.5: Changes in the CASPT2 vertical transition energies $\Delta(\Delta E)$ (in eV) and the dipole moment $|\Delta\mu|$ (in Debye) of **1**, **2** and **3** between vacuum and solution.

	1		**2**		**3**	
State	$\Delta(\Delta E)$	$\|\Delta\mu\|$	$\Delta(\Delta E)$	$\|\Delta\mu\|$	$\Delta(\Delta E)$	$\|\Delta\mu\|$
1^1MC	0.00	0.16	0.04	0.37	0.09	0.94
2^1MC	0.04	0.34	0.09	0.74	0.33	0.28
3^1MC	0.00	0.14	0.15	0.16	0.68	0.20
4^1MC	0.00	0.08	0.16	0.35	0.37	1.08
1^1MLCT	0.02	4.48	0.12	2.50	0.97	6.89
2^1MLCT	0.03	2.54	0.01	2.44	0.74	7.73
3^1MLCT	0.17	2.08	0.01	2.61	0.80	5.52
4^1MLCT	0.27	2.11	0.00	3.01	n/a	n/a

Table 3.6: Orthogonal Valence Band decomposition of the CASSCF wave function of the LS state for **1**, **2** and **3** expressed in weights of different TM-d^n L^m electronic configurations (n+m equals the number of active electrons). Results in vacuum are compared with a PCM modelling of the solvent.

Complex		Electronic configuration				
		d^6 L^4	d^7 L^3	d^8 L^2	d^9 L^1	Total
1	vacuum	55.0	33.9	8.3	2.1	99.3
	water	55.0	33.8	8.3	2.1	99.2
2	vacuum	18.7	44.7	26.0	8.0	97.4
	water	18.7	44.7	25.9	7.9	97.2
3	vacuum	9.7	39.9	38.3	11.2	99.1
	water	9.6	39.9	38.4	11.2	99.1

CASSCF wave function is expressed in localized orbitals obtained by a unitary transformation [182]. Using these localized orbitals (shown in Figures S5.1 and S6.1 of *Chapter3: Sup. Info.* of the ioChem-bd, DOI:10.19061/iochem-bd-2-3), it is possible to mark the configuration state functions of the CASSCF wave function by the number of electrons associated to the metal ion. This is not possible when the function is expressed in natural orbitals which are much more delocalized over metal and ligands.

Table 3.6 reports the decomposition of the LS wave function for all three compounds. It can be readily seen that there is practically no difference between the vacuum and solvent results. This indicates that the wave function of the fundamental state does not change when solvent effects are included in the electronic structure. More interesting is the comparison between the three different compounds. Assuming an ionic picture with a formal TM(II) state, the TM-d^6 state should be the leading electronic configuration. This is true to some extent for **1**, but cannot be maintained for the other two complexes. In these cases the CO ligand provides a much stronger σ donation than the phenantroline ligands, leading to very low weights of the ionic configuration. This effect is slightly stronger in the Ru complex due to the larger spatial extent of the TM-4d orbitals. The weight of the ionic determinant has been found to be an indication of the possibility for SCO [187]. Normally, SCO compounds exhibit weights on the d^6 conficuration of roughly 55%. This is indeed compatible with the SCO character of **1**, while it excludes any kind of such phenomena for the other two complexes, for which σ donation is large, thus ionic is lowered and no SCO is possible. The adiabatic energy difference between LS and HS is too large is these cases [187].

3.4 Conclusions

The purpose of this work was to investigate theoretically the solvent effects on the electronic states of $[Fe(phen)_3]^{2+}$, trans(Cl)-Fe(bpy)$Cl_2(CO)_2$ and trans(Cl)-Ru(bpy)$Cl_2(CO)_2$, comparing (TD-)DFT to CASPT2 results. Because the results obtained with TD-DFT for all the transitions differ from the values obtained with CASPT2 and do not compare well with the available experimental data, the hybrid TD-DFT/PBE0 cannot be recommended as an alternative for the study of the excited states.

CASPT2 results of $[\mathrm{Fe(phen)_3}]^{2+}$ compare much better with experiment. The theoretical absorption spectrum places the MLCT and the LC bands slightly higher in energy than experimentally measured, which can be explained by the use of the ideal geometry in which the three phenantroline ligands are identical, leading to delocalized MLCT states with slightly higher energy that the ones that are localized on one ligand.

The solvent effects were treated with the COSMO model for (TD)-DFT, and with PCM for the CASPT2 calculations. The results obtained show that solvent effects are only important when the dipole moment between initial and final state changes significantly. The transitions of $[\mathrm{Fe(phen)_3}]^{2+}$ are not affected by the introduction of solvent effects due to the high symmetry of the complex. On the other hand, the MLCT of the complex **2**, that involve the bipyridine ligand, are affected due to the asymmetric charge transfer involved in these transitions. The excitations that involve the carbonyl ligand, which do not show significant changes in dipole moment, are hardly affected by adding solvent effects. It should be kept in mind that thermal motion of the complexes and the solvent molecules around these will continuously break the highly symmetric average structure [188]. Hence, solvent effects are important, although one has to find a way to efficiently take into account the effect of the thermal motion in the calculation of the spectrum [189].

Finally, an analysis of the wave function was carried out using orthogonal Valence Bond theory. Two conclusions were obtained with this analysis: (i) the wave function of the ground state does not suffer changes when the solvent effects are included, and (ii) the weight of the ligand-to-metal charge transfer (LMCT) determinants is an indication of a possible thermal SCO. When the LS wave function has a contribution of approximately 45% of the LMCT, the complex is expected to undergo thermal SCO.

3.5 Post-publication: Accurate Shifted Spectra

The good results obtained with the B3LYP* functional (see *Section: Exchange-Correlation Functionals* in Chapter 2) in the treatment of the excited states of the Fe(III) complexes discussed in the next chapter and the systems described in Ref. [62] made us come back to the $[\mathrm{Fe(phen)_3}]^{2+}$ complex after the publication of the results reported in this chapter. Moreover, the increase of the computational power allowed us to redo the TD-DFT/PBE0 calculations with many more roots.

Figure 3.4 shows the B3LYP* spectrum (solid red line) taking into account the first 200 singlet roots, comparing it to the experimental results (green) and the CASPT2 spectrum (blue). The procedure to convert the calculated excitation energies in a graphical representation of the spectrum is the same as used in the work described before in this chapter, except that we express the energy differences in eV and the width of the gaussians is 0.25 eV. The spectrum has an intense peak centered at 5.10 eV (250 nm) corresponding to ligand-centered transitions and three less strong features between 2.50 and 3.50 eV (500-350 nm) arising from MLCT transitions. The representation of the energies in eV's makes clear that the TD-DFT/B3LYP* spectrum is fully consistent with the experimental one except for a constant shift of 0.35 eV. If we apply this uniform shift to the excitation energies, the dashed red curve is obtained, which shows a very good agreement with the experimental curve.

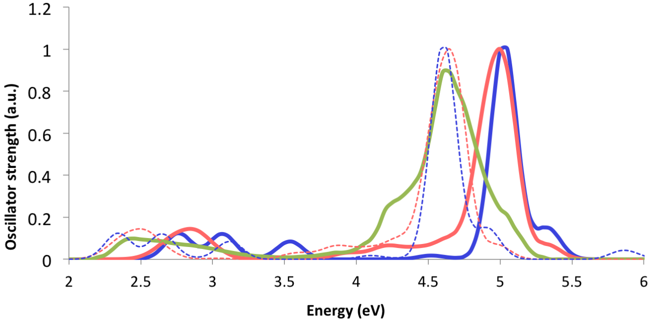

Figure 3.4: TD-DFT/B3LYP* absorption spectrum of $[\mathrm{Fe(phen)_3}]^{2+}$ (**1**) in vacuum represented by the solid red line, the CASPT2 in vacuum is represented by the solid blue line, and the solid green line represents the absorption spectrum obtained experimentally. The dashed lines are the shifted spectra.

Similarly, we can apply a slightly larger shift of 0.45 eV on the CASPT2 energies to obtain the red dashed curve, also coinciding with the experimental measurements over the whole interval. The mismatch between the on-set of the experimental MLCT band and the lowest CASPT2 energy for this state has been attributed to the effect of the thermal motion, inducing symmetry breaking and consequently localization of the electron on one ligand [190]. In the next chapter we will give evidence that this may also explain (at least partially) the error in the TD-DFT/B3LYP* energies.

To come back to the TD-DFT/PBE0 results reported in Fig. 3.5, we have repeated the calculation with 200 roots instead of the 40 used previously. Going to higher roots revealed that important excitations were missing in the smaller calculation, more specifi-

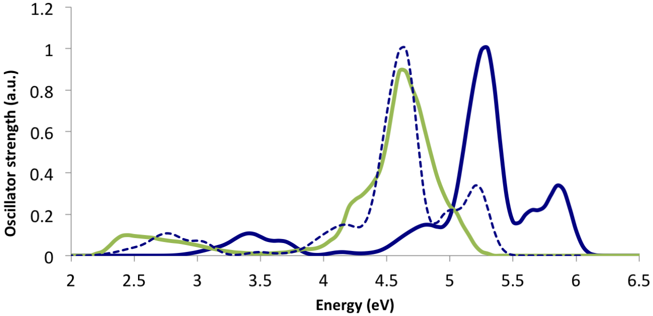

Figure 3.5: TD-DFT/PBE0 absorption spectrum of $[Fe(phen)_3]^{2+}$ (**1**) in vacuum represented by the solid blue line, the dashed blue line is the TD-DFT/PBE0 shifted spectrum (by 0.70 eV) and the solid green line represents the absorption spectrum obtained experimentally.

cally, we completely missed a very intense peak formed by ligand-centered transitions. The new spectrum (represented on an eV scale) is shown in Fig. 3.5. It becomes immediately clear that TDDFT/PBE0 also reproduces rather correctly the main features of the experimental spectrum, albeit that a larger shift (0.70 eV) has to be applied to obtain good agreement.

CHAPTER 4

TD-DFT Study of the Light-induced Spin-crossover of Fe(III) Complexes

4.1 Introduction

Over the last decades there has been considerable interest in spin-crossover (SCO) and the associated molecular bistability of first-row transition metal (TM) complexes. The most widely studied complexes are based on the prototypical Fe(II)N_6 core, but other ions and coordination spheres are becoming more and more important in the field [2, 4, 191]. In fact, the first description of SCO concerned an Fe(III) complex [39], and nowadays many more Fe(III) complexes have been reported [53, 192]. The so-called light-induced excited spin state trapping (LIESST), which triggers the spin transformation from a low spin state (LS) to a metastable high spin state (HS) by light, has received special attention both in experimental and computational studies because it offers an optimal control on the SCO process. LIESST was discovered in the 1980s [57, 58] and explained shortly afterwards [30, 154]. Some necessary ingredients for LIESST are a not too large energy difference between the LS and HS states; significant different geometry of the two spin states and a correct ordering of the metal-to-ligand charge transfer (MLCT) and ligand-field states [155–157]. The less frequent occurrence of LIESST in Fe(III) complexes has always been ascribed to the relatively small modification of the iron coordination sphere when the electronic configuration changes from LS to HS. However, other factors such as π-π intermolecular interactions between the ligands [193–198] have made possible the observation of SCO induced by light at reasonably high temperature and slow HS-LS relaxation in Fe(III) complexes.

Among the different Fe(II) complexes that show the LIESST phenomenon, $[\mathrm{Fe(bpy)_3}]^{2+}$ (bpy = 2,2'-bipyridine) is one of the most intensely studied ones. Most experiments have been done at room temperature in aqueous solution [15, 16, 19, 199–201]. After the initial laser pulse an excited singlet state with MLCT character is populated. This ^{1}MLCT state was shown to deactivate on an extremely short time scale into the HS state. The system needs not more than $\sim$130 fs to reach a vibrationally hot quintet state. This HS state relaxes back to the initial LS state at a much longer time scale; the lifetime of the HS state is 650 ps. Although there is a clear consensus about the main characteristics of the photocycle, the role of the triplet ligand field (Fe-3d^6) states is still under debate. The first intersystem crossing from singlet to triplet takes place in the MLCT manifold but it is not clear whether this state directly couples with the final HS state or that the deactivation goes via the triplet ligand field states. Arguments have been given for both scenarios [19, 61, 201, 202] and it is obvious that more research is needed to clarify this issue.

The LIESST mechanism in Fe(III) complexes is much less profoundly analyzed. Experimental studies have not gone much further than the observation that the HS state gets populated after irradiation through magnetic susceptibility measurements [194–198, 203], but no time-resolved experiments have been published. From the theoretical point of view, we can mention the calculations by Ando and co-workers [204], who optimized the geometries of the different spin states of $[\mathrm{Fe(pap)_2}]^+$ (Hpap = N-2-pyridylmethylidene-2-hydroxyphenylaminato), and calculated the vertical excitation en-

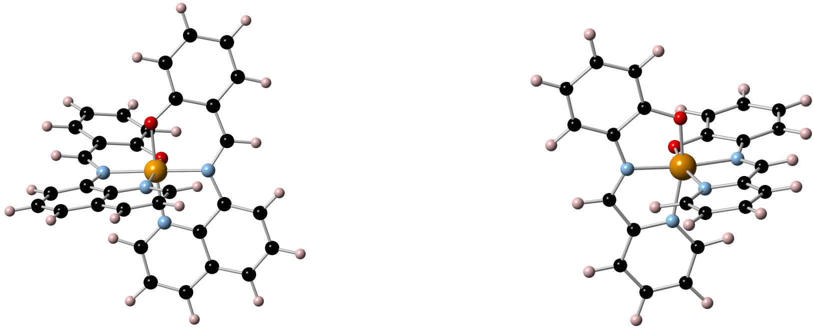

Figure 4.1: Ball and stick representation of the Fe(III) complexes: $[Fe(qsal)_2]^+$ (left), $[Fe(pap)_2]^+$ (right). Color code: orange for Fe, red for O, black for C, blue for N and pink for H.

ergies and some aspects of the HS to LS deactivation. The present study makes a first step towards the detailed theoretical description of the LIESST process in Fe(III) complexes. From an accurate description of the fundamental LS state, we construct an approximate minimal energy path to the optimal geometry of the HS state and follow the energies of a large collection of excited states along this path to locate regions where intersystem crossing can take place and to explore the character of possible intermediate states in the LIESST process. Furthermore, we provide a rough estimate of the deactivation time by the calculation of the intersystem crossing rates with the time-dependent formulation of Fermi's golden rule [205]. The main focus is on $[Fe(qsal)_2]^+$ (Hqsal = N-(8-quinolyl)salicylaldimine), but we also pay attention to the $[Fe(pap)_2]^+$ complex. Both complexes are schematically depicted in Fig. 4.1.

4.2 Computational Information

Despite the tremendous effort that has been made in the search of a density functional that is able to correctly reproduce the relative stability of high spin and low spin electronic configurations, there seems to be no consensus about the best strategy to accurately predict the adiabatic energy difference between HS and LS states in spin crossover complexes. Nevertheless, there are several functionals that have been tested for a large set of complexes and that turn out to work rather satisfactorily, examples are OPBE, TPSSh and B3LYP* [83, 184, 206]. The latter functional reduces to 15% the exact Fock exchange in the standard B3LYP functional. This reduction is based on the observation that ΔE_{HL} depends linearly on the amount of Fock exchange in the functional. Whereas the original B3LYP systematically overestimates the stability of the HS state, reducing the Fock exchange to 15% brings the calculated relative stability in agreement with experiment for a large collection of SCO complexes. For an accurate computational description of light-induced SCO it is also important to have good geometries and accurate estimates of the vertical excitation energies. These two aspects have been tested by Papai and co-workers for three Fe(II) complexes [62] and it was concluded that the B3LYP* functional leads to geometries as accurate as obtained with virtually any other choice, but more importantly also reproduces rather well the potential energy curves of ground and excited states using the time-dependent variant of DFT. This let us to decide to use this functional to explore the LIESST mechanism in the two Fe(III) complexes mentioned before. To establish the performance of the functional with respect to the calculated geometries and vibrational frequencies, we compare the results to those obtained with the PBE0 functional (more details in Section S3 of *Chapter4: Sup. Info.* of ioChem-bd, DOI:10.19061/iochem-bd-2-3), which was previously used in the study of the deactivation mechanism in $[Fe(bpy)_3]^{2+}$ [60]. The adiabatic energy differences and vertical excitation energies are compared to experimental data when available and to results of multiconfiguration wave function calculations, specifically complete active space self-consistent field (CASSCF) followed by CAS second-order perturbation theory (CASPT2).

All B3LYP* calculations have been performed with the ORCA program package version 3 [207]. Both for the geometry optimizations and the TD-DFT calculations, the def2-TZVP [161] basis set (triple zeta for the valence plus polarization functions on all atoms) was used. To reduce the computational cost implicit to the use of hybrid functionals, we have activated the RIJCOSX procedure [208] to speed-up the calculation of the exchange contribution to the energy. Vibrational frequencies were calculated by numerical differentiation of the analytical gradients for the lowest states of each spin symmetry (doublet, quartet and sextet) and fully numerically for the first lowest excited doublet state of ligand-to-metal charge transfer character (LMCT)[209]. In the latter case, we have reduced the basis set to split-valence quality (def2-SV(P) [161]) and increased the convergence criteria to avoid spurious imaginary frequencies. The effect of the basis set reduction on the vibrational frequencies was tested by repeating some of the calculations for the fundamental states with this smaller basis. The calculations with the PBE0 functional (the hybrid variant of the PBE functional with 25% Fock exchange) [136] were performed with TurboMole 6.6 [165, 210–212] using the same def2-TZVP basis set as before.

In addition to the full geometry optimization, we also generated a two-dimensional potential energy surface by performing a series of restricted geometry optimizations in which the Fe-O and Fe-N distances were kept fixed while the rest of the complex was fully relaxed. The Fe-O distance was fixed at different values in the interval of 1.80 to 2.00 Å and the Fe-N distance was varied in the 1.85–2.30 Å interval. This surface contains the HS and LS minimal structures and allows us to define an approximate minimal energy path to interpolate between the two minima. The evolution of the excited state energies was followed along this interpolation path to find the approximate location of intersystem crossings from the excited doublet state to quartet and sextet states and in this way obtain information about the character of the intermediates in the LIESST process.

CASSCF/CASPT2 calculations were performed as implemented in the MOLCAS 7.4 package [167]. Atomic natural orbital (ANO) basis sets optimized for scalar relativistic effects and core correlation were applied for all atoms [168, 169]. For both complexes we used a (7s,6p,5d,4f,3g,2h) contraction for Fe, (4s,3p,1d) for N and O, (3s,2p) for C and (2s) for H. The Cholesky decomposition [170, 171] was used to reduce the computational cost associated to the calculation of the two-electron integrals. Scalar relativistic effects were included using Douglas-Kross-Hess Hamiltonian

[172]. Spin-orbit coupling (SOC) and oscillator strengths of the electronic transitions were calculated with the state interaction approach [173, 174, 213].

Two active spaces were used to construct the CASSCF reference wave function depending on the studied transitions. The first active space contains 9 electrons distributed in all possible ways over 12 orbitals; five orbitals with mainly Fe-3d character, two σ-bonding orbitals with important contributions on the lone pairs of N and O, and five orbitals that account for the double-shell effect of the 3d-shell, the so-called 3d' orbitals. This active space has been used in many applications on TM complexes before and provides a balanced description of all the important non-dynamic electron correlation [89, 174, 175]. It has been used to build the two-dimensional CASPT2 potential energy surface of the LS and HS states. The second active space extends the previous one with two ligand π orbitals leading to an active space of 14 orbitals and 13 electrons. The inclusion of these orbitals permits us to study the electronic excited state with LMCT character, which turned out to be the lowest optically allowed transitions in contrast to the $[\mathrm{Fe(bpy)_3}]^{2+}$ complex where the lowest excited states have metal-to-ligand charge transfer character. More information about the shape of the active orbitals can be found in the Sections S1 and S4 of *Chapter4: Sup. Info.* of ioChem-bd(DOI:10.19061/iochem-bd-2-3).

CASPT2 calculations account for the remaining electron correlation by correlating all the electrons except the deep core electrons ($1s^2$ for N, O and C and $1s^2 2s^2 2p^6$ for Fe). In order to exclude possible intruder states, we applied an imaginary level shift of 0.15 a.u. in CASPT2 [147]. The standard definition of the zeroth-order Hamiltonian (IPEA=0.25 a.u.) was used. Moreover, three more IPEA values, 0.00, 0.50 and 0.70 a.u., have been tested to check the influence of this parameter on the adiabatic CASPT2 energies [214].

4.3 Results and Discussion

Geometry, Vibrational Frequencies and Energetics

The geometries were fully optimized for the lowest spin-states of the $3d^5$ configuration of the Fe^{3+}: the doublet and the sextet. The DFT calculations for the doublet and sextet were performed within the spin-unrestricted formalism, and hence, the resulting electronic states are not necessarily eigenfunctions of the $\hat{S}^2$ operator. However the spin functions considered here are essentially mono-determinantal and the spin contamination is very small. The predicted values of $\hat{S}^2$ for HS and LS, 8.76 and 0.77, are close to the expected values of 8.75 and 0.75.

Table 4.1 shows the optimized bond lengths of the central Fe(III) ion to the six atoms in the first coordination sphere of the two complexes. The structures are slightly distorted from the ideal octahedral coordination with shorter Fe-O bonds than the Fe-N ones, which in turn appear in pairs. The distances are in good agreement with experiment, albeit slightly overestimated. The largest deviation is observed for the Fe-N bond length in the HS state of $[Fe(qsal)_2]^+$, which is 0.09 Å longer than the experimental value. All other distances differ by less than 0.05 Å. The expansion of the coordination sphere is nicely reproduced by the DFT calculations; the Fe-O distance is hardly affected by the change in the spin state, while the Fe-N distances change by approximately 0.2 Å. The DFT calculations also reproduce the angles in the Fe coordination sphere rather accurately, Tables S2.1 and S5.1 (see *Chapter4: Sup. Info* of the ioChem-bd, DOI:10.19061/iochem-bd-2-3) show that none of the calculated angles differs by more than 5° from the experimental value, both in the LS and the HS geometries.

The expansion of the Fe coordination sphere (see Δr in Table 4.1) in the prototypical Fe(II)N_6 SCO materials is known to strongly affect the frequencies of the vibrational modes dominated by the stretching of the Fe–N bonds. In general, these modes get softer by about 50-120 cm^{-1} in the HS state, which gives a major contribution to the increased entropy of the HS state [215]. A similar change in the vibrational modes is also observed in the DFT calculations on the two Fe(III) complexes studied here. Table 4.2 shows a selection of HS and LS vibrational frequencies, which imply important displacements in the FeN_4O_2 core of the complex. The vibrations are marked as bending or stretching and in the latter case we also put a symmetry label on the vibrations. This is, however, to some extent arbitrary since the complex exhibits an approximate octahedral symmetry and the vibrations turn out to be mixtures of

Table 4.1: B3LYP*/def2-TZVP optimized bond lengths in Å of $[Fe(qsal)_2]^+$ and $[Fe(pap)_2]^+$. Δr measures the bonds expansion upon LS-HS transition. The experimental distances in parenthesis are taken from Ref. [195].

$[Fe(qsal)_2]^+$ distance	HS	LS	Δr
Fe–O	1.91 (1.88)	1.88 (1.88)	0.03 (0.00)
Fe–N_1	2.21 (2.12)	2.02 (1.97)	0.19 (0.15)
Fe–N_2	2.18 (2.09)	1.97 (1.94)	0.21 (0.25)
$[Fe(pap)_2]^+$ distance	**HS**	**LS**	**Δr**
Fe–O	1.93 (1.93)	1.88 (1.88)	0.05 (0.05)
Fe–N_1	2.25 (2.21)	2.01 (1.99)	0.24 (0.22)
Fe–N_2	2.18 (2.17)	1.93 (1.91)	0.25 (0.26)

bending and stretching modes, with contributions not only of the FeN_4O_2 core, but also coupled to movement on the ligands. For this reason, it has not been possible to assign the symmetric breathing mode in the HS state of $[Fe(pap)_2]^+$.

The stretching modes labeled t_{1u} are characterized by an off-center movement of the Fe ion and it is exactly in these modes that the largest difference between the LS and HS state is observed. The t_{1u} frequencies are lowered by 115 and 95 cm^{-1} on average in $[Fe(qsal)_2]^+$ and $[Fe(pap)_2]^+$, respectively. The frequencies of the other vibrations are also lowered but the change is in general significantly smaller.

To close this exploration of the ground state properties, we report the adiabatic energy difference of the LS and HS state ΔE_{HL}. This key parameter is notoriously difficult to calculate with DFT methods given the strong dependency of the results on the functional applied, but even for multiconfigurational wave function based calculations there is some debate on the most reliable (efficient) procedure to calculate this property. As stated in the Introduction, the B3LYP* functional was specifically designed to reproduce ΔE_{HL} in Fe(II) complexes. Our present results show that the functional also performs rather well for the here considered Fe(III) complexes. In both cases, the LS electronic energy is lower than the HS energy, in agreement with the LS character of both complexes at room temperature and below (contrary to the PBE0 results, see Table S3.3 of *Chapter4: Sup. Info* in ioChem-bd, DOI:10.19061/iochem-bd-2-3). A direct validation of the size of the calculated ΔE_{HL} is

Table 4.2: Frequencies (in cm^{-1}) of the Fe-L bending and stretching modes for the LS and HS states of $[Fe(qsal)_2]^+$ and $[Fe(pap)_2]^+$. The labels of the stretching modes are approximate due to the non-ideal octahedral symmetry.

	$[Fe(qsal)_2]^+$		$[Fe(pap)_2]^+$	
Character	LS	HS	LS	HS
Bending				
	164	133	168	95
	184	141	179	152
	200	185	209	175
	224	193	261	235
	233	210	280	246
Stretching				
e_g	218	222	241	227
e_g	256	239	250	231
a_g	259	226	252	–(a)
t_{1u}	342	260	333	271
t_{1u}	353	261	336	272
t_{1u}	385	308	441	281

(a) The symmetric stretch (or breathing mode) could not be identified.

difficult, since this parameter is not easily extracted from experiment. Hence, we opt for an indirect comparison with experiment via the transition temperature of the thermal spin crossover $T_{1/2}$ [193, 195, 216]. Following the procedure outlined in previous studies [84, 215, 217–220], we calculated $T_{1/2}$ by adding the zero-point energy to the electronic energy of both states and look for the temperature at which the $T\Delta S$ product is equal to the enthalpy. The entropy change is dominated by the vibrational contribution but has a small constant contribution due to the different spin multiplicity of the LS and HS states of $9.13\ \mathrm{J/K^{-1}\ mol^{-1}}$ ($0.76\ \mathrm{cm}^{-1}/K$). Table 4.3 lists the DFT adiabatic HS–LS energy differences, the zero-point energy contribution and the sum of these two terms (ΔH_{HL}) for the two complexes. The resulting $T_{1/2}$ are in qualitative agreement with the experimental values of the transition temperatures, which adds additional evidence for the reliability of the B3LYP* functional for determining the relative energies of the electronic states involved in the SCO process in Fe(III) complexes. The overestimation of the transition temperature is most probably a combination of uncertainty in the calculated ΔE_{HL} and the lack of environment effects, which play an important role due to the π-π interactions between the ligands on neighboring complexes. Note that these interactions also cause the hysteresis and the two-step nature of the thermal spin crossover. The theoretical description of these phenomena goes beyond the scope of the present study. Here, the focus is on the light-induced variant, and more specifically on the initial stages of the process to obtain information about the deactivation mechanism from excited LS state to metastable HS state. This process is much less dependent on the environment and

Table 4.3: DFT/B3LYP* adiabatic HS-LS energy difference (ΔE_{HL}), difference in zero-point energy (ΔZPE) and theoretical estimate of the transition temperature for thermal spin crossover of $[\mathrm{Fe(qsal)_2}]^+$ and $[\mathrm{Fe(pap)_2}]^+$. Energies in cm^{-1}, temperature in K. Experimental data in parenthesis [193, 195, 216].

	$[\mathrm{Fe(qsal)_2}]^+$	$[\mathrm{Fe(pap)_2}]^+$
ΔE_{HL} (DFT)	2166	2127
ΔZPE	-670	-660
ΔH_{HL}	1496	1467
$T_{1/2}$	350 (289-205)	324 (181-165)

can be studied in isolated complexes.

Potential Energy Surfaces for LS and HS

The largest changes in the geometry between the doublet and sextet states take place in the first coordination sphere of the Fe(III) ion and lead to an increase of the radius of the coordination sphere by approximately 0.15 Å. This expansion largely determines the potential energy surface on which the SCO takes place, but other more subtle geometric changes also play a role in facilitating the thermal SCO or the deactivation of the excited LS state in LIESST [221, 222]. By performing a series of restricted geometry optimizations, a two-dimensional potential energy surface was constructed as explained in the computational information. Figure 4.2 shows the B3LYP* energies on this grid for the spin state with the lowest energy (*i.e.*, the doublet) state for the smaller distances and the sextet state for the part of the surface with larger Fe-O and Fe-N distances. The surface was constructed with 400 points and the contours in the figure are interpolations, which should be considered as a guide to the eye. For both complexes, the line that connects the two minima can be considered within a rather good approximation as the minimal energy path and we will use it as reaction coordinate to follow the deactivation of the excited LS state towards the meta-stable HS state.

This reaction coordinate not only involves the expansion of the coordination sphere but also includes all other geometric changes between the LS and HS state, among which the opening of the O-Fe-N angle is one of the most important ones (see Tables S2.1 and S5.1 of *Chapter4: Sup. Info* in ioChem-bd, DOI:10.19061/iochem-bd-2-3). Therefore, the representation of the potential energy surface in terms of the Fe-N and Fe-O distances is just one of the many possible. Alternatively one could also choose the Fe-N distance and the O-Fe-N angle as coordinates to explore the ground state energy surface as is done in Fig. 4.3 for $[Fe(qsal)_2]^+$. The approximate minimal energy path from LS to HS in this representation is also nearly linear although a certain decoupling of the enlargement of the Fe-N distance and the opening of the O-Fe-N distance can be observed on the potential energy surface. This two-mode model has also been invoked in the SCO mechanism in Fe(II) complexes both for the thermal [30, 62] and the light-induced variant [18, 22]. The two-mode deactivation mechanism requires an extensive exploration of the excited state potential energy surfaces, which will be subject of a follow-up study.

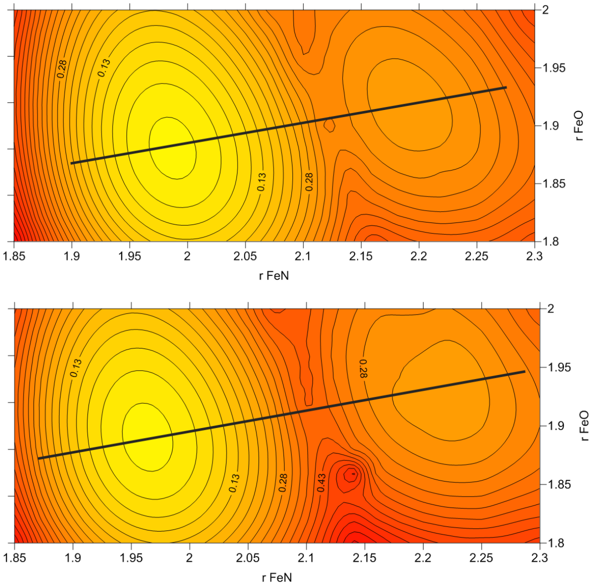

Figure 4.2: B3LYP* potential energy surface as function of the Fe-N and Fe-O distances (Å) of the lowest electronic state of $[Fe(qsal)_2]^+$(top) and $[Fe(pap)_2]^+$(bottom). The black thick line indicates the quasi minimal energy path (MEP) connecting the LS minimum on the left to the HS minimum on the right. Energies (in eV) are relative to the total energy of the LS minimum.

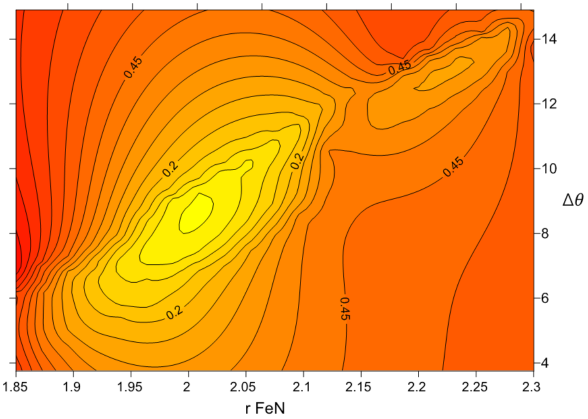

Figure 4.3: B3LYP* potential energy surface of the lowest electronic state of $[\mathrm{Fe(qsal)_2}]^+$ as function of the Fe-N distance (Å) and $\Delta\theta$ (degrees), the difference in the O-Fe-N angle between LS and HS.

CASPT2 calculations can give accurate excitation energies provided that the active space and basis set are properly chosen. Additionally, it has been shown in previous works on Fe(II) complexes that it is essential to re-optimize the distances between Fe and its first neighbours [60, 175, 223]. The use of DFT optimized geometries can easily lead to errors larger than 1 eV. This is caused by the fact that CASPT2 has the tendency to shorten the Fe-L distances, which leads to stronger ligand field and consequently higher MC excited states. The effect on the LMCT (and MLCT) states is less drastic since the electronic configuration of these states does normally not contain electrons in the anti-bonding Fe-3d(e_g) orbitals as it is also the case for the LS ground state. A full geometry optimization of the whole complex with CASPT2 is beyond the current computational possibilities and therefore we opt for single point CASPT2 calculations on a selection of points generated with the restricted DFT geometry optimizations to find the optimal Fe-N and Fe-O distances for [Fe(qsal)$_2$]$^+$. There is ample evidence that the CAS(9,12) and the basis set specified in the computational information are sufficiently large to give close to converged estimates of the optimal CASPT2 distances [175, 185, 186, 214, 220].

The CASPT2 potential energy surface shown in Fig. 4.4 is less well defined than the ones that were constructed from the DFT data due to the smaller number of points, but the graph shows that the energy surface has the same shape as the DFT/B3LYP* one, with the difference that the minima for both LS and HS state appear at smaller Fe-ligand distances. The minimum of the LS state is located at 1.93 Å and 1.82 Å for the Fe-N and Fe-O distances, respectively. These distances increase by 0.19 Å for the Fe-N and 0.04 Å for the Fe-O distance in the HS minima, being the Δr_{HL} very similar to the experimental increase. For the [Fe(pap)$_2$]$^+$ complex, we located the minimum of the LS state at 1.89 Å and 1.84 Å for the Fe-N and Fe-O distances, respectively. The variation of the Fe-N distance in the HS minima is 0.04 Å larger than the complex [Fe(qsal)$_2$]$^+$ and it is equal for the Fe-O distance, locating this minima at 2.12 Å and 1.88 Å respectively.

The CASPT2 adiabatic HS-LS energy differences at the geometries with the relaxed Fe-O and Fe-N distances are 1658 and 2157 cm^{-1}, respectively, as shown in the last entry of Table 4.4. This is in a good agreement with the B3LYP* adiabatic energy difference listed in Table 4.3. To complete the comparison between CASPT2 and DFT, we looked at the proposal of Kepenekian *et al.* [214] to calculate ΔE_{HL}. They observed that the CASPT2 ΔE_{HL} values calculated with the standard zeroth-order Hamiltonian $\hat{H}^{(0)}$ are systematically underestimated for Fe(II) complexes and found that increasing the IPEA values greatly improves the theoretical estimate of this quantity. This was later confirmed by Lawson Daku and co-workers [224]. However, in the present case the recipe of increasing the IPEA value does not give the desired result. The effect is similar to what is observed in the Fe(II) complexes –increasing the IPEA favors the LS state with respect to the HS state– but the calculated ΔE_{HL} becomes so large that thermal spin crossover near room temperature is no longer viable. For example, using the values obtained with IPEA=0.50 a.u., the theoretical estimate of $T_{1/2}$ becomes larger than 700 K, which is clearly outside the experimental range. On the other hand, it can be seen from the Table 4.4 that the definition of the zeroth-order Hamiltonian in the original CASPT2 papers from the early 1990s (*i.e.*, IPEA=0.00 a.u.) fails to predict the LS as ground state [89, 144].

Absorption Spectra

To study the deactivation mechanism from the initially populated excited LS state to the metastable HS state we cannot stay on the ground state energy surfaces, and therefore, we will now switch attention to the excited states. The most two common low-lying excitations for Fe(III) complexes are: (i) the metal centered (MC)

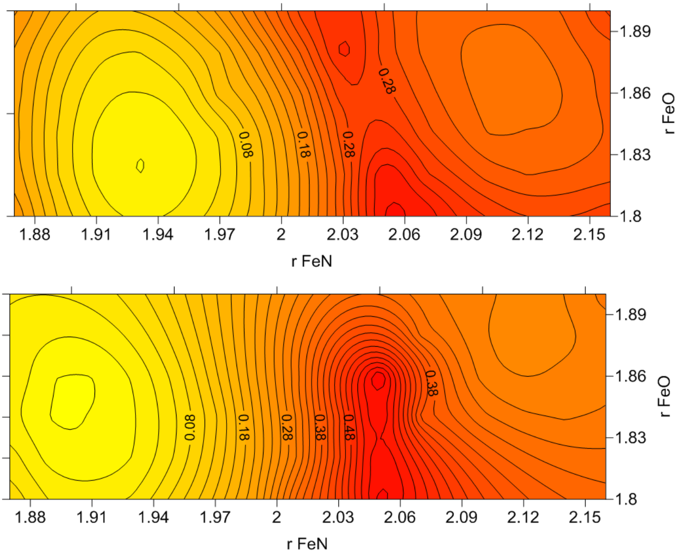

Figure 4.4: CASPT2 potential energy surface as function of the Fe-N and Fe-O distances (Å) of the lowest electronic state in the complexes $[\mathrm{Fe(qsal)_2}]^+$ (top) and $[\mathrm{Fe(pap)_2}]^+$ (bottom). Energies (in eV) are relative to the total energy of the LS minimum.

Table 4.4: CASPT2 ΔE_{HL} values (in cm^{-1}) calculated with different IPEA values (in a.u.) in the definition of $\hat{H}^{(0)}$ using the B3LYP* optimized geometry or the geometry with CASPT2 reoptimized Fe–ligand distances.

Geometry	IPEA	ΔE_{HL}	
		$[Fe(qsal)_2]^+$	$[Fe(pap)_2]^+$
B3LYP*	0.00	-628	-53
	0.25	2050	2742
	0.50	3877	4548
	0.70	5133	5780
+ reopt. d(Fe–L) $^{(a)}$	0.25	1658	2157

(a) Fe–ligand distances are reoptimized with CASPT2

transitions involving electron replacements within the Fe-3d orbitals, and (ii) the ligand-to-metal charge transfer (LMCT) transitions transferring one electron from the π system of the ligand to the iron center, as illustrated in Fig. 4.5. The higher formal oxidation state of Fe makes that the metal-to-ligand charge transfer (MLCT), dominant at low energies in the more commonly studied Fe(II) complexes, lies at higher energies and therefore less important for the spin crossover. The π-π^* excitations on the ligands also lie at higher energy than the LMCT transitions.

Figure 4.6 displays the B3LYP* absorption spectrum of $[Fe(qsal)_2]^+$ (*top*) and $[Fe(pap)_2]^+$ (*bottom*) in their LS ground state. The curves are obtained by representing each transition by a gaussian function with a full-width at half-maximum of 40 nm and a height that corresponds to the relative oscillator strength.

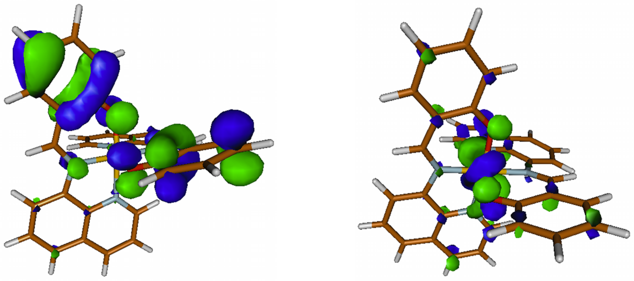

Figure 4.5: Graphical representation of the orbitals involved in LMCT transition of $[\mathrm{Fe(qsal)_2}]^+$; *left*: the ligand π orbital that looses one electron, *right*: the Fe-3d orbital of t_{2g}-like character that receives the electron.

Starting with $[\mathrm{Fe(qsal)_2}]^+$, the main peak at 724 nm is dominated by LMCT transitions and is in good agreement with the experimental wave length of 803 nm used to induce the SCO. At lower energy, one can find the MC transitions, but these have much lower oscillator strengths and do not contribute to the absorption spectrum. At higher energy, between 615-470 nm, we observe other intense bands, which can be ascribed to ligand-ligand excitations. Unfortunately, we are not aware of any experimental absorption spectrum in the literature of this complex and therefore a direct comparison with experiment is not possible. However, a similar broad band around 724 nm has been reported in the literature for other Fe(III) complexes with spin crossover, for example $\mathrm{Fe(acpa)_2}$ and $\mathrm{Fe(Sal_2tr)}$ [225, 226]. In these two complexes the LMCT is found at slightly higher energy, 685 and 620 nm respectively. The absorption spectrum of $[\mathrm{Fe(pap)_2}]^+$ has the same overall shape.

The most significant difference is the shift to lower energies of the main LMCT band to 820 nm and the increased LMCT character of the band between 500-550 nm. This is in agreement with experiment, since LIESST is triggered with 532 nm light in this compound.

We also compared the vertical excitation energies obtained with B3LYP* to those calculated with CASPT2. For this purpose the active space was extended with two occupied ligand π-orbitals resulting in a CAS(13,14). Using the geometry with the re-optimized Fe–ligand distances, the lowest LMCT state appears at 578 nm in complex $[\mathrm{Fe(qsal)_2}]^+$ and at 354 nm for $[\mathrm{Fe(pap)_2}]^+$. Both transition energies are significantly higher than those found in the TD-DFT calculations and used in the LIESST experiments. A possible explanation lies in the symmetry of the complexes. The two-fold rotation axes forces the ligand-π orbital involved in the LMCT process to be delocalized over both ligands. As found by Domingo *et al.* [227], the inclusion of the effect of the thermal motion leads to a constant symmetry breaking and consequently two inequivalent ligands. The localization of the orbital involved in the CT excitation on one of the ligands was shown to lower the excitation energy significantly. To avoid lengthy molecular dynamics simulations and subsequent CASPT2 calculations on a series of snapshots as done in Ref. [227], we distort the geometry of the complex by hand shortening the Fe-ligand distance by 0.2 Å for one of the ligands. Figure 4.7 shows how this distortion leads to a localization of the ligand π orbital and induces a lowering of the excitation energy in complex $[\mathrm{Fe(qsal)_2}]^+$ to 775 nm, in much better agreement

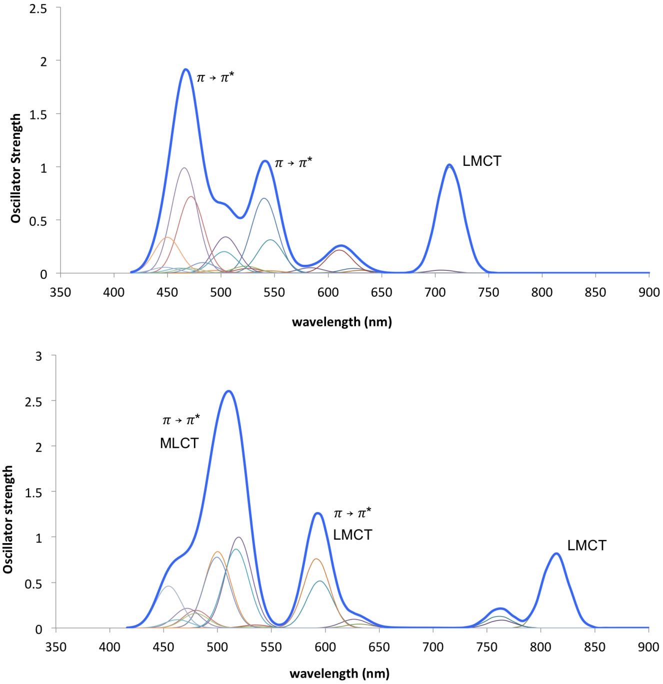

Figure 4.6: B3LYP* absorption spectrum of $[Fe(qsal)_2]^+$ (top) and $[Fe(pap)_2]^+$ (bottom). The individual transitions (thin lines) are represented by a Gaussian function (bw = 40 nm). Oscillator strength in arbitrary units.

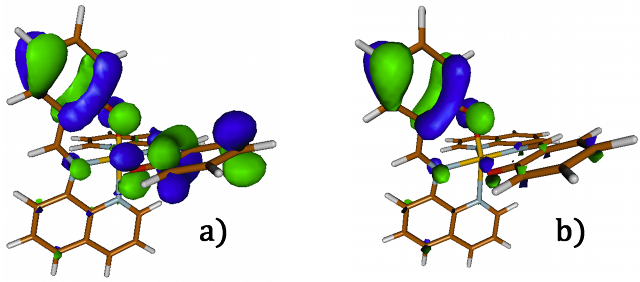

Figure 4.7: Graphical representation of the ligand π orbital involved in the LMCT transition of the $[Fe(qsal)_2]^+$ complex. a) Delocalized orbital over two ligands with non-distorted geometry. b) Localized orbital over one ligand with distorted geometry.

with the experimental value. Doing the same trick in the TD-DFT calculation lowers the LMCT energy to 820 nm, still in excellent agreement with CASPT2 and experiment.

Excited States Along the Quasi-MEP

In analogy to the study of the LIESST phenomenon in Fe(II) complexes [60, 61, 185, 186], we constructed the potential energy curves of the ground and excited states along the approximate minimal energy path that connects the LS and HS minima shown in Fig. 4.2 as a thick black line. At regular intervals on this line, TD-DFT calculations were performed to follow the evolution of the relative energies of a collection of excited states. The results are shown in Fig. 4.8. The two figures share the same main characteristics.

At short Fe–L distances, both complexes exhibit a doublet ground state dominated by the Fe-3d^5 configuration shown in the upper left panel of Fig. 4.9. The other two components of this electronic configuration –degenerate with the ground state in a perfect octahedral surrounding– lie approximately 0.6 eV higher in energy. This relative energy between the different components of the LS term (^{2}T$_{2g}$ in O_h symmetry) was also obtained with CASPT2. At larger distances, the ground state corresponds to the HS state (^{6}A$_{1g}$ in O_h symmetry) with an electronic configuration shown in the upper right panel of Fig. 4.9. This state rapidly increases in energy with decreasing distance and lies way up in energy in the Franck-Condon region of the doublet ground state. At lower energy, we can observe a quartet state with a Fe-3d^5 configuration (upper-middle panel in Fig. 4.9). The fact that this state has only one electron in the antibonding e_g-like orbitals causes this state to have a minimum somewhere between the distances where the doublet and sextet have their lowest energy. Note that this intermediate spin (IS) state lies rather close in energy to the crossing point of the LS and HS state as earlier observed by Ando [204] in [Fe(pap)$_2$]$^+$ and by Iuchi [228] in the Fe(II) complex [Fe(bpy)$_3$]$^{2+}$. The other components of the lowest IS (^{4}T$_{1g}$ in O_h symmetry) lie slightly higher and can be recognized in the Fig. 4.8 as the two grey lines parallel to the thick green line at approximately 0.3 and 0.5 eV higher energy.

The other low-lying states are doublets of LMCT character, whose electronic configuration can be found in the left lower panel of Fig. 4.9. These states have the strongest oscillator strength and are populated when the system is irradiated with light. The potential energy curves of these states are parallel to the metal centered doublets since both have zero electrons in the Fe-3d e_g-like orbitals. The quartet LMCT states lie at significant higher energy and are not expected to play any role in the deactivation process from ^{2}LMCT to HS. This is quite different from the mechanism generally accepted for the Fe(II) complexes, where the first intersystem crossing takes place in the MLCT manifold. The quartet LMCT states lie higher in energy than the doublets LMCTs because unavoidably one of the Fe-3d e_g-like orbitals has to be occupied to form a quartet state (Fig. 4.9, *right*), which is not the case for the doublet LMCTs.

Deactivation Rates in Fe(III) Complexes

The shape of the potential energy curves suggests that the deactivation of the ^{2}LMCT state involves an intersystem crossing with the metal centered quartet state followed by an intersystem crossing with the final metastable HS state (see Figure 4.9). To give support for this deactivation path we estimate the intersystem crossing rates using the time-dependent formulation of Fermi's golden rule [205] and successfully applied to describe the photocycle in $[\mathrm{Fe(bpy)_3}]^{2+}$ [61]. Vibrational frequencies and normal modes were determined for the LS, IS, and HS states in an ordinary DFT treatment, while the ^{2}LMCT state was addressed with TD-DFT. Combined with the energy differences and the spin-orbit coupling among these four states, the crossing rates were determined, and

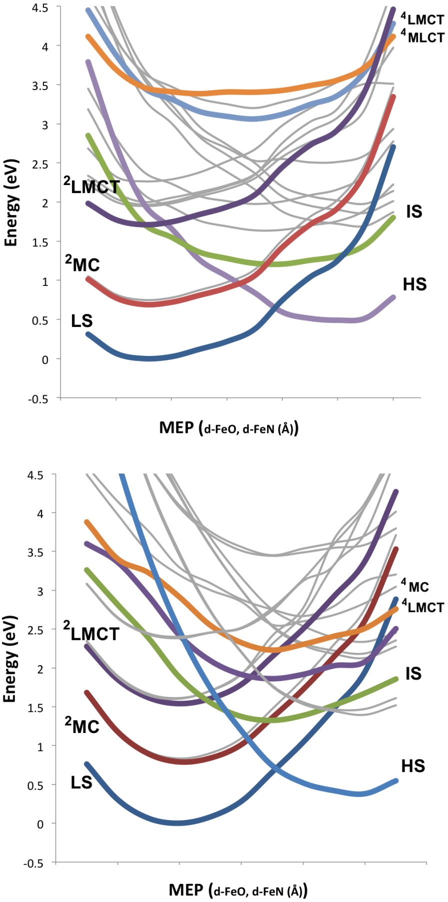

Figure 4.8: B3LYP* potential energy curves for a collection of electronic states along the quasi-MEP of the complexes $[Fe(qsal)_2]^+$ (top) and $[Fe(pap)_2]^+$ (bottom).

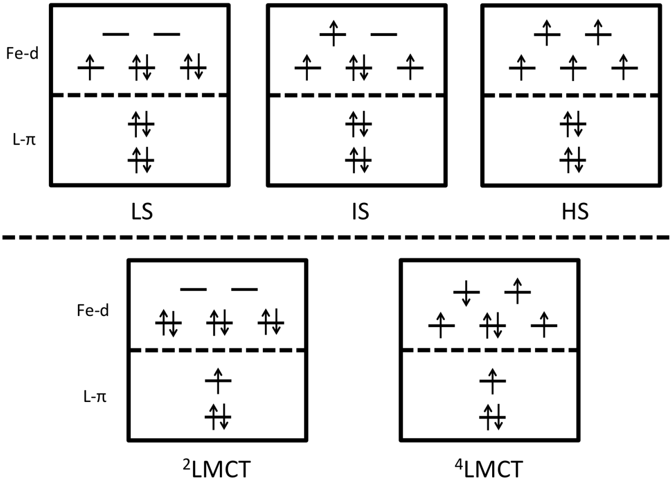

Figure 4.9: Schematic representation of the electronic configurations of the states involved in the LIESST phenomenon.

from these the lifetimes of the excited states. As stated in the computational information, the spin-orbit coupling among the different states was calculated through the state interaction using the CASSCF wave functions. The use of an effective one-electron spin-orbit operator [229] makes the direct coupling between states that differ by more than one electron in the leading electronic configuration very small (or even zero). Therefore, we also consider second-order effects, that is the coupling between Ψ_I and Ψ_J involving other intermediate states. Instead of using the perturbative expression applied by Iuchi in the study of the spin-orbit coupling in $[Fe(bpy)_3]^{2+}$ [228], we have included this indirect coupling in a variational manner with the effective Hamiltonian approach. The full spin-orbit matrix with 14 doublets, 15 quartets and 8 sextet states is mapped on a smaller model space that only contains the LS, IS, HS and ^{2}LMCT states. The matrix elements of the effective Hamiltonian shown in Table 4.5 include not only the direct spin-orbit coupling between the states of the model space, but also the effect of the indirect coupling via the external states [119].

Starting with the ^{2}LMCT state, there are several possible deactivation paths. The small spin-orbit coupling with the HS state (3.4 cm^{-1}) makes the direct deactivation of the excited state highly improbable. Alternatively, the ^{2}LMCT may undergo an internal conversion and fall back in the initial LS state. This will certainly happen, but we cannot calculate the rate of this process, since Fermi's golden rule only gives us access to intersystem crossing rates. To address the internal conversions one has to rely on more sophisticated simulation techniques like multiconfigurational time-

Table 4.5: Effective spin-orbit coupling matrix elements $\langle \Phi_I | \hat{H}_{SO}^{eff} | \Phi_F \rangle$ of the complex [Fe(qsal)$_2$]$^+$ at the B3LYP* optimized geometry of the LS state.

Φ_I	Φ_F	SO coupling (cm^{-1})
^{2}LMCT	IS	15.0
^{2}LMCT	HS	3.4
IS	HS	368.1
IS	LS	347.0
HS	LS	8.9

dependent Hartree (MCTDH) simulations or ab initio molecular dynamics with surface hopping [230–236]. Remains the intersystem crossing with the IS state. The rather small spin-orbit coupling (15 cm^{-1}) is solely due to second-order coupling, since the leading electronic configurations of the two states differ by more than one electron (see Fig. 4.9) making the direct coupling practically zero. However, this small coupling is partially compensated by a rather large vibrational contribution and we obtain a reasonably high intersystem crossing rate.

After reaching the IS state, the system can further evolve either by an intersystem crossing with the HS state (368.1 cm^{-1}) to complete the LIESST path, or fall back on the initial LS state (347.0 cm^{-1}). The calculated intersystem crossing rates show that both processes are extremely fast and compete. This means that the quantum yield of the LIESST process can never be as high as found in the polypyridyl Fe(II) complexes, where the quantum yield is reported to be unity. This is, however, not the case in the here-considered Fe(III) complexes. Experimental studies point at a much lower efficiency. Let us finally stress that the system reaches the HS state, it becomes trapped. The intersystem crossing rate with the LS state is small (8.9 cm^{-1}).

A graphical representation of the deactivation pathway that arises from our calculations is given in Fig. 4.10. It shows how the ^{2}LMCT undergoes a (slow) intersystem crossing with the IS state and thereafter the system either falls back on the LS state or undergoes a second intersystem crossing and gets trapped in the HS state, as expected for LIESST. Both process are fast and compete.

4.4 Conclusions

The strategy proposed by Papai *et al.* [62] to study to electronic structure and the thermodynamic properties of Fe(II) spin-crossover complexes has been validated for two prototypical Fe(III) complexes, $[\text{Fe(qsal)}_2]^+$ and $[\text{Fe(pap)}_2]^+$. The use of the B3LYP* functional within the framework of (time-dependent) density functional theory has been proven to be suitable to obtain accurate geometries, vibrational frequencies and relative energies of the states involved in the thermal and light-induced spin-crossover of the two Fe(III) complexes. The adiabatic HS-LS energy difference is in reasonable agreement with the estimate calculated with multiconfigurational wave function techniques (CASSSCF/CASPT2) and the

Φ_I	Φ_F	SO term [cm^{-2}]	Vibrational term [cm^2s^{-1}]	t [s]
^{2}LMCT	IS	2.26×10^2	7.94×10^8	1.26×10^{-9}
^{2}LMCT	HS	1.14×10^1	5.54×10^7	1.81×10^{-8}
IS	HS	1.35×10^5	2.45×10^{13}	4.08×10^{-14}
IS	LS	1.20×10^5	6.66×10^{12}	1.50×10^{-13}
HS	LS	7.89×10^1	5.01×10^5	1.99×10^{-6}

Table 4.6: Intersystem-crossing rates between all states of the $[Fe(qsal)_2]^+$ involved on the LIESST phenomenom.

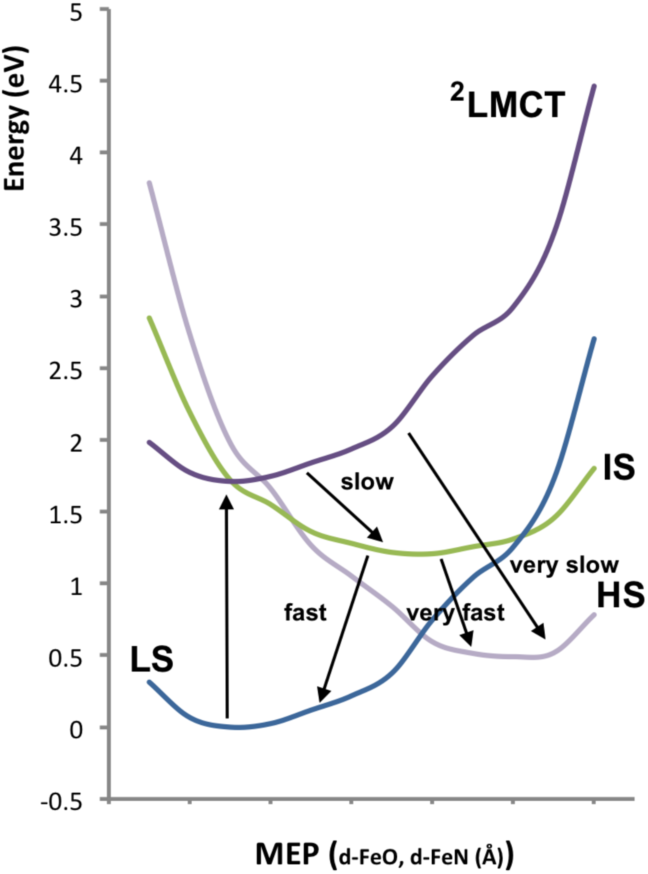

Figure 4.10: Graphical representation of the photocycle of the $[Fe(qsal)_2]^+$ showing the different deactivation paths.

$T_{1/2}$ that we derived by combining the ΔE_{HL} with the zero-point energy corrections and the entropy contributions is on the same order of magnitude as the experimental transition temperature for spin crossover. The TD-DFT/B3LYP* calculations gives a good account of the absorption spectrum with an intense band of ligand-to-metal charge transfer character in the expected region.

After this pertinent validation, the study of the LIESST mechanism in Fe(III) has been performed. The two-dimensional scan of the energy surface of LS and HS states as function of the Fe-N and Fe-O distances defines an approximate reaction coordinate for the deactivation of the excited doublet state to the final, metastable HS state. Alternative choices such as the Fe-N distances and the changes in the O-Fe-N angle lead to slightly different reaction paths, but the main features are expected to be the same. The TD-DFT calculations along the reaction path define the potential energy curves of the electronic states involved in the LIESST process. We observe that after the excitation of the system in the ^{2}LMCT state, it can undergo an intersystem crossing with the IS in the Franck-Condon region and subsequently convert to the HS state via a second intersystem crossing close to the first one. The IS→LS crossing is found slightly displaced towards the HS minimum along the reaction path.

More information about the deactivation has been obtained by calculating the intersystem crossing rates with the time dependent formulation of Fermi's golden rule as done before in $[\text{Fe(bpy)}_3]^{2+}$[60, 61]. In addition to the energy differences and the vibrational modes, one also needs the spin-orbit coupling matrix elements between the electronic states. These were calculated with the state interaction method based on CASSCF wave functions, second-order couplings were incorporated by an effective Hamiltonian treatment. The calculated rates let us propose two competing pathways in the photocycle of the LIESST process. After a relatively slow ^{2}LMCT→IS intersystem crossing, the system can deactivate very rapidly to the final HS state or fall back on the initial LS state. This scenario of two competing pathways is in agreement with the low efficiency of the LS-HS conversion found in experiment. There are several differences with the LIESST mechanism of the Fe(II) complexes. In the first place, the process is expected to be significantly slower because of the small spin-orbit coupling between the ^{2}LMCT and the IS state. Secondly, the first intersystem crossing cannot take place in the LMCT manifold as the ^{4}LMCT state lies too high in energy, and therefore, necessarily involves a ligand-field quartet state. Finally, the efficiency of the process is much smaller than in the Fe(II) complexes due to the competition between the IS→LS and IS→HS pathways.

One should be aware that the calculation of the intersystem crossing rates with Fermi's golden rule gives a first rough estimate and that non-adiabatic effects are not included. To obtain a more complete description one should rely on the previously mentioned MCTDH or excited state molecular dynamics methods. However, these methods also have some drawbacks. The quality of the MCTDH results rely critically on the choice of the vibrational modes included int he model Hamiltonian, in contrast to the application of Fermi's rule, which considers all vibrational degrees of freedom. The molecular dynamics with surface hopping are very costly and it is far from trivial to include enough electronic states to scan all possible deactivation paths. A combination of the three schemes would most probably give a more complete description of the photocycle.

4.5 Post-publication: B3LYP* vs. Experimental Fe(III) Spectra

It has not been possible to find the experimental absorption spectrum of $[\mathrm{Fe(qsal)_2}]^+$ and $[\mathrm{Fe(pap)_2}]^+$ in the literature. Therefore we have selected two other Fe(III) complexes with a well-known spectrum, the $\mathrm{Fe(acpa)_2}$ and $\mathrm{Fe(Sal_2tr)}$ [225, 226], to check the efficiency of predicting the absorption spectrum with TDDFT/B3LYP* in Fe(III) complexes. Figures 4.11 and 4.12 show the theoretical spectrum of the 100 first doublets and sextets with the methodology mentioned before. The B3LYP* prediction for the LS state is in rather good agreement with the experimental spectrum, especially if we apply a small red-shift of 0.20 eV in the case of $\mathrm{Fe(acpa)_2}$, whereas no shift is needed for $\mathrm{Fe(Sal_2tr)}$. Moreover, we can identify the bands between 1.8-2.0 eV (600-650 nm) as LMCT bands, in agreement with the experimental assignment. On the other hand, the calculated spectrum for the HS state represents less accurate the experimental spectrum. Bigger shifts (0.40 eV) are needed as well as wider gaussians (full-width at half height of 1 eV) for both complexes. In conclusion, the method predicts reliable results for the low-spin states, but it is not capable of giving accurate information about excited states with high-spin multiplicity.

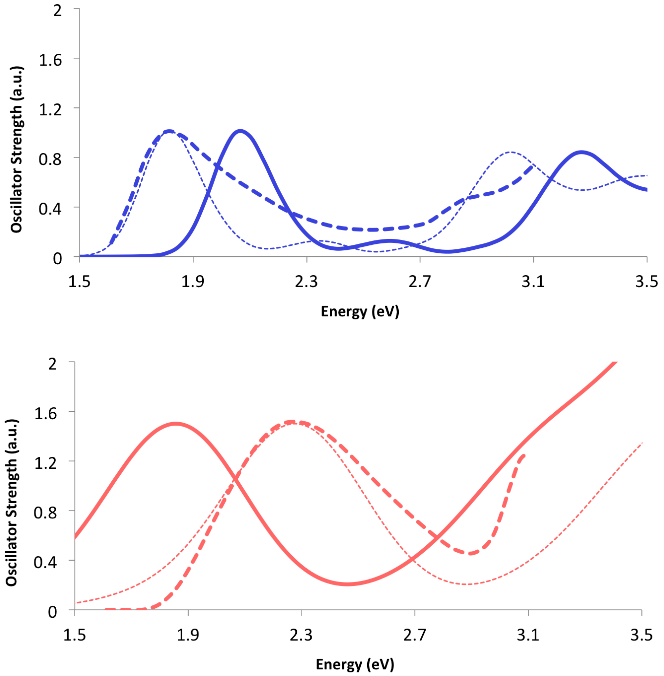

Figure 4.11: Comparison of the TDDFT/B3LYP* (red lines) and the experimental (black dashed line) absorption spectrum of the LS (upper panel) and HS (lower panel) of Fe(acpa)2. The solid red line is obtained by placing gaussian functions centered at the transition energies of FWHM = 0.3 eV for the LS and 1.0 eV for the HS. The dashed red line is obtained by shifting all transitions by -0.2 eV (LS) or +0.4 eV (HS). The height of the gaussians is an indication of the oscillator strength relative to the maximum of the experimental spectrum.

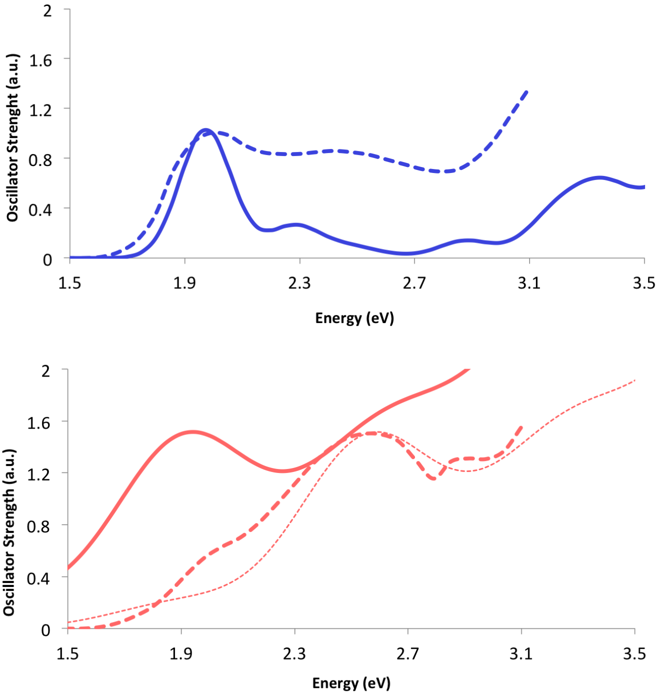

Figure 4.12: Comparison of the TDDFT/B3LYP* (red lines) and the experimental (black dashed line) absorption spectrum of the LS (upper panel) and HS (lower panel) of Fe(Sal$_2$tr). The solid red line is obtained by placing gaussian functions centered at the transition energies of FWHM = 0.3 eV for the LS and 1.0 eV for the HS. The dashed red line in the HS spectrum is obtained by shifting all transitions by +0.4 eV (HS). The height of the gaussians is an indication of the oscillator strength relative to the maximum of the experimental spectrum.

CHAPTER 5

Delving into the Magnetic, Electronic and Geometrical Parameters of P450-I and CPO-I

5.1 Introduction

Cytochromes P450 form a large group of thiolate heme enzymes that catalyze the functionalization of a wide variety of compounds by the insertion of an activated oxygen atom into an inert C–H bond [237–240]. The mechanism for P450 hydroxilation involves a radical intermediate called compound I (P450-I), which has been proposed to be an $\mathrm{Fe^{IV}}$ (*i.e.*, $\mathrm{d^4}$ configuration) surrounded by an oxo, a thiolate and a porphyrin ligand, with a radical delocalized over the last two ligands. Due to the important role of these enzymes, many experimental and theoretical investigations have been carried out since its discovery in the 1960's [241–243]. These studies have evidenced the existence of the P450-I and have demonstrated that the reactivity can change depending on the donation character of the axial ligand [244–247]. However, the electronic structure of the P450-I has not been well-characterized due to its very short life-time and the difficulties to trap it [240, 248, 249]. Thus, the enzyme chloroperoxidase (CPO) has been used as valuable model system to study the P450 chemistry. Chloroperoxidase compound I (CPO-I), which is a thiolate-ligated ferryl radical similar to P450-I, is sufficiently stable to extract information about the geometric and electronic structure using spectroscopic techniques [250–253]. The latter can eventually be used to clarify the structure and reactivity of P450-I.

Theoretical studies have played an important role in order to complement the experimental studies. A versatile strategy to study the electronic behaviour of the huge biological systems is to use a biomimetic model system that acts similarly as the actual biomolecule. Most of the theoretical studies were done using iron-porphyrin models with the structure (SR)$\mathrm{Fe^{IV}}$(O)(Porph) (R= H, Me or Cys) as represented in Fig. 5.1. The first studies were done by Loew and Harris probing the nature and the role of the different intermediates combining density functional theory (DFT) and semiempirical INDO/SCF/CI method [254–258]. Thereafter, many other studies have been published reporting DFT or multiconfigurational calculations [259–265]. For a more rigorous description of the biological system, QM/MM calculations have been performed on P450-I with a considerable degree of success [266–271]. Provided the QM region is large enough, very accurate results have been extracted. As general conclusion from these investigations is that the low-lying states of P450-I comprise a nearly degenerate triradicaloid manifold of doublet and quartet states. At slightly higher energy, one can find a sextet state with two extra unpaired electrons on the Fe ion. Considering the lowest states, two unpaired electrons are associated with the Fe=O unit, but the calculations are less unanimous on where to place the third unpaired electron. The investigations that have used biomimetic models with an –SH ligand at the axial position suggest that the third electron is delocalized over the porphyrin ring. In contrast, when –$\mathrm{SCH_3}$ is used as axial ligand, there is an important spin population on sulfur. The two scenarios lead to important differences in both the geometry and the electronic structure of the complexes. Being directly associated with the axial coordination of the metal, these differences are expected to have a significant effect on the reactivity.

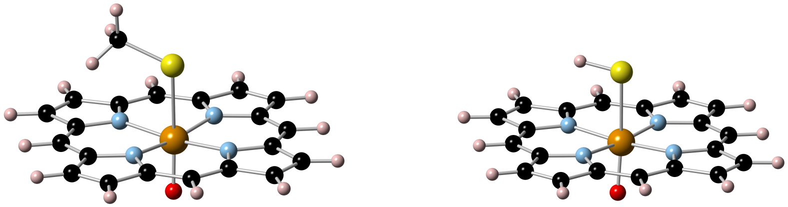

Figure 5.1: Ball and stick representation of the (SR)Fe^{IV}(O)(Porph) models used: R=CH_3 (left) and R=H (Right). Color code: orange for Fe, red for O, yellow for S, black for C, blue for N and pink for H.

Recently, Green and co-workers have suggested that the larger reactivity of the cytochrome P450-I as compared to CPO-I is related to the shorter Fe-S distance in the former [272]. The larger exchange splitting –proportional to the energy difference of the doublet and quartet spin state (see *below*)– of P450-I was suggested to be an indication of higher spin density on sulphur with respect to the CPO-I analogue. The goal of the present study is unravel the origin of magnetic properties in P450-I and CPO-I complexes combining wave function and DFT-based calculations using a biomimetic model, (SCH_3)Fe^{IV}(O)(Porph), represented on the left in the Figure 5.1, the one on the right has been used to clarify the spin density changes induced by –SR. A detailed analysis of the electronic density and evaluation of the exchange coupling and magnetic anisotropy constants is proposed to stress the importance of axial ligand distance in dictating magnetic properties.

5.2 Computational Information

All geometries were optimized using the hybrid functional B3LYP*[83, 84], which reduces to 15% the exact Fock exchange used in the standard B3LYP functional. This functional has previously shown its ability to accurately describe geometries and adiabatic energy differences between states of iron complexes with different oxidation states. The molecular orbitals are expanded with the default triple-ζ basis set with one polaritzation function (def2-TZVP) [161]. The so-obtained geometries are compared to the ones resulting from B3LYP and PBE0 (which adds 25% of exact Fock exchange to the standard PBE functional [136]) calculations to determine the dependence of the FeS distance on the computational method. The optimal geometries of the sextet (high spin, HS), quartet (intermediate spin, IS) and doublet (low spin, LS) states of the complex were determined without imposing symmetry constraints and characterized as minima by a vibrational frequency calculation.

The DFT calculations were performed within the ORCA package version 3.0.1[207]. To reduce the computational cost implicit to the use of hybrid functionals, we have activated the RIJCOSX procedure [208] to speed-up the calculation of the exchange contribution to the energy. Vibrational frequencies were calculated by numerical differentiation of the analytical gradients.

Thereafter, a series of B3LYP* optimized structures was generated by restricted geometry optimizations varying the Fe=O and the Fe–S distances in the intervals 1.55–1.75 Å and 1.95–2.60 Å, respectively. These points have been used as input for multiconfigurational wave function calculations to obtain additional information about the electronic structure of the complex. Complete active space self-consistent field (CASSCF) and subsequent second-order perturbation theory (CASPT2) were performed as implemented in MOLCAS 7.4 [166, 167]. Atomic natural orbital (ANO) basis sets optimized for scalar relativistic effects and core correlation were applied for all atoms [168, 169]. We used a (7s,6p,5d,4f,3g,2h) contraction for Fe, (5s,4p,2d) for S, (4s,3p,1d) for N and O, (3s,2p) for C and (2s) for H. The Cholesky decomposition [170, 171] was used to reduce the computational cost associated to the calculation of the two-electron integrals. Scalar relativistic effects were included using Douglas-Kross-Hess Hamiltonian [172].

The active space to construct the CASSCF reference wave function contains 15 electrons and 14 orbitals and was used to explore the multiconfigurational character of the electron structure on a 2D potential energy surface as function of the Fe=O and Fe–S distances. A graphical representation of the active orbitals is given in the supporting information, but we will give a short description here using the labels of Figures S1.1 to S1.5 of *Chapter5: Sup. Info* in ioChem-bd (DOI:10.19061/iochem-bd-2-3). Among the five Fe-3d orbitals, only the Fe-3d$_{x^2-y^2}$ and the Fe-3d$_{xy}$ orbitals remain practically atomic (ψ_5, ψ_{11}). The Fe-3d$_{xz}$ forms bonding and antibonding combinations with the O-2p$_x$ orbital (ψ_1, ψ_4) and the Fe-3d$_{yz}$ orbital strongly mixes with the O-2p$_y$ and S-3p$_y$ orbitals (ψ_6, ψ_8, ψ_{10}). The Fe-3d$_{z^2}$, O-2p$_z$ and S-3p$_z$ constitute three more molecular orbitals of σ character (ψ_3, ψ_7, ψ_9). The eleventh active orbital (ψ_2) is a σ-orbital arising from the N atoms of the porphyrin ring. The three remaining orbitals are the so-called 3d' orbitals and account for the double-shell effect to introduce more flexibility on the charge redistribution between the metal and the ligands. We have only added the Fe-3d' t_{2g}-like orbitals because the 3d' orbitals associated to the Fe-3d$_{e_g}$ orbitals could not be forced into the active space. Since the occupation numbers of the latter are almost zero, the electron correlation associated with these orbitals is very small.

Some calculations were done with a larger active space, obtained by adding two occupied π and two unoccupied π^* orbitals of the porphyrin system. This extension of the active space allows us to study to what extent the third unpaired electron is shared by sulphur and porphyrin. The large number of orbitals and electrons makes a full CASSCF treatment impossible and therefore we opted for the less demanding Restricted Active Space variant, RASSCF to build the reference wave function. To limit the wave funtion expansion, we allowed at most 2 holes in the two π orbitals and at most two electrons in the π^* orbitals.

CASPT2 and RASPT2 calculations [89, 145, 273] account for the remaining electron correlation by correlating all the electrons except the deep core electrons (1s^2 for N, O and C and 1s^{2}2s^{2}2p^6 for Fe). In order to exclude possible intruder states, we applied an imaginary level shift of 0.15 a.u. in CASPT2 [147]. In the calculations of the exchange coupling constant, we have used the difference dedicated configuration interaction method (DDCI) [149] to include electron correlation effects. This method is known to provide very accurate estimates of the coupling in a wide variety of complexes [119].

Analysis of the electronic structure was performed by an orthogonal valence bond reading of the CASSCF wave function using localized orbitals. The canonical active CASSCF orbitals shown in Fig. S1 are delocalized over several atoms. They have been transformed into strongly localized orbitals by rotations of bonding and antibonding MO pairs as described in Ref. [182]. Another, more general localization scheme has been used to transform the inactive and virtual orbitals into a localized form and subsequently reduce the MOs space used in the DDCI calculations. The canonical MOs are transformed by following a valence-bond-like description of the electronic density, which is based on one of the Kekulé structures of the molecule and allows us to spatially separate the orbitals [153, 274–276]. The method has proven to be extremely efficient not only to reduce in a rational way the number of inactive and virtual MOs in post CASSCF treatments [277–280], but also to analyze the relevance of chemical regions in energy differences [281].

5.3 Results and Discussion

Geometry, Vibrations and Energetics at DFT level

The optimized geometries of the complex are rather similar for the three spin states. As will be discussed below, the LS and IS state share the same electronic configuration, and hence, it is not surprising that their geometries are practically identical. The electronic configuration of the HS state is different but the antibonding Fe-3d e_g-like orbitals remain unoccupied as in the other two spin states. Therefore the coordination sphere does not expand from LS to HS, in contrast with what is typically observed in the prototypical Fe(II) spin crossover complexes.

The Fe=O distance is only weakly dependent on the functional applied and in good agreement with the available experimental data. On the other hand, the Fe-S distance is more sensitive to the details of the density functional and is in general overestimated by at least 0.1 Å when compared to the X-ray structure of CPO-I and even more with respect to the P450-I data (see Table 5.1). The DFT calculations are performed within the spin-unrestricted formalism, and hence, the resulting electronic states are not necessarily eigenfunctions of the $\hat{S}^2$ operator. The spin contamination for the HS and IS states is reasonably small, the expectation values of $\hat{S}^2$ being 8.80 and 3.77, very close to the theoretical values of 8.75 for a sextet and 3.75 for a quartet state. The situation is slightly more complicated for the LS state. In principle, a doublet spin state $\hat{S}^2$ expectation value should be 0.75, whereas a value as large as 1.76 is calculated. However, if one realizes that the electronic state is actually an up-up-down arrangement of three unpaired electrons (see *below*), the nearly 1.75 value is expected since it corresponds to the expectation value of the $|\alpha\alpha\beta|$ determinant.

Based on the calculated distances, the PBE0 and B3LYP* functionals are the best candidates to continue the DFT calculations and

Table 5.1: Some relevant geometrical parameters of the DFT optimized structures for LS, IS and HS states of the (SMe)Fe^{IV}(O)(Porph) (distances in Å and angles in degrees). The experimental values are given for comparison [253, 272].

Method	r(Fe-S)	r(Fe-O)	r(Fe-N)$^{(a)}$	$\measuredangle$ (Fe-S-CH$_3$)
DFT-PBE0				
LS	2.52	1.61	2.00	109.5
IS	2.57	1.61	2.00	109.1
HS	2.61	1.61	2.07	109.8
DFT-B3LYP				
LS	2.62	1.62	2.02	110.1
IS	2.68	1.62	2.02	109.7
HS	2.73	1.62	2.08	110.3
DFT-B3LYP*				
LS	2.58	1.63	2.02	109.9
IS	2.62	1.63	2.02	109.7
HS	2.62	1.63	2.08	110.3
Exp. CPO-I	2.48	1.66		
Exp. P450-I	2.39	1.67		

(a) Average of the four Fe-N distances

elaborate on the vibrational frequencies and the energetics of the system. It is well known from previous studies of Fe(II) [62] and Fe(III) [282] complexes that the B3LYP* functional gives much better relative energies than PBE0, and therefore, we will continue from now on with this functional.

Table 5.2 shows the vibrational frequencies of the stretching modes associated to the Fe-L_6 core of the complex. In the first place, we see that the frequencies are similar for the three spin states, as a result of the small differences in the geometry. The comparison with experiment reveals a difference of almost 100 cm^{-1} between the calculated and experimental Fe=O frequency. This softening of the Fe=O bond in CPO-I with respect to the typical value around 890 cm^{-1} of the stretching in the ferryl group has be ascribed to interactions of the O atom with H on distant groups of the protein [261, 283].

Finally, we shortly discuss the relative energies of the spin states. Given the reasonable B3LYP* results in Fe(II) and Fe(III) complexes [62, 83, 282], it is expected that the DFT energies of the three spin states offer a qualitative description of their ordering. Table 5.3 lists the contribution of the electronic energy, the zero-point vibration and the entropy contribution at 300 K to the LS-IS and the LS-HS energy difference. The entropy contribution also contains a small temperature-independent term arising from the larger degeneracy of the electronic state with increasing S [215]. B3LYP* shows that the LS and IS states to be nearly degenerate, the electronic energy is slightly in favor of the LS but the entropy

Table 5.2: Frequencies in cm^{-1} of the Fe-L stretching modes for the three spin states of $(SMe)Fe^{IV}(O)(Porph)$. Experimental frequency from Ref. [284]

	$(SMe)Fe^{IV}(O)(Porph)$			
Character	LS	IS	HS	Exp.
Fe-S	125	124	117	
Fe-N_4	234	233	178	
	271	270	243	
	276	275	252	
	370	370	368	
Fe-$O^{(a)}$	875/890	873/890	877/897	790

$^{(a)}$The Fe-O stretching is strongly coupled to a C-H bending and has large contributions in both normal modes.

contribution inverts the relative stability around $T = 250$ K. The zero-point energy (ZPE) does not affect the LS-IS energy difference. Because of the nearly identical geometry, the correction is practically the same for both states. On the contrary, the HS state is predicted to lie much higher in energy, 5000 cm^{-1} above the LS state, and despite the entropy effects lower the HS energy, it can safely be assumed that this state does not play a role in the main characteristics of the complex.

As for the spin density, we have analyzed the distribution of the unpaired electrons by Mulliken spin populations. Table 5.4 compares the populations on the Fe, O, S and the sum of all atoms of the porphyrin ligand for $(SMe)Fe^{IV}(O)(Porph)$ to those of the complex where the S-CH_3 is replaced by S-H. The substitution of CH_3 by

Table 5.3: B3LYP* adiabatic electronic energy difference ΔE, zero-point energy difference ΔZPE, entropy contribution ΔS ($T = 300$ K) and free energy difference ΔG for (SMe)Fe$^{\mathrm{IV}}$(O)(Porph). Energies in cm^{-1}.

	ΔE	ΔZPE	ΔS	ΔG
LS-IS	135	0	-160	-25
LS-HS	5003	-443	-436	4123

Table 5.4: B3LYP* spin populations in the HS, IS and LS states for (SMe)Fe$^{\mathrm{IV}}$(O)(Porph) and (SH)Fe$^{\mathrm{IV}}$(O)(Porph)

	(SMe)Fe$^{\mathrm{IV}}$(O)(Porph)			(SH)Fe$^{\mathrm{IV}}$(O)(Porph)		
	HS	IS	LS	HS	IS	LS
Fe	3.17	1.19	1.24	3.09	1.18	1.24
O	0.59	0.87	0.84	0.67	0.88	0.83
S	0.71	0.73	-0.75	0.49	0.58	-0.62
Porphyrin	0.52	0.22	-0.33	0.75	0.37	-0.47
Total	5	3	1	5	3	1

an H atom does not greatly modify the spin denisties on the Fe ion, but induces slightly larger delocalization onto the porphiryn and slightly lower on the sulphur. The spin populations indicate that three of the five unpaired electrons of the HS state are localized on the Fe atom supporting a formal Fe(V) oxidation state in both complexes. The other two unpaired electrons are shared by O, S and the porphyrin ring. In the IS and LS states, two electrons pair in the low-lying Fe-3d_{xy} orbital (the porphyrin is in the xy-plane with the N-atoms positioned on the x and y axis), leaving one unpaired electron for Fe. In both states we find a spin density close to 1 on O of the same sign as the spin density on Fe, meaning a parallel (or ferromagnetic) alignment of the spins in the Fe=O unit. The remaining spin density is mostly localized on S for the complex with the S-CH_3 axial ligand, while the other complex shows a larger tendency to share the unpaired electron between S and the porphyrin ring. As can be seen in Fig. 5.2, the residual spin density on the porphyrin ring arises from the overlap of the S-3p orbital holding the unpaired electron and a 2p_z orbital of one of the porphyrin N-atoms. This spin density analysis clearly supports a triradicaloid nature of the electronic structure of the IS and LS states. In the IS state the three electrons have a parallel alignment and in the LS state the third unpaired electron is antiferromagnetically coupled to the two electrons in the Fe=O unit, characteristic of an $|\alpha\alpha\beta|$ determinant with the already mentioned 1.75 value of $\langle \hat{S}^2 \rangle$.

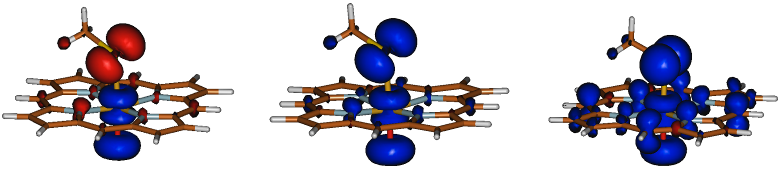

Figure 5.2: DFT/B3LYP* spin density representation of the LS, IS and HS over the optimized DFT/B3LYP* structure.

CASPT2 geometries and energies

To check the relative energies and the distribution of the unpaired electrons calculated within the DFT framework, we have performed multiconfigurational wave function calculations over the (SMe)Fe^{IV}(O)(Porph) structure. These calculations work with the exact Hamiltonian and eigenfunctions are $\hat{S}^2$ pure eigenfunctions. A full CASPT2 geometry optimization is beyond our computational possibilities. Instead, we have performed single point CASPT2 calculations on the series of DFT/B3LYP* structures with different Fe-S and Fe-O distances as explained in the computational information. Such approach not only gives an estimate of the optimal CASPT2 Fe-S and Fe-O distances but, more importantly, also provides us with insight in the changes in the electronic structure when these two distances are modified. One can anticipate that the reactivity of CPO-I and P450-I should be better understood following this analysis.

Figures 5.3 and 5.4 summarize the results of the CASPT2 calculations for the LS and IS in the form of 2D potential energy surfaces. The Fe-O optimal distance is very similar for both spin states, around 1.65 Å, basically the same outcome as found in the DFT calculations. The Fe-S distance is less well defined. The potential energy surface of the IS has a clear minimum around 2.5 Å, only a little shorter than the B3LYP* results. However, the LS surface shows a flat valley spanning Fe-S distances from 2.1 Å to 2.5 Å in which the energy of the LS state changes by less than 500 cm^{-1}. Calculations with a smaller active space pins the Fe-S optimal distance at much too short distances (~2.1 Å, see Figure S2.1 of *Chapter5: Sup. Info* in ioChem-bd (DOI:10.19061/iochem-bd-2-3). The present active space clearly tends to enlarge the bond distance, but it is clear that it is still not large enough to get a fully satisfactory description of the energetics. A further extension would, however, lead to wave function expansions that are quite hard to handle, not only from the point of view of computational resources, but also with respect to the convergence of the CASSCF procedure.

At the lowest point of the IS PES, the CASPT2 energy difference between IS and LS is 530 cm^{-1} with the LS lower in energy, in agreement with the previous B3LYP* findings. A full account of the free energy is not easily accessible from the wave function based calculations because the vibrational entropy contribution cannot be determined, but the similarity of the electronic energy difference, adds confidence to the conclusion drawn from the B3LYP* calculation. The LS and IS states are very close in energy and that their relative stability depends on subtle details not included in the present model complexes.

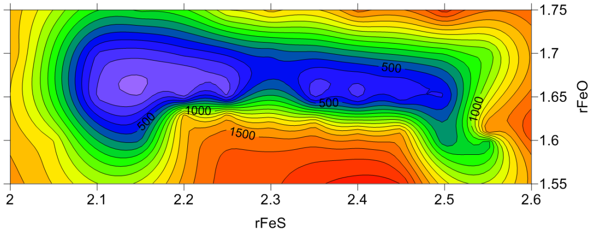

Figure 5.3: CASPT2 potential energy surface as function of the Fe-S and Fe-O distances (Å) of the LS state. Energies (in cm^{-1}) are relative to the total energy of the LS minimum.

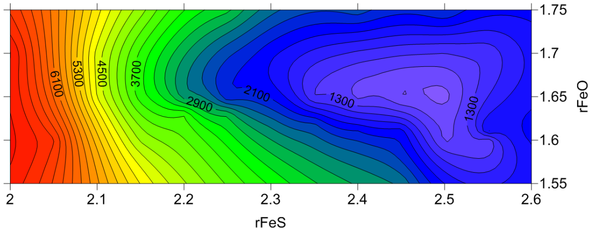

Figure 5.4: CASPT2 potential energy surface as function of the Fe-S and Fe-O distances (Å) of the IS state. Energies (in cm^{-1}) are relative to the total energy of the IS minimum

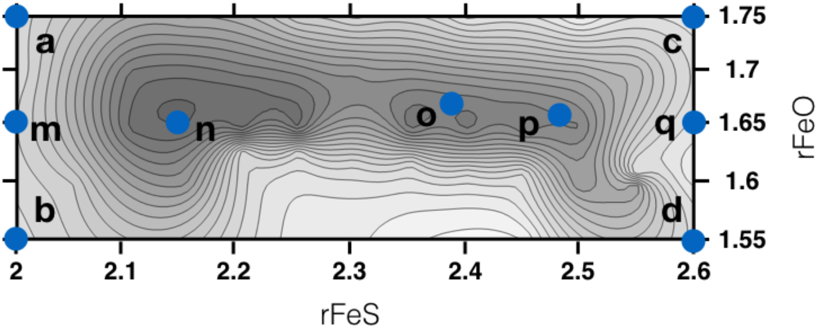

Figure 5.5: Collection of points on the 2D surface for which the electronic structure is analyzed in terms of spin populations and electron count on the different atoms. $a \dots d$ represent geometries with the longest/shortest Fe-S and Fe-O distances (Å), $m \dots q$ explore the valley of similar LS energies of Fig. 5.3, with o and p corresponding to the P450-I and CPO-I geometries, respectively.

Wave Function Analysis

The electronic structures of P450-I and CPO-I has been much debated in the literature [255, 258–260, 262, 264–271]. In particular, one would like to specify the spin density and the metal center oxidation state. Given the uncertainty on the optimal geometry of the LS state, we have analyzed the electronic structure of the complex for a collection of points on the potential energy surface and focus on the distribution of the unpaired electrons as function of the Fe-S and Fe-O distances, suggested to be key parameters in the reactivity of CPO-I and P450-I.

Figure 5.5 marks the geometries that have been selected to analyze the composition of the multiconfigurational wave function and the spin density population on the different parts of the complex as done for the DFT-based calculations. In addition to the four corners (points $a \ldots d$), we have also selected five points in the low-energy valley of the LS PES ($m \ldots q$). The o and p points are geometries that are very close to the reported X-ray active center structures of P450-I and CPO-I, respectively.

Table 5.5 summarizes the spin populations of Fe, O, S and porphyrin calculated from the CASSCF wave function of the LS, IS and HS states. In the first place, it is clear that the spin populations for LS and IS are compatible with the triradicaloid character of the electronic structures. As a general feature, we observe that the spin density on the porphyrin is small in all points and graphical inspection of the spin density shows that it arises from the overlap of the singly occupied S-3p orbital with a 2p orbital of one of the N atoms of the porphyrin ligand (see Figure S1.6 in *Chapter5: Sup. Info.* of the ioChem-bd, DOI:10.19061/iochem-bd-2-3). This observation is consistent with the DFT calculations, albeit that the CASSCF spin density is more localized on the S atom. The spin population on the O atom hardly changes with the Fe=O distance, whereas there is a certain tendency towards larger spin population on S for larger Fe-S distances. The HS state has a large Fe spin population and also shows a significant delocalization of the unpaired electrons onto the porphyrin ligand.

Simultaneously, we have performed an orthogonal valence bond reading of the multiconfigurational wave function and calculated the electron count on Fe, O, and S atoms to have an approximate

	LS				IS				HS			
	Fe	O	S	Porph.	Fe	O	S	Porph.	Fe	O	S	Porph.
a	0.51	0.60	-0.10	0.01	-	-	-	-	3.50	0.80	0.53	0.16
b	0.65	0.49	-0.13	0.00	1.17	0.86	0.91	0.04	3.32	0.59	0.91	0.17
c	0.82	0.51	-0.32	0.01	1.24	0.76	0.96	0.02	3.82	0.04	0.97	0.16
d	0.85	0.51	-0.32	0.00	1.28	0.73	0.96	0.02	3.54	0.33	0.96	0.15
m	0.59	0.54	-0.12	0.01	1.12	0.95	0.88	0.03	3.35	0.61	0.86	0.17
n	0.69	0.53	-0.21	0.01	1.17	0.86	0.93	0.03	3.48	0.40	0.94	0.17
o	0.83	0.52	-0.31	0.01	1.23	0.78	0.95	0.03	3.63	0.24	0.96	0.16
p	0.83	0.51	-0.32	0.01	1.25	0.75	0.96	0.02	3.63	0.23	0.96	0.16
q	0.85	0.49	-0.32	0.01	1.27	0.73	0.96	0.02	3.66	0.21	0.96	0.15

Table 5.5: CASSCF spin populations of Fe, O and S atoms for the LS and IS states on a selection of points with different Fe-O and Fe-S distances.

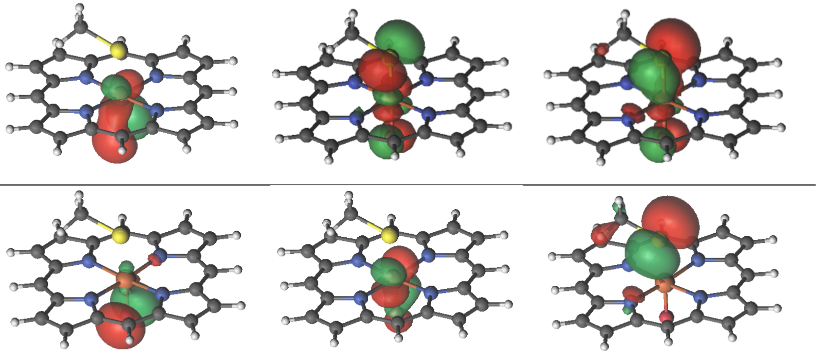

Figure 5.6: Example of localization procedure of the orbitals by rotation. The canonical orbitals (top) are transformed into localized orbitals (bottom).

idea of the total charge of these atoms. Assigning charges to atoms in a complex is of course a very delicate task. However, our goal is to clarify the so-called spectroscopic oxidation state of the Fe center, which can be a Fe^{4+} or Fe^{3+}, following a reported strategy. [285] As an example of the localization procedure, Figure 5.6 illustrates how the three canonical active orbitals of π character, delocalized over Fe, O and S are transformed into localized orbitals of O-2p_x, Fe-3d_{xz} and S-3p_x character. The same is done for the other active orbitals and in Figure S1.5 of *Chapter5: Sup. Info.* of the ioChem-bd (DOI:10.19061/iochem-bd-2-3) all 11 localized active orbitals can be found. After expressing the CASSCF wave function of the LS state in this new set of localized orbitals, we have determined the effective occupation numbers of these atomic-like orbitals and the results are listed in Table 5.6.

The number of electrons associated to each localized orbital (or set of localized orbitals) does not show important variations along the potential energy surface. For all the geometries here considered, the d-electron count for Fe is between 5.3 and 5.6. Two electrons are located in the Fe-3d$_{xy}$ orbital and the other two Fe-3d$_{t_{2g}}$-like orbitals (d$_{xz}$ and d$_{yz}$) are both occupied by 1.3 electrons. The Fe-$3d_{z^2}$ holds 0.75 electrons, whereas the Fe-3d$_{x^2-y^2}$ remains empty in all geometries. Distributed almost equally over the three 2p-orbitals, the O atom has approximately 4 electrons in its 2p-shell. Combined with the information on the spin density, we therefore, conclude that the electronic distribution in the oxoferryl moiety (FeO) is best described by the more covalent situation Fe^{3+}–O$^{\bullet}$, as previously reported by Banse *et al.*[285]. The two p-orbitals localized on the sulphur atom have three electrons, one in the 3p$_x$ and two in the 3p$_z$ orbital. The third S-3p orbital is among the inactive orbitals and hence doubly occupied. Thus, the electronic configuration of S is 3p^5, compatible with a S$^-$ ion.

Exchange Coupling Parameter and Axial Anisotropy

The last step of the analysis of the electronic structure concerns the magnetic properties of the complex. These have been ascribed to arise mainly from the exchange coupling between the Fe=O (S_1=1) unit and the unpaired electron on sulphur (S_2=$\frac{1}{2}$) combined with an axial magnetic anisotropy arising from the unpaired electrons of the oxoferryl. The corresponding model Hamiltonian can be written as $\hat{H} = -J\hat{S}_1 \cdot \hat{S}_2 + D(\hat{S}^2_{z,1} - 2/3)$, where $\hat{S}_1$ and $\hat{S}_{z,1}$ are the total spin operator and its z-component accounting for

Table 5.6: Electron count of Fe-3d, O-2p and S-3p type-orbitals

	Fe-3d	O-2p	S-3p
a	5.61	4.04	1.05
b	5.47	4.09	1.11
c	5.53	4.32	0.98
d	5.52	4.31	0.98
m	5.53	4.09	1.09
n	5.30	4.26	1.10
o	5.51	4.31	0.99
p	5.51	4.32	0.98
q	5.51	4.33	0.98

the unpaired electrons of Fe=O and $\hat{S}_2$ is the total spin operator of the third unpaired electron, mostly localized on S [272]. This expression explicitly assumes that the rhombic anisotropy of Fe=O is negligible and that the total anisotropy of the whole complex is solely due to the unpaired electrons on Fe=O.

We have followed a two-step procedure to analyze the magnetic properties. In the first place, we have calculated the relative energies of the lowest three Kramers doublets that originate from the LS and IS states following the usual procedure of diagonalizing the spin-orbit Hamiltonian expressed in terms of CASSCF basis functions with energies on the diagonal corrected for dynamical correlation [111, 116, 174, 286]. From the two energy differences we have extracted D and J as defined by the model Hamiltonian used in experiment (see Section S3 of *Chapter3: Sup. Info.* of the ioChem-bd, DOI:10.19061/iochem-bd-2-3), for the model Hamiltonian and

Table 5.7: DDCI exchange coupling J and anisotropy parameters in cm^{-1}. The J value calculated with DFT (Broken Symmetry) has been added for comparison.

	J	D	J^{SF}_{DDCI}	J^{SF}_{BS}	$D_{\mathrm{Fe=O}}$	$E_{\mathrm{Fe=O}}$
m	-3285	15.3	-3265	-1858	18.1	0.1
n			-1443	-1128	17.2	0.3
o	-277	15.2	-269	-368	16.2	0.2
p	-168	15.3	-159	-267	13.1	0.4
q	-71	14.2	-64	-160	10.4	0.1

the corresponding energies expressed in terms of J and D). Secondly, we have divided the magnetic problems in two separate parts: (i) the isotropic exchange coupling between the Fe=O and S was determined directly from the IS–LS energy difference: $J^{SF} = (2/3)(E_{LS} - E_{IS})$ without taking into account spin-orbit coupling (spin-orbit free, SF) and (ii) the axial and rhombic anisotropy parameters $D_{\mathrm{Fe=O}}$ and $E_{\mathrm{Fe=O}}$ were extracted following the procedure outlined in Ref. [111] based on the standard zero-field splitting (ZFS) Hamiltonian $\hat{H} = D_{\mathrm{Fe=O}}(\hat{S}_z^2 - (1/3)\hat{S}^2) + E_{\mathrm{Fe=O}}(\hat{S}_x^2 - \hat{S}_y^2)$. This allows us to verify the assumptions that lead to the model Hamiltonian used so far for the interpretation of the magnetic data.

The magnetic parameters have been calculated in the $m \ldots p$ points of Fig. 5.5 to sample the dependence on the Fe-S distance and compare the outcomes for the CPO-I geometry (point q) to the one corresponding to P450-I (point p). The results for the isotropic (Fe=O)–S exchange interaction J^{SF} can be found in Table 5.7, where we compare the outcomes of the DDCI calculations and those extracted from DFT/B3LYP* calculations relying on the broken symmetry (BS) approach [119, 287]. The J_{BS}^{SF} values were extracted using the equation based on the Yamaguchi relation: $J_{BS}^{SF} = 2(E_{BS} - E_{IS})/(< S_{IS}^2 > - < S_{BS}^2 >)$. As expected, the J^{SF} strongly depends on the Fe-S distance. In fact, $|J^{SF}|$ decays exponentially with the distance [288] as $|J| \propto e^{-\alpha r}$, where α equals -5.8 Å^{-1} for DDCI and -3.9 Å^{-1} for the BS calculations (see Figure 5.7). The axial anisotropy of the Fe=O group is sizeable and and slowly decreasing for longer Fe–S distances. Furthermore, we observe that the rhombic anisotropy is indeed negligible. The comparison of these data extracted from fragment, $D_{\mathrm{Fe=O}}$ and $E_{\mathrm{Fe=O}}$, and spin-orbit free (J^{SF}) calculations, with those extracted from the full complex including spin-orbit coupling shows that there is only a small deviation between the two approaches and that the model Hamiltonian accurately describes the magnetic properties. The calculations predict a $|J^{SF}|$ value 30%(BS) and 40%(DDCI) larger in *o* than in *p*, in agreement with the $|J|$ relation between P450-I and CPO-I obtained by Krest and co-workers [272]. As most salient details, we observe that the spin-orbit coupling slightly enhances the isotropic coupling and that the simultaneous description of all three electrons levels off the variation of the axial anisotropy with the Fe–S distance.

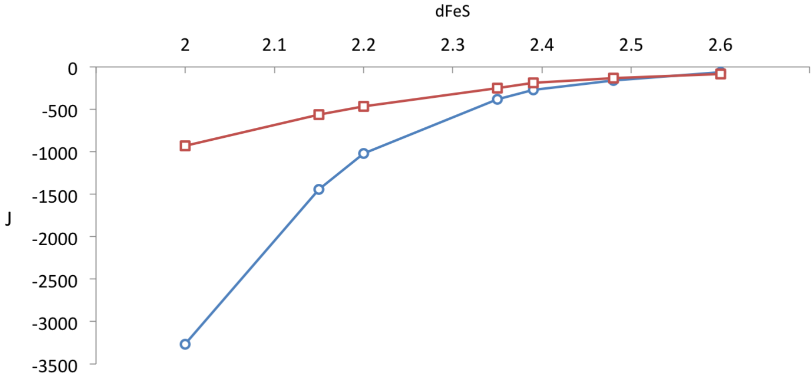

Figure 5.7: Graphical representation of the correlation of the magnetic exchange coupling paramenter (J) along the FeS distance. The DDCI values are depicted by the blue circles and the BS values by the red squares.

5.4 Conclusions

We have analyzed the geometry, electronic structure and magnetic properties of the biomimetic model of the widely studied P450-I and CPO-I, $(SCH_3)Fe^{IV}(O)(Porph)$, using a combination of density functional and wavefunction methodologies. First, we performed DFT/B3LYP* calculations to optimize the geometries, and calculate vibrational frequencies and relative energies of the LS, IS and HS states. The DFT methodology gives accurate Fe=O distance but is not good enough to describe the Fe-S distance, which is more sensitive to the functional used. The vibrational frequencies predicted are similar in the three spin-states in concordance with the small geometry changes. The calculated Fe=O stretching frequency is reasonably similar to the experimentally observed frequency. The DFT/B3LYP* approach situates the LS and IS states in a quasi degeneracy and the HS state at much higher in energy. Additional CASSCF/CASPT2 single point calculations over a series of DFT/B3LYP* structures have been done to better estimate the Fe-S and Fe=O distances and to observe the shape of the potential energy surface of the LS and IS states. The methodology does not properly describe the Fe-S distance because the presence of a flat valley on the LS PES along this distance which complicates the estimation. Moreover, the LS and IS states are close in energy, in line with the prediction of the DFT/B3LYP*.

DFT/B3LYP* and CASSCF coincide in the fact that the electronic structure of the LS state is formed by a triradicaloid configuration with two electrons situated on the Fe=O moiety. The DFT/B3LYP* places the other one on the sulphur ligand with traces over the porphyrin. On the contrary, the CASSCF situates the third unpaired electron completely on the sulphur, being posteriori confirmed by RASSCF. Moreover, we have found evidences that the oxidation state of Fe is halfway between III and IV, being better described by the more covalent configuration Fe^{3+}–$O^{\bullet}$. The last step in the study concerns the magnetic properties along the flat LS valey by using DDCI and Broken-symmetry. The analysis of the isotropic magnetic coupling (J) confirms the antiferromagnetic behaviour and the strong dependence on the Fe-S distance. Even though the axial anisotropy (D) parameter of the ferryl moiety slowly decrease with the Fe-S, the calculated axial anisotropy of the full complex remains constant. Finally, the $|J|$ relation obtained between points o and p is in agreement with the obtained by the experimentals between P450-I and CPO-I.

CHAPTER 6

Amidinium-templated 2D [MnCr] Bimetallic Oxalate-based Networks: The Influence on Structure and Magnetism Explored by Combining Experience and Theory

6.1 Introduction

Since their discovery [289], the rational design of oxalate-based bimetallic networks was followed by a sorting into two robust categories: (10,3) three-dimensional (3D) networks and (6,3) three-dimensional (2D) networks [290]. Based on this rationalisation, it was possible to synthesize targeted multifunctional magnets to observe cross-effects such as magneto-chiral dichroism [291] or magnetisation-induced second harmonic generation, for example [292]. Few exceptions to these architectures and stoechiometries were presented in the literature and were considered as exotic cases [293, 294], that did not invalidate the general scheme of synthesis. Recently, to favour the appearance of new properties under electric field [295–298], cations with H-bonding abilities were introduced as templating agents in the oxalate-based [MnCr] bimetallic coordination networks. It then appeared a competition between the formation of hydrogen and coordination bonds. The latter holding the anionic network, the insertion of such cations deeply modifies the coordination network [296–298] or even prevents its formation [299–301]. The evolutions of the coordination network are related to variations of the manganese(II) coordination environment and/or of the oxalate bridging mode. The presence of methanol molecules in the crystal lead to hepta-coordinated Mn ion, a rather unusual situation we should like to examine. In parallel to these structural changes, modifications in the exchange interactions and Long Range Magnetic Ordering (LRMO) were observed. A dramatic change from ferromagnetic to antiferromagnetic of the Mn(II)-Cr(III) exchange interaction was tentatively attributed to the sweeping from a bisbidentate to a bidentate/monodentate bridging mode of the oxalate ligand [302]. Along this line, we intend to bring new examples of distorsion of the coordination sphere around the metallic centres. This influence of the bridging mode of the oxalate must be further tested experimentally and theoretically confirmed to be validated. For this purpose, using the template effect induced by organic species is an appealing strategy. Amidinium-containing cations may offer a possibility to test the proposed magneto-structural correlation since they are known to be active H-bonds donors and offer numerous possibilities of functionalization [303–306]. Theoreticians have reported, since the first application to magnetic ordering in transition metal compounds done by Wachters and Nieuwpoort in 1972 [307], accurate strategies for analyzing the exchange coupling constants in bimetallic complexes with bridging ligands through *ab initio* calculations [105, 109, 110, 114, 280, 308, 309].

In this chapter, the synthesis structure and magnetic properties, of three [MnCr] oxalate-based compounds obtained by using three different amidinium-based cations, namely 1,4-bis(1,4,5,6-tetrahydropyrimidinium-2-yl)benzene ($\mathbf{A}^{2+}$), 2,2'-(1,4-phenylene)bis(1,4,5,6-tetrahydropyrimidinium-5-ol) ($\mathbf{B}^{2+}$) and 1,4-bis(1-methyl-1,4,5,6-tetrahydropyrimidinium-2-yl)benzene ($\mathbf{C}^{2+}$), (see Figure 6.1) are presented and compared with two [MnCr] oxalate-based synthesized by Coronado *et al.*, one hexacoordinated [310] and other heptacoordinated[302]. The obtained compounds present all the same Mn/Cr ratio as well as an

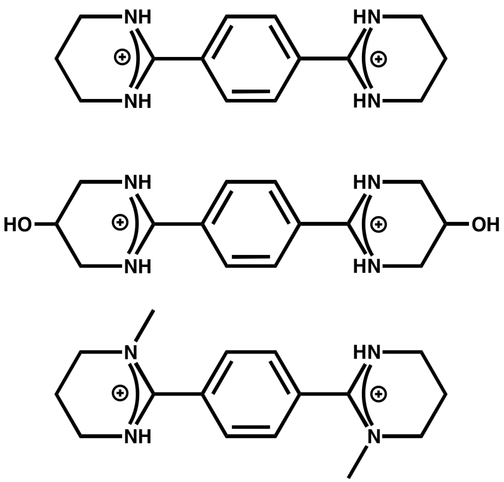

Figure 6.1: Amidinium-based dications templating the formation of the oxalate-based compounds. $\mathbf{A}^{2+}$ (top), $\mathbf{B}^{2+}$ (middle) and $\mathbf{C}^{2+}$ (bottom).

analogous coordination sphere around the Mn(II) centre, with the following formula $X[Mn^{II}(CH_3OH)Cr^{III}(ox)_3]_2 \cdot nS$ ($X^{2+} = C_{14}N_4H_{20}{}^{2+}$ (**1**), $C_{14}O_2N_4H_{20}{}^{2+}$ (**2**), $C_{16}N_4H_{24}{}^{2+}$ (**3**); n=4 (**1-2**), 2 (**3**); S= CH3OH (**1-2**), CH3CN (**3**)). The structural data will be used as a solid basis to perform a thorough *ab initio* theoretical study to establish a possible magneto-structural correlation between the geometry of the oxalate bridge and the exchange interaction between the metallic centres.

6.2 Computational Details

For each compound, four different Mn(μ-ox)Cr pairs were considered, the **1**, **2** and **3** using the anionic units represented in Fig. 1 and the **4** and **5** corresponding to the anionic unit presented in the refs. [302] and [310], respectively. The geometrical parameters extracted from the different crystal structures were applied without performing any further geometry optimization.

The presence of five unpaired electrons on high-spin Mn(II) and three on the Cr(III) ion leads to a 8-electron 8-orbital active space, denoted as CAS(8,8). The orbitals and configuration expansion coefficients of the S = 1, 2, 3 and 4 wave functions were optimized at CASSCF level to minimize the energy for all twelve units. In addition, CASPT2 calculations has been done to check the robustness of the spin Hamiltonian picture. The deviation per state can be evaluated using the following error expression:

$$\epsilon = \frac{100 \times \sum_i^N |E_i^{AI} - E_i^M|}{N \times \Delta E^{AI}} \tag{6.1}$$

where N is the number of states described by the Hamiltonian, E^{AI} are the *ab initio* energies and E^M are the model energies of the state i, and ΔE^{AI} the *ab initio* energy differences between the lowest and excited spin-states.

It has been clearly demonstrated that a bare valence-only description is not sufficient to grasp energy differences in spin-coupled systems [311–314]. Thus, dynamic electron correlation contributions were then incorporated using the variational methodology, the CAS+S and the difference dedicated configuration interaction (DDCI) method, implemented in the CASDI code [150, 315]. The DDCI approach aims at hierarchizing different states, which share similar spatial descriptions. Therefore, one has to choose a common set of MOs to build up the CI space. The CAS(8,8)SCF nanuplet MOs were used throughout the spin states energies evaluation. The CAS(8,8)SCF wave function is used as reference and depending on the number of holes created in the doubly occupied (inactive) and particles created in the empty (virtual) orbitals, the resulting CI space can be labelled as DDCI-1, DDCI-2 and DDCI-3 [119].

The results presented here all refer to CAS+S and DDCI-2. Given the large number of determinants in the reference wave function, the straightforward application of the DDCI approach leads to an unmanageably large wave function expansion. Therefore, we have followed two different approaches to keep the calculation tractable. In the first place, the delocalized molecular orbitals of the S=4 state were transformed to a set of localized orbitals, which can be classified by there shape as core orbitals, σ, σ^*-orbitals, π, π^*-orbitals, etc. This procedure allows us to split the system following a valence bond-like picture, staying in an orthogonal framework. The method has proven to be extremely efficient not only to reduce in a rational way the number of inactive and virtual MOs in post CASSCF treatments but also to analyse the relevance of chemical regions in energy differences [314]. The procedure is particularly attractive in exchange coupling constants calculations since one

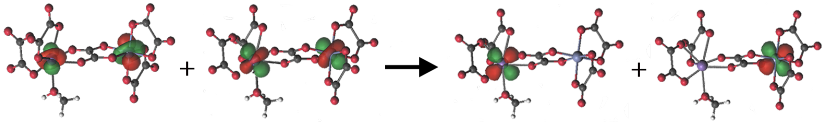

Figure 6.2: Example of localization procedure. The molecular orbitals (MOs) on the *left* is non-localized (a mixture of the MOs of the 2 metal centres) and the MOs of the *right* are the localized after DOLO program procedure.

can concentrate the numerical efforts according the polarizable nature of the different fragments. The DOLO program (implemented in CASDI code) was used to perform the localization procedure. The second, complementary reduction step consists in eliminating all the deadwood configurations from the reference wave function. For this purpose, we only kept the neutral (Cr^{3+}–Mn^{2+}) and ionic (Cr^{4+}–Mn^{+} and Cr^{2+}–Mn^{3+}) configurations, while all the di- and tri-ionic configurations were eliminated from the CASSCF wave function [109]. This classification of the configurations in the CAS wave function can only be made when the active orbitals are localized on the magnetic centres as shown in Figure 6.2.

Extended basis sets were used for the metal centres and nearest-neighbour oxygen atoms, namely ANO-RCC 5s4p2d1f and 3s2p1d. The other oxygen and carbon atoms were described with ANO-RCC 2s1p, while the H atoms were assigned a 2s basis set. All our calculations were performed using the MOLCAS 7.4 suite of program [166, 167] and subsequent CASDI chain [150].

6.3 Results and Discussion

Quantum chemistry calculations were performed to explore the nature and magnitude of the exchange interactions for the different Mn(μ-ox)Cr pairs of the heptacoordinated compounds **1-4** and the hexacoordinated compound **5** (Figure 6.3). Considering that these pair interactions are not accessible independently from the experiment, the theoretical exploration should complement the magnetic measurements and finely stress the influence of the characteristics of the Mn(II) coordination sphere and of the oxalate bridge on the exchange interaction parameters. Our goal is to quantify the possible deviation between the three constants within a given compound and to look for a trend in the series of compounds.

The Robustness of the Spin Hamiltonian

The first step of the study was to check the robustness of the Heisenberg spin Hamiltonian ($\hat{H} = -2J \cdot \hat{S}_1\hat{S}_2$) with the multiconfigurational CASSCF. Previous studies have demonstrated that CASSCF energy differences usually provide a good approximation to the experimental spin state ordering but it is also demonstrated that the values of the magnetic coupling constants are normally too small [316, 317]. The active space used for the study is the minimal one, with 8 electrons and 8 orbitals (Mn-3d^5 and Cr-3d^3). Table 6.1 shows the energy values obtained for the different spin states of one of the dimers of compounds **1-4**. The energies are regularly

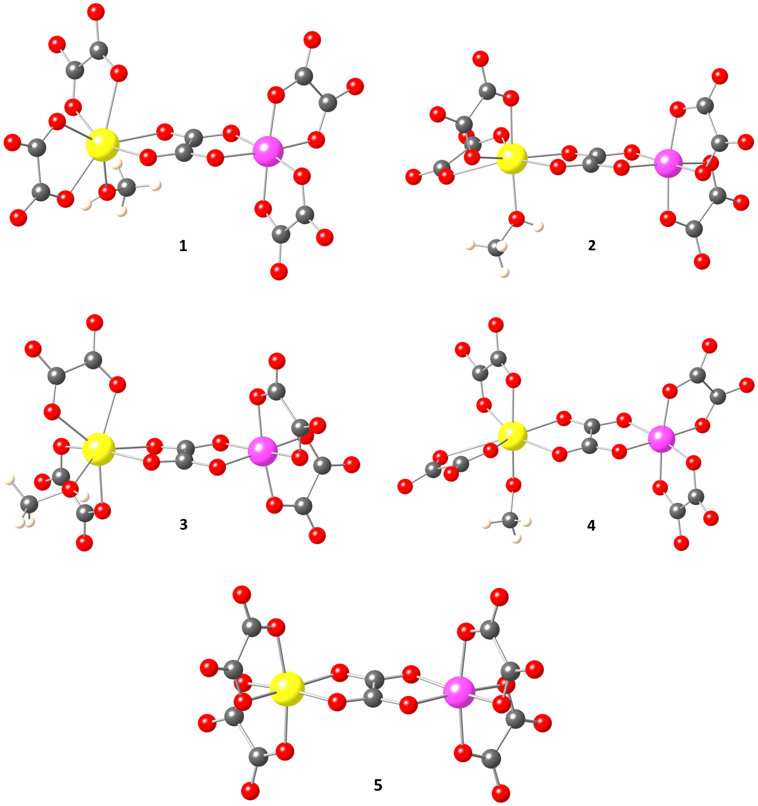

Figure 6.3: Estructures extracted from the X-ray crystal structures. The experimental J values of the different heptacoordinated complexes: (**1**) 4.46 K, (**2**) 5.70 K, (**3**) 5.70 K and (**4**) -9.90 K [302]. The hexacoordinated complex (**5**) with an approx. experimental J value of 5.61 K [310].

Table 6.1: CAS(8,8)SCF energies (in K) of the different spin states calculated for one of the Mn–Cr pairs for compounds **1-4**. The nanuplet S=4 energy has been chosen as reference.

	1	**2**	**3**	**4**
S=4	0.00	0.00	0.00	0.00
S=3	1.04	0.77	0.70	0.84
S=2	1.63	1.17	1.04	1.27
S=1	1.93	1.35	1.19	1.49
J	0.10	0.07	0.06	0.08
J_{biquad}	0.08	0.05	0.04	0.05
λ	-0.009	-0.008	-0.007	-0.008
J_{exp}	0.61	0.42	0.54	-0.94
ε (%)	4.59	4.30	4.22	4.54
ε_{biquad} (%)	0.27	0.19	0.62	0.45

spaced at first sight, but a careful inspection reveals a 5% deviation from the strict Heisenberg behaviour. Extending the Hamiltonian with a term for the biquadratic exchange ($\lambda(\hat{S}_1\hat{S}_2)^2$) reduces the deviation to less than 1% although is very small ($\lambda_{max} = 0.01$ K). However, more importantly, we also confirm that the values of J are much too small to use CASSCF as method to compare with experiment.

In a first attempt to improve the CASSCF results, we add a second-order perturbation theory correction by means of CASPT2 . The results obtained at this level of calculation are summarized in Table 6.2. It is immediately seen that CASPT2 completely changes the

Table 6.2: Energies (in K) of the different spin states and geometries calculated at the CAS[8,8]SCF/CASPT2 level. The nanoplet S=4 energy has been chosen as reference. The J values have been calculated from the nanoplet-heptet energy difference.

	1	**2**	**3**	**4**
S=4	0.00	0.00	0.00	0.00
S=3	11.2	10.1	10.3	10.3
S=2	5.6	3.6	4.1	4.4
S=1	-5.4	-7.4	-7.0	-6.6
J	1.39	1.27	1.29	1.29
J_{exp}	0.61	0.42	0.54	-0.94

results. The methodology fails on the ordering of the spin states in all four compounds and predicts a triplet ground state instead of expected nanuplet. Moreover, the spacing between the levels is so irregular that even the mapping on a model Hamiltonian including biquadratic exchange is impossible. This erroneous behaviour of CASPT2 was observed before for a μ-oxalato Cr–Ni dimer [110]. It was concluded that reasonable J values can be obtained from the energy difference of the S_{max} and S_{max-1} states for ferromagnetically coupled spin moments. The so-obtained J-values compare reasonably well with experiment for **1-3**, and anticipates ferromagnetic coupling in **4** as well, contrary to what was suggested by the experiments.

In conclusion, the combination of CASSCF and CASPT2, very successful in a wide range of applications, does not give the desired accuracy to study the magnetic coupling of the Mn–Cr pairs in the considered compounds. Therefore, we explore the performance of other computational schemes in the next sections in order to improve the reliability of the values obtained.

From Multiconfigurational to Variational

Since the perturbational treatment of the dynamic electron correlation introduces numerical artefacts, we now switch to variational approaches. The intrinsic multideterminantal nature of the spin states enforces us to stay within the multireference family of methods, and among the many schemes available, we start with the most simple one, namely the so-called CAS+S (or DDCI-1) method. This method is known to systematically underestimate the strength of the magnetic coupling but it enables us to check whether the regular spacing found with CASSCF is maintained when electron correlation is included. It has been reported in the literature that electron correlation can lower the relative energy of the so-called non-Hund states, responsible for deviations to the regular Heisenberg spacings [318]. The relatively low cost of the CAS+S calculations allows us calculate all the spin states from nanuplet to triplet, so that the robustness of the Hamiltonian can be estimated.

To reach qualitative convergence on the calculated J-values, we elevate the computational level to DDCI-2, while some tests are also done with the full DDCI method (see Chapter 2: Methodology for the details). Since the computational cost increases rapidly for these schemes, we have adopted the usual procedures to restrict the wave function expansion to the most determinants only. In the first place, we have transformed the canonical CASSCF orbitals to a set of localized orbitals following the procedure outline in Chapter 2. The resulting orbitals not belonging to the CAS are classified by their character as core, σ, π, σ^*, π^*, metal-4d and diffuse. Thereafter we define five orbital spaces; frozen, inactive, active, virtual and deleted, where the orbitals in the first and the last spaces are excluded from the electron correlation treatment. The localized orbitals are distributed in four selections over these five spaces as detailed in Table 6.3. The second, complementary reduction step consists in eliminating all the deadwood configurations from the reference wave function. For this purpose, we only kept the neutral (Cr^{3+}-Mn^{2+}) and ionic (Cr^{4+}-Mn^{+} and Cr^{2+}-Mn^{3+}) configurations, while all the di- and tri-ionic configurations were eliminated from the CASSCF wave function [110]. This classification of the configurations in the CAS wave function can only be made when the active orbitals are localized on the magnetic centres as shown in Figure 6.2. The resulting wave functions are labeled as SEL+DDCI2 and SEL+DDCI, respectively.

Table 6.4 shows that the number of determinants is enormously reduced when the reference wave function is restricted to the neutral determinants only; comparing SEL+DDCI and CAS+DDCI we observe a reduction by a factor of 6. Furthermore, we see a steady increase of the number of determinants with the size of the

Table 6.3: The four selections of MOs over the five orbital spaces. A, B, C and D sets will be used after.

	A	B	C	D
Frozen	100 (core+σ)	100 (core+σ)	50 (core)	50 (core)
Inactive	42 (π)	42 (π)	92 (π+σ)	104 (π+σ)
Active	8 (d-M)	8 (d-M)	8 (d-M)	8 (d-M)
Virtuals	30 (d'+π^*)	52 (d'+π^*+σ^*)	52 (d'+π^*+σ^*)	203
Deleted	173	151	151	0

MO space considered in the generation of the CI expansion and that SEL+DDCI-2 is more than an order of magnitude cheaper than SEL+DDCI. Concerning the magnetic coupling constants, we can see that increasing the MO space has a minor effect on the J-values calculated with CAS+S. For SEL+DDCI, we do observe a modest increase. The anomalously large constant calculated with CAS+DDCI (5.77 K) is due to the appearance of intruder states and could in theory be solved by adding the quintet root to the calculation. This can, however, only be done by decreasing the M_S value of the determinants, which increases the number of determinants to such extent that the calculation becomes practically impossible. Therefore, no further attempts have been made to perform full CAS+DDCI calculations. Finally, we conclude that SEL+DDCI-2 provides us with a relatively cheap computational scheme to investigate the three different magnetic couplings in the four compounds, although we should keep in mind that the value may be slightly underestimated when making the comparison with experiment.

Table 6.4: Number of determinants (in millions) in the wave functions $|S, M_S >= |4,3>$ and $|3,3>$ for different CI expansions and calculated J-values (in K) for one of the Mn–Cr pairs in compound **4**. The A, B, C, and D are the MOs selections showed in Table 6.3.

	A	B	C	D
CAS+S	1.1	2.0	4.2	17.2
SEL+DDCI-2			3.6	
SEL+DDCI	17.0	38.0	126.5	
CAS+DDCI	102.3			
CAS+S	0.08	0.08	0.16	0.27
SEL+DDCI-2			0.35	
SEL+DDCI	0.43	0.54	0.95	
CAS+DDCI	5.77			

The question to what extent the Heisenberg behaviour is maintained when electron correlation is taken into account is answered in Table 6.5 and graphically represented in Figure 6.4. There we report the CAS+S energies of the four spin states calculated with MO distribution A (see Table 6.3) for the same dimers as the ones used in the CASSCF/CASPT2 calculations. The values are similar than the ones reported in Table 6.1 for CASSCF, they increase with the use of the MO distribution D (compare compound **4** in Table 6.4 and 6.5). Nevertheless, the calculation of the S=1, 2, 3 and 4 eigenvalues calls for an unaffordable number of determinants. In addition, we see that the Heisenberg behaviour is strictly maintained, the calculated deviations are less than 1%. A fitting with a biquadratic term in the Hamiltonian leads to negligibly small λ values (λ_{max} = 0.001 K). The wave function analysis of Bastardis

Table 6.5: Energies (in K) of the different spin states and geometries calculated at the CAS+S level. The selection used is A in Table 6.3. The nanuplet S=4 energy has been chosen as reference.

	1	**2**	**3**	**4**
S=4	0.00	0.00	0.00	0.00
S=3	0.64	0.84	0.77	0.66
S=2	1.11	1.44	1.30	1.12
S=1	1.44	1.89	1.71	1.47
J value	0.08	0.11	0.10	0.08
J_{exp}	0.61	0.42	0.54	-0.94
ε (%)	0.16	0.94	1.03	1.03

and co-workers for a Ni-dimer showed that CAS+S has all the necessary ingredients to describe non-Heisenberg behaviour [318], and hence, we conclude that for the present compounds the role of the non-Hund states is small enough to be neglected. In consequence, the energy difference between the S=4 and S=3 (see Table 6.4) can be used to construct the whole Heisenberg spectrum and from now on we will only consider these two spin states as they are computationally less demanding.

DDCI-2 to Complement the Experimental Values

Table 6.6 lists the CAS[8,8] + DDCI-2 calculations and exchange coupling constants performed on the three spin state energy differences (S=1,2,3 and 4, resulting from the S_{MnII} = 5/2 and S_{CrIII}

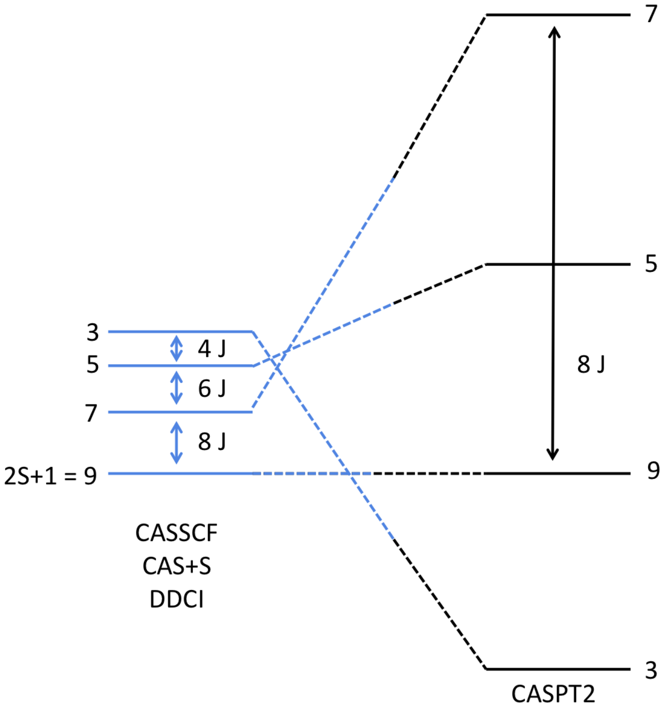

Figure 6.4: Graphical representation of the magnetic ordering of the different spin-states depending on the methodology.

= 3/2 coupling). First, we observed that the latter follow the expected Heisenberg behaviour $E(S-1) - E(S) = J\Delta S$ with deviations smaller than 1.5%. Therefore, the description of the magnetic properties of each individual pair by means of a Heisenberg Hamiltonian is fully justified. Let us stress that important deviations to Heisenberg picture have been observed and rationalized for $S >$ 1/2 spin-coupled systems [119, 319, 320]. Then, the calculated values are all positive, a reflection of the ferromagnetic behaviour in all considered pairs. This observation is somewhat puzzling since an antiferromagnetic behaviour was reported in compound **4**.

Let us therefore further analyse the results obtained for the three types of bridges. The calculated values are referred to as J_1, J_2 and J_3. The asymmetry in the two Mn-O(ox) distances is largest in the dimer associated with J_1 (see Table 6.6). Despite the relatively small amplitude of the exchange coupling constants, one can observe a general trend favouring a smaller J_1 value for a larger asymmetry character. This is most pronounced when compounds **1**, **2**, **3** are compared to compound **4**. Indeed, the nearly monodentate coordination in **4** leads to a very weak J_1 value that, however, is suggestive of ferromagnetic behaviour. Hence, we can confirm on the importance of the asymmetry of the Mn-oxalate coordination on the magnetic coupling. Accordingly, J_2 and J_3 exhibit comparable amplitudes in all four complexes, and so are all the Mn-O(ox) distances (see Table 6.6). Finally, in order to address the influence of the methanol coordination on the coupling, we have evaluated the magnetic coupling in a related Mn(μ-ox)Cr compound synthesized without the presence of methanol (*i.e.*, hexacoordinated Mn

Table 6.6: J values (in K) of the different Mn-Cr pair (**1-4**) calculated at the CAS[8,8] + DDCI-2 level. Mn-O(ox) distances (Å) are given in parenthesis.

	1	**2**	**3**	**4**
J_1	0.27 (2.17-2.46)	0.21 (2.19-2.39)	0.26 (2.19-2.51)	0.08 (2.16-2.81)
J_2	0.24 (2.20-2.27)	0.38 (2.27-2.28)	0.28 (2.25-2.35)	0.43 (2.18-2.22)
J_3	0.46 (2.22-2.30)	0.45 (2.20-2.28)	0.29 (2.22-2.25)	0.53 (2.26-2.30)
J_{avg}	0.32	0.35	0.28	0.35

ion). The resulting magnetic units show nearly regular octahedral coordination spheres around Mn and Cr. The calculated exchange coupling constants are between 0.4-0.8 K for the three different pathways, in line but slightly larger to those listed in Table 6.6. This increase can be related to average Mn-O distances about 0.2 Å smaller than in compounds where manganese(II) is heptacoordinated.

From our calculations, it appears that the asymmetry of the bridge does have an influence on the magnetic coupling but does not provide a clear-cut explanation in the nature and amplitude of the experimental observations (see Table 6.11). The calculated and experimental exchange interaction parameters have the same magnitude but the contributions of J_2 and J_3 blurs out the small differences

Table 6.7: Average energies (in K) of the different spin states and geometries calculated at the CAS[8,8] + DDCI-2 level. The nanuplet S=4 energy has been chosen as reference.

	1	**2**	**3**	**4**	**5**
S=4	0.00	0.00	0.00	0.00	0.00
S=3	2.59	2.78	2.24	2.81	5.14
S=2	4.47	4.81	3.88	4.84	8.95
S=1	5.80	6.23	5.02	6.27	11.54
J_{avg}	0.32	0.35	0.28	0.35	0.64
ε (%)	1.40	1.26	0.85	1.35	0.91

observed on J_1. One may question the procedure that consists in averaging over the three pathways (see Figure 6.5), positive values J_1, J_2 and J_3 suggesting a ferromagnetic behaviour in all **1-4** compounds. Thus, one may use a different strategy to make contact with experimental observations. Setting the S=2 energy to zero as a reference for all three pairs, one can average the three energies of spin states. Evidently, no dramatic change is expected as a consequence of the robustness of the Heisenberg picture. Nevertheless, this strategy follows the idea of having a single exchange interaction that reflects the occupations of averaged spin states. The calculated energies are given in Table 6.7, and as expected, a ferromagnetic behaviour is preserved in all compounds. It should be noted that the reverse problem was observed for DFT calculations performed on trinuclear oxalate-bridged complexes [300].

This is indicative that the pair model where only the coordination

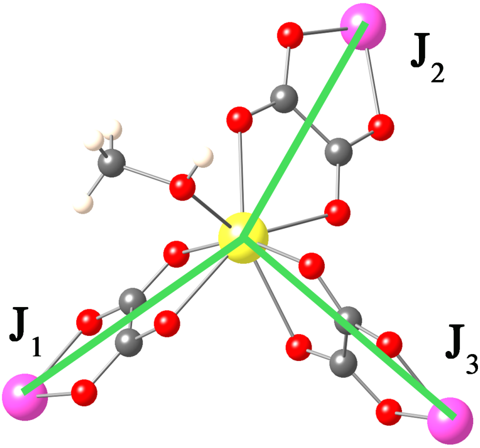

Figure 6.5: Schematic representation of the 3 different magnetic pathways in the hexagonal layers formed by the anionic units.

bonds between the two metal centers are considered, which is the basis of most exchange parameter analysis in molecular magnetism, may not capture all the physical effects in extended materials. In turn, charge repartition [158, 321], H-bonding [322] and/or magnetic anisotropy should play a crucial role all the more that the observed coupling constants have a modest magnitudes. Thus, the latter parameter is explored in the four compounds by calculating the zero-field splitting (ZFS) parameters for the Cr(III) and Mn(II) centers (Table 6.8) following the strategy described in Ref. 40 [111]. In all cases, only a non-negligible axial anisotropy (D) appears, the rhombic anisotropy (E) being very small. Provided that the isotropic coupling between Cr(III) and Mn(II) dominates over the single ion anisotropy, the sublevels of the S=4 state can be described with an effective zero-field Hamiltonian $S \cdot D(eff) \cdot S$ [1], where $D(eff)$ is $(3/28)D_{\mathrm{Cr}} + (5/14)D_{\mathrm{Mn}}$ = -0.29 K. The S=3 state lies at $8J$ and the effective axial anisotropy becomes -0.14 K for this state. This means that the manifold of M_S sublevels of this spin state overlaps with the manifold of the S=4 state, and hence, the strong exchange assumption is probably not valid. It is important to point out the need of including the virtual orbitals to get a proper description of the anisotropy, especially on the Mn ion. The inclusion of an effective core potential does not change the values obtained. Needless to say that the anisotropy of the Mn ion completely disappears in the compound without methanol (**5**). This increases enormously the difficulty of the theoretical analysis of the magnetic properties as was shown by Maurice *et al.* in a study of a Ni dimer in the weak exchange limit [112]. In that complex, it was also found that the isotropic coupling (ferromagnetic in nature) extracted from very precise *ab initio* calculations was slightly smaller than the one estimated from experimental data, exactly as in the present case. Concerning complex **4**, we tentatively assign the disagreement between theory (ferromagnetic isotropic coupling) and experiment (antiferromagnetic isotropic coupling) to the weak exchange regime, which makes the fitting of the magnetic susceptibility a delicate question.

The calculated and experimental exchange interaction parameters (Table 6.9) have the same magnitude. Nevertheless, within the calculations, all the exchange interaction parameters remain ferromagnetic even for the most extreme asymmetry of the bridge (J_3 (**4**) in Table 6.9). The values obtained, especially for compound

Table 6.8: Calculated zero field splitting parameters *D* (axial) and *E* (rhombic) parameters (in K) of the Cr and Mn centers in the compounds **1-4**.

	1		**2**		**3**		**4**	
CAS[n,m]	D	E	D	E	D	E	D	E
Cr								
[3,5]	-0.96	0.04	-0.87	0.10	-0.64	0.04	-0.88	0.04
[3,10]	-0.95	0.04	-0.87	0.10	-0.64	0.04	-0.88	0.04
[3,10] + ECP	-0.97	0.04	-0.88	0.10	-0.67	0.05	-0.91	0.05
Mn								
[5,5]	-0.11	0.01	0.09	0.00	-0.10	0.03	-0.10	0.03
[5,10]	-0.53	0.07	-0.54	0.05	-0.41	0.06	-0.27	0.12
[5,10] + ECP	-0.50	0.08	-0.53	0.07	-0.41	0.05	-0.30	0.04
J_{avg}	0.32		0.35		0.28		0.35	

Table 6.9: Experimental and theoretical J values (in K) of the different Mn-Cr pairs. The experimental J value of **4** and **5** were extracted from refs. [302, 310].

	1	**2**	**3**	**4**	**5**
J_{theo}	0.32	0.35	0.28	0.35	0.64
J_{exp}	0.61	0.42	0.54	-0.94	0.54

4, contrast with the experimental result found by Coronado and co-workers [302]. On the contrary, the calculated value for the hexacoordinated compound **5** is in agreement with the experimental value found by Coronado and co-workers in a previous work [310].

6.4 Conclusions

The purpouse of this work was to complement the experimental findings using computational tools. Accurate predictions of the coupling constants between MnCr magnetic centers have been obtained from the variational DDCI-2 methodology. The magnetic properties of the bimetallic MnCr-oxalate complexes do not suffer important changes from the hexacoordinated to the heptacoordinated environment as was suggested in previous studies [302]. The values of the magnetic coupling constant remain ferromagnetic ($J > 0$) and no clear relations with the distortions have been found. Moreover, the zero-field splitting (ZFS) parameters have been calculated for the single ions of Cr(III) and Mn(II). The rhombic anisotropy is small. In contrast, a non-negligible values were found for the axial anisotropy, concluding that the strong exchange limit is possibly not valid due to the mixture between the sublevels of the S=3 and S=4 electronic states.

In addition, a more theoretical exploration has been undertaken. First, to check the robustness (see Fig. 6.4) of the spin Hamiltonian with the different methodologies, being the variational methods the best candidates to accomplish the relationship between the spin-state energies and the J values predicted by the Heisenberg Hamiltonian. CASSCF also satisfies these energy spacings in contrast with CASPT2, which provides an erroneous ordering. Secondly, we have selected a variatonal method to include electron correlation with the best accuracy/computational cost. It is demonstrated that DDCI-2 is a good alternative to the expensive DDCI methodology.

6.5 Experimental Part by C. Maxim, S. Ferlay and C. Train

Synthesis

$MnCl_2 \cdot 4H_2O$ was purchased from commercial sources and used as received. $(NH_4)_3[Cr(ox)_3] \cdot 3H_2O$ [304–306], $\mathbf{A}Cl_2$ [323], $\mathbf{B}Cl_2$ [323] and $\mathbf{C}Cl_2$ [324], (Figure 6.1) were prepared following the published procedures.

$\mathbf{A[Mn^{II}(CH_3OH)Cr^{III}(ox)_3]_2 \cdot 4CH_3OH}$ (1)

$(NH_4)_3[Cr(ox)_3] \cdot 3H_2O$ (85.6 mg, 0.2 mmol) and $MnCl_2 \cdot 4H_2O$ (40 mg, 0.2 mmol) in 8 mL methanol was introduced in a 1.5 cm diameter tube and layered with 15 mL CH_3OH. A methanolic solution (3mL) containing $\mathbf{A}Cl_2$ (25 mg, 0.1 mmol) was then layered. After 2-3 days, violet crystals were formed at the interface. Elemental analysis calculated (%) for $C_{32}H_{44}Cr_2Mn_2N_4O_{30}$ (1178.6): C 32.61, H 3.76, N 4.75; found: C 31.58, H 3.36, N 4.28; IR: $\nu = 3457$ (O–H), 3124 (N–H), 3035 and 2990 (C–H), 1701, 1659, 1640 cm^{-1} (C–O).

$\mathbf{B[Mn^{II}(CH_3OH)Cr^{III}(ox)_3]_2 \cdot 4CH_3OH}$ (2)

$(NH_4)_3[Cr(ox)_3] \cdot 3H_2O$ (85.6 mg, 0.2 mmol) and $MnCl_2 \cdot 4H_2O$ (40 mg, 0.2 mmol) in 8 mL methanol was introduced in a 1.5 cm diameter tube and layered with 12 mL CH_3OH. A methanolic solution (4mL) containing $\mathbf{B}Cl_2$ (20 mg, 0.1 mmol) was then layered. After

3 days, violet crystals were formed at the interface. Elemental analysis calculated (%) for $C_{32}H_{44}Cr_2Mn_2N_4O_{32}$ (1210.65): C 31.74, H 3.66, N 4.62; found: C 31.18, H 3.24, N 4.32; IR: ν = 3459 (O–H), 3120 (N–H), 3025 and 2989 (C–H), 1702, 1657, 1639 cm^{-1} (C–O).

$\mathbf{C[Mn^{II}(CH_3OH)Cr^{III}(ox)_3]_2 \cdot 2CH_3CN}$ (3)

Compound 3 was obtained as violet crystals by slow evaporation at room temperature (1 day) of an solvent mixture solution (5 mL $CH_3OH/CH_3CN/H_2O$ 4:4:1) containing $(NH_4)_3[Cr(ox)_3]\cdot 3H_2O$ (52.5 mg, 0.125 mmol), $MnCl_2\cdot 4H_2O$ (25 mg, 0.125 mmol) and **C**Cl_2 (27 mg, 0.063 mmol). Elemental analysis calculated (%) for $C_{34}H_{38}Cr_2Mn_2N_6O_{26}$ (1260.55): C 35.18, H 3.30, N 7.24; found: C 35.05, H 3.18, N 7.14; IR: ν = 3447 (O–H), 3114 (N–H), 3015 and 2988 (C–H), 1703, 1649, 1638 cm^{-1} (C–O).

Characterization Techniques

FT-IR spectra were recorded on a Perkin Elmer ATR spectrometer. Microanalyses were performed by the shared Elemental Analysis Service at Université de Strasbourg. TGA measurements have been performed on polycrystalline compounds on Pyris 6 TGA Lab System (Perkin-Elmer), using a N_2 flow of 20 mL/mn and a heat rate of 4°C/mn. Variable temperature (2.0-300K) magnetic susceptibility measurements were carried out on polycrystalline samples with a MPMS SQUID magnetometer by applying a 1000G external magnetic field.

Structural Studies

Single-Crystal Studies

Data were collected at 173(2) K on a Bruker APEX8 CCD Diffractometer (compound **2** and **3**) equipped with an Oxford Cryosystem liquid N_2 device, using graphite-monochromated Mo-Kα (λ = 0.71073) radiation and on Xcalibur E Diffractometer (compound **1**) using Cu-Kα (λ = 1.54184) radiation. The structures were solved by direct methods and refined by full-matrix least squares techniques based on F^2. The non-H atoms were refined with anisotropic displacement parameters. Calculations were performed using SHELX-2013 crystallographic software package. All hydrogen atoms were generated geometrically [325]. For compound 2 the noncoordinated methanol molecules are highly disordered which could not be located successfully from Fourier maps in the refinement cycles. The scattering from the highly disordered lattice guest molecules were removed using the SQUEEZE procedure implemented in the PLATON package [326]. Moreover, the coordinated methanol molecules are disordered over two positions, with a ratio refined at 0.67:0.33. CCDC 1448152-1448154 contain supplementary crystallographic data for the three compounds. They can be obtained free of charge from the Cambridge Crystallographic Data Centre via www.ccdc.cam.ac.uk/datarequest/cif.

Powder Diffraction Studies (PXRD)

Diagrams were collected on a Bruker D8 diffractometer using monochromatic Cu-Kα radiation with a scanning range between 4 and 40° using a scan step size of 8°/mn. As already demonstrated and currently admitted, for all compounds, discrepancies in intensity between the observed and simulated patterns are due to preferential orientations of the microcrystalline powders.

Results and Discussion

Synthesis

Compounds **1** and **2** were obtained as crystalline materials by slow evaporation at room temperature of a methanolic solution containing tris(oxalato)chromate(III) and manganese(II) chloride and the chloride salt of the template cation (A^{2+} and B^{2+}). Compound **3** was obtained following the same procedure (with C^{2+}), but using a $CH_3OH/CH_3CN/H_2O$ mixture. For the three compounds, PXRD (Fig. 6.6) and TGA measurements (Fig. 6.7) of the polycrystalline samples demonstrates that a single compound is formed during the crystallization process and that the number of solvent molecules found in the polycrystalline powder fits well with the one found by XRD. As already mentioned, in **1-3**, methanol used as solvents appears to be coordinating to Mn(II). This was previously observed in 2D oxalate-based networks when methanol or

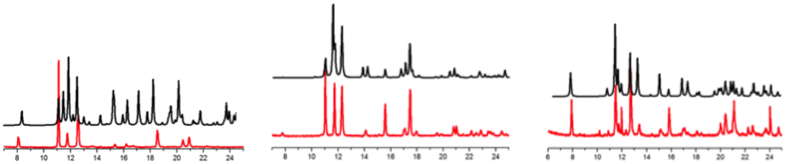

Figure 6.6: Comparison of the simulated (black) and recorded (red) PXRD patterns for **1-3** (Numbered from left to the right).

ethanol are used as solvents [301, 302]. As demonstrated below by single-crystal diffraction, the tris(oxalate)chromate(III) is preserved during the self-assembly process and the oxalate ligand act as a bisbidentate ligand. The introduction of H-bond active cations leads to numerous directional hydrogen bonds between the coordination network and the counter-ion present in the crystal. This contrasts with the "standard" oxalate-based networks [290] but was previously observed with other H-bond active cations leading to distortion of the coordination network or even to a lowering of the dimensionality of the coordination architecture [296, 301]. In the present cases, the implication of the oxygen atoms of oxalate ligands in hydrogen bonds weakens their coordination ability towards manganese(II) allowing the coordination of an extra monodentate ligand available in solution, *e.g.* a methanol molecule.

Structural Description

1 and **2** revealed to be isomorphous (monoclinic, P21/c) and also isometric (cell parameter in the same range), so

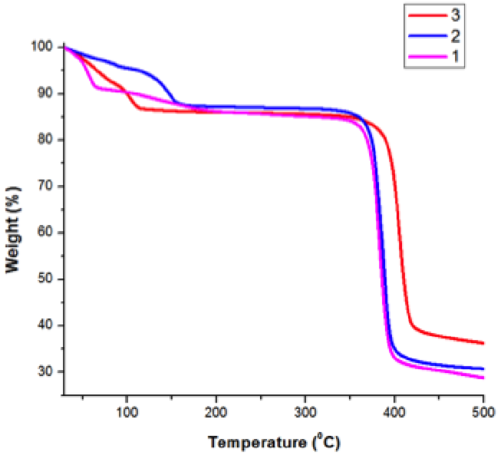

Figure 6.7: TGA Traces for **1-3**

both compounds are isostructural. **3** displays a slightly different packing. In all the compounds, the asymmetric unit is based on one half of an amidinium dication lying about an inversion centre with one anionic dimeric units $[(CH3OH)Mn^{II}(ox)Cr^{III}(ox)_2]^-$ and solvent molecules. Accordingly the formula are **A**$[Mn^{II}(CH_3OH)Cr^{III}(ox)_3]_2 \cdot 4CH_3OH$ for **1**, **B**$[Mn^{II}(CH_3OH)Cr^{III}(ox)_3]_2 \cdot 4CH_3OH$ for **2** and **C**$[Mn^{II}(CH_3OH)Cr^{III}(ox)_3]_2 \cdot 2CH_3CN$ for **3** (Figure 6.8).

Compounds **1-3** are displaying a lamellar structure where the $[(CH_3OH)Mn^{II}(ox)Cr^{III}(ox)_2]^-$ anionic units are bimetallic honeycomb pseudo-hexagonal layers, with alternating Cr(III) and Mn(II) centres, parallel to the ab plane (Figure 6.9). This is consistent with the structures observed in many bimetallic 2D oxalate-bridged sys-

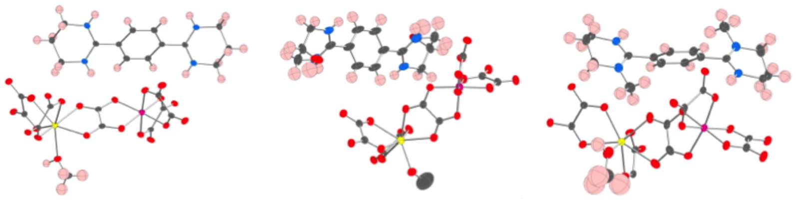

Figure 6.8: Dicationic and anionic units in compounds **1-3**.

tems [290]. In these bimetallic planes, the environment of the metal ions are comparable within the series as well as in a previously described compound of $[Mn(CH_3OH)_6][MnCr(ox)_3CH_3OH]\cdot 2CH_3OH$ [302] thereafter numbered **4**.

In all four compounds, the Cr(III) ions are in an octahedral environment with Cr-O distances in a narrow range and consistent to with the previous observations (Table 6.10). Within a given layer, all the Cr(III) helical centres present the same absolute configuration whereas, following the observed space groups, the opposite configuration is observed in the adjacent layers leading to an overall achiral structure. In contrast, the Mn(II) ions adopt an heptacoordinated environment where Mn-O distances (Table 6.10) and O–Mn–O angles undergo impressive variations compared to the idealized coordination polyedra in heptacoordination [327], *e.g.* Capped OCtahedron (COC-7), Capped Trigonal PRism (CTPR-7) and PentagonalBiPYramid (PBPY-7). Continuous Shape Measurements (CSM) thus appear as the best instrument to describe the coordination environment of the heptacoordinated manganese(II) centers. The CSM values (Table 6.10) for compounds **1-4** indicate that the closest idealized coordination polyhedron is CTPR-7 for

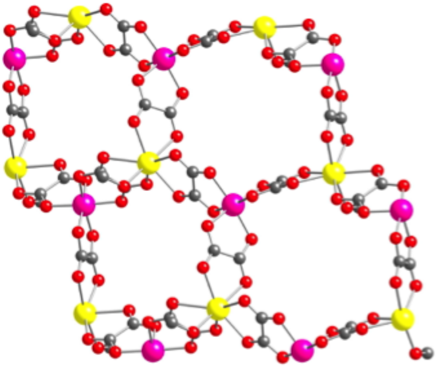

Figure 6.9: The deformed bimetallic honeycomb pseudo-hexagonal anionic system in compounds **1-3**.

the four compounds. In the case of **1** and **3**, the difference with PBPY-7 and COC-7 respectively is small, indicating that the coordination polyhedron adopt an intermediate geometry, which is also the case for compound **4**. For two of the three chelating oxalate ligands, the difference between the two Mn–O(ox) distances is in a 0-5% range leading to a rather symmetrical positioning of the ligand. The situation is dramatically different for the third oxalate ligand. In all cases, it exhibits the shortest and the longest Mn–O(oxalate) distances. The ratio between the two distances goes from 0.92 for **2** down to 0.77 for **4**. In the latter case, with a Mn–O(oxalate) long distance of 2.813 Å, the authors actually did not even consider the presence of a second coordination bond between the third oxalate ligand and the Mn(II) ion [302].

The non-octahedral environment of the Mn(II) ions induces a bend-

	1	**2**	**3**	**4**
Cr–O	1.976(3)-2.011(3)	1.967(2)-1.984(2)	1.959(4)-1.984(3)	1.954(3)-1.986(3)
Mn–O (ox)	2.176(3)-2.462(3)	2.193-2.391(2)	2.192(4)-2.513(4)	2.159(3)-2.814(3)
Mn–O (MeOH)	2.224(3)	2.256(3)	2.148(3)	2.138(3)
CSM for Mn(II)				
S(MnO_7) to COC-7	3.67	3.35	2.68	3.77
S(MnO_7) to CTPR-7	2.05	1.78	2.18	2.44
S(MnO_7) to PBPY-7	2.69	2.96	3.03	3.55
N···O (Cation)	2.817-3.074	2.905-3.275	3.252	-
O···O (MeOH)	2.853-3.009	3.084-3.179	-	-

Table 6.10: Relevant angles and distances in **1-4**. For 4, the data is extracted from refs. [302] and the CSM for Mn(II) from ref [327].

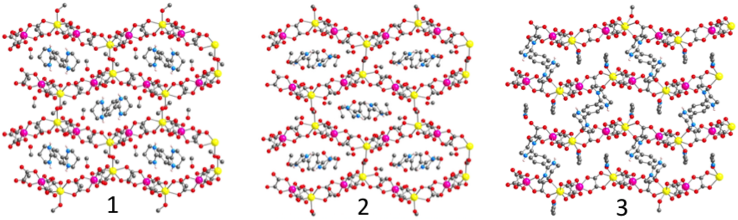

Figure 6.10: Dicationic and anionic units in compounds **1-3**.

ing of the Mn-Cr motives. Due to the presence of the inversion centres, this leads to a corrugation of the bimetallic planes. In **3**, the planes are stacked one above the other whereas in **1** and **2**, the planes are staggered, leading to the formation of "pockets" where the dications and solvent molecules are located (Figure 6.10). The dicationic units are indeed connecting the anionic layers through charge assisted N–H···O(ox) hydrogen bonding [328] between the dicationic units and the anionic layer. In **2**, the hydroxyle groups of the cations are also involved in H bonds as well as the crystallization methanol molecules. In **3**, the acetonitrile molecules are interacting with the oxygen atoms from the oxalate ligands through hydrogen bonds (Table 6.10).

Magnetic Properties

For compounds **1-3**, the thermal evolution of the χ_MT product and $\chi_M{}^{-1}$ are shown in Figure 6.11. The magnetic behaviour of the three compounds appears as very similar despite the structural changes stated above. At room temperature, the χ_MT values are

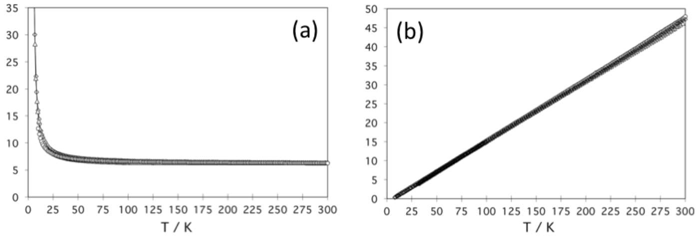

Figure 6.11: Thermal variation of the $_{\chi M}$T product (a) and the inverse magnetic susceptibility $_{\chi M}$T^{-1} (b) for compound **1** (diamonds), **2** (trinagles) and **3** (circles).

6.35 (**1**), 6.46 (**2**) and 6.28 cm^3·mol^{-1}·K (**3**). They are close to those expected for the sum of the corresponding non-interacting metal ions (6.25 cm^3 cm^3·mol^{-1}·K considering g=2.00 for both metal ions). Upon cooling, the $_{\chi M}$T product for **1-3** increases continuously. This evolution is indicative that the exchange interactions between the two metal(II) ions are dominated by ferromagnetic ones. To quantify the average interaction, the inverse susceptibility (Figure 6.11b) is fitted using a Curie-Weiss law to determine the Curie-Weiss temperatures given in Table 6.11. In a mean field approach, the Curie-Weiss temperature Θ can be related to the exchange interaction J [329]. In most cases [329, 330] a unique exchange interaction parameter in taken for a given pair of metal ions. In the present case, the structural analysis indicates that there are strong structural differences between the three oxalate bridges. It is therefore necessary to introduce three different exchange interaction parameters J_1, J_2 and J_3 for the three types of oxalate bridges present in the three compounds. The relationship between the Curie-Weiss temperature and the exchange parameters follow the next expressions (where S_i is the spin value of the metal center i):

$$\Theta = \frac{4 \cdot (J_1 + J_2 + J_3)/3 \cdot S_{Mn^{\text{II}}}(S_{Mn^{\text{II}}} + 1) S_{Cr^{\text{III}}}(S_{Cr^{\text{III}}} + 1)}{(S_{Mn^{\text{II}}}(S_{Mn^{\text{II}}} + 1) + S_{Cr^{\text{III}}}(S_{Cr^{\text{III}}} + 1))} \tag{6.2}$$

$$\Theta = \frac{4 \cdot < J > \cdot S_{Mn^{\text{II}}}(S_{Mn^{\text{II}}} + 1) S_{Cr^{\text{III}}}(S_{Cr^{\text{III}}} + 1)}{(S_{Mn^{\text{II}}}(S_{Mn^{\text{II}}} + 1) + S_{Cr^{\text{III}}}(S_{Cr^{\text{III}}} + 1))} \tag{6.3}$$

Nevertheless, as expected from a mean field approach, the Curie-Weiss temperature is proportional to the linear averaging of the three exchange parameters. In contrast with the approach proposed by Ohkoshi *et al.* on ternary Prussian Blue Analogues [330], it is not possible to go further in the present case because these compounds are made of only two independent magnetic subnetworks. The average $< J_{exp} >$ deduced from eq. 6.3 are gathered in Table 6.11. In ref. [302], the authors have tentatively related the extreme lengthening of one the Mn–O coordination bond in compound **4** with the appearance of antiferromagnetic coupling. This proposal was natural when considering the seminal work on oxalate-bridged dicopper(II) complexes where the modifications of the bridge definitely led to strong modifications of the overlap between the magnetic orbitals and, following Kahn's model, to impressive modification of the exchange interaction [331]. Nevertheless, within the presented series, this explanation does not seem to hold since compound **3** is the compound where the deformation of one of the three bridges

Table 6.11: Experimental magnetic parameters for compounds **1-4**. For **4**, the Curie-Weiss temperature is taken from Ref. [302].

	1	**2**	**3**	**4**
Θ / K	5.87	4.40	5.67	-9.90
$<J_{exp}>$ / K	0.61	0.42	0.54	-0.94

is the most severe but the weakest average exchange interaction is found for **2**. The variations of the average exchange interaction parameter do not correlate with the CSM for the manganese(II) center neither. Is the averaging of the three exchange interaction constants masking the appearance of an antiferromagnetic contribution for the most dissymmetrical bridge? A theoretical inspection where the three bridges are treated independently might be able to answer this question.

Conclusions

The synthesis of compounds **1-3** confirms the ability of anionic 2D oxalate-bridged [MnCr] networks to welcome organic dications. They are indeed the first 2D compounds where dications are inserted whereas this result was discovered in the 1990's for 3D compounds [332]. In comparison with previous cases [299, 300] the competition between coordination and hydrogen bonds did not hinder the formation of the 2D coordination network but, as already observed [297, 302], it induced the corrugation of the layers because the manganese(II) centres are heptacoordinated, while using

MeOH as solvent during the formation of the extended compounds. This phenomenon influences the magnetic exchange parameter between the metal-centres though the switch from a ferromagnetic to an antiferromagnetic interaction observed [302] in **4** was not observed experimentally nor reproduced theoretically. In the latter case, this raises fundamental questions about the phenomena that must be taken into account to fully understand the exchange interaction between two magnetic centres.

CHAPTER 7

Conclusions and Perspectives

After five intense years, we are convinced that the work done has contributed to the research field that explores the (light-induced) magnetic properties of TM complexes. All the contributions have been exposed in the chapters 3, 4, 5 and 6, where considering the growing demand for interpretation of experimental observations, the improvement of theoretical methods and the increasing of the computational resources has allowed us to deepen the understanding of magnetic beahviors of metal transitions architectures. The concluding remarks can be summarized in the following points:

∗ The density functional theory in its time-dependent variant in combination with B3LYP* accurately describes the electronic states of the different spin-states of Fe(II) and Fe(III) SCO complexes. The lower computational cost and the agreement with the CASSCF/CASPT2 methodology confirms TD-DFT/B3LYP* as an alternative to the expensive multiconfigurational methods in the study of SCO complexes.

∗ The effects of the solvent hardly affect the transition energies of symmetrical complexes (*i.e.* $[\mathrm{Fe(phen)_3}]^{2+}$), a reflection of the small dipole moment change between transiton states. In addition, the inclusion of solvent effects does not change the wavefunction of the ground state. Hence, calculations can be done in gas phase as long as the transitions do not imply large changes in the dipole moment of the complex.

∗ The combination of TD-DFT/B3LYP* and CASSCF let us extend the description of the LIESST phenomenom from

Fe(II) to Fe(III) SCO complexes. After analyzing the states involved in the process (LS, IS, HS and LMCT) and calculating the crossing rates via the Fermi's golden rule, two competing pathways for the deactivation of the excited doublet state were proposed: ^{2}LMCT→IS→HS and ^{2}LMCT→IS→LS. This competition and the small spin-orbit coupling between the ^{2}LMCT and IS states are ways to rationalize the low efficiency found in experiments.

∗ Using a biomimetic Fe(IV) model of the widely studied CPO-I and P450-I systems, we have rigorously analyzed the electronic structure and magnetic properties to provide more information to the understanding of the relation between the reactivity and the Fe–S distance of both complexes. DFT/B3LYP* calculations, complemented with CASSCF, described the system as a triradicaloid with two electrons on the Fe=O moiety, and the other one on the sulphur. In contrast with CASSCF results, let us mention that DFT/B3LYP* suggests the presence of a more delocalized picture, with contribution of over the porphyrin ring. Using localiziation tools we have found evidences that the best description of the system is a coherent with a Fe^{3+}–$O^{\bullet}$ configuration. DDCI and BS confirm the strong relation between the Fe–S distance and the strength of the ferromagnetic coupling between the spin moments of the Fe=O group and the electron on the axial ligand, while the axial anisotropy (D) remains constant.

∗ Combining experiment and DDCI calculations we have

> demonstrated that increasing the number of ligands coordinated in the Mn coordination sphere of an oxalate-based [MnCr] network from six to seven does not affect to the magnetic coupling, which remains ferromagnetic in both structures. Small deviations have been found between theory and experiment attributed to the non-negligible axial anisotropy (D). This result is in mark contrast with what had been observed in previous analogues.

All these studies were of prime importance to set up to perform a strategy to efficiently the LIESST on binuclear Fe(II) SCO complexes. We attempted the study but the preliminary results we have obtained were not as expected. Unfortunately, our insepctions fails, probably because of two factors: (i) the DFT/B3LYP* does not provide a correct ordering of the spin-states and situates the high-spin state as ground state, and (ii) the minimum active space needed to perform CASSCF/CASPT2 calculations is CAS(12,20) which is currently unaffordable.

Work is in progress to tackle these obstacles found on our path. We are currently exploring the possibilities of using a generalized active space, which permits dividing the active orbitals in an arbitrary number of subspaces, each with their own spin coupling. Furthermore, we are comparing the outcomes of the B3LYP* calculations with different quantum chemistry codes (Orca, TurboMole and Gaussian) to clarify the apparent contradiction in the results published by Zein *et al.* [90] and our first results on the same complexes. A start has been made on the exploration of the excited state potential energy surfaces, but a full description of the LIESST process would require much more time than available in the scope of this thesis.

This work is to be considered as a challenging attempt to combine DFT and wave function-based methods to examine the electronic structures of magnetic systems. We took profit of both methodologies depending on the targeted systems and properties, sometimes each one complementing the other. Our feeling is that quantum chemistry methods have reached a status of predictible tools that should be used to guide the synthesis of original architectures. Evidently, the gap between actual systems and their operating conditions (solvent, temperature, etc.) and the theoretical inspections offered by quantum chemists remains to be filled. The exponential wall of wave function methods, in particular when numerous open-shells are present, might not be jumped over by the still growing capacities of computers. Therfore, it is of prime importance to maintain the development of strategies (molecular orbitals localization, reduction of configuration interaction expansions) which will allow us to keep on the philosophy of a wave function construction. In the mean time, the impressive capabilities of DFT-based methods greatly complement the previous ones. In the future, the combination of these methodologies, a current important field, may offer new insights into *in vivo* synthetic systems while keeping spectrocopic accuracy.

Bibliography

[1] O. Kahn, in *Molecular Magnetism*, Wiley-VCH: New York, 1993, p. 396.

[2] P. Gütlich and H. A. Goodwin, *Spin crossover in Transition Metal Compounds*, Springer-Verlag, 2004, vol. 233-235.

[3] D. Gatteschi, R. Sessoli and J. Villain, in *Molecular Nanomagnets*, Oxford University Press, 2006.

[4] M. A. Halcrow, *Spin-Crossover Materials – Properties and Applications*, Wiley, Chichester, United Kingdom, 2013.

[5] M. Turnbull, T. Sugimoto and L. Thompson, in *Molecule-Based Magnetic Materials: Theory, Techniques and Applications*, American Chemical Society, 1996.

[6] D. Gatteschi and R. Sessoli, *Angew. Chem. Int. Ed.*, 2003, **42**, 268–297.

[7] A. Caneschi, D. Gatteschi, N. Lalioti, C. Sangregorio, R. Sessoli, G. Venturi, A. Vindigni, A. Rettori, M. G. Pini and M. A. Novak, *Angew. Chem. Int. Ed.*, 2001, **40**, 1760–1763.

[8] C. Coulon, R. Clérac, L. Lecren, W. Wernsdorfer and H. Miyasaka, *Phys. Rev. B*, 2004, **69**, 132408–132411.

[9] W.-X. Zhang, R. Ishikawa, B. Breedlove and M. Yamashita, *RSC Adv.*, 2013, **3**, 3772–3798.

[10] N. Ishikawa, M. Sugita, T. Ishikawa, S.-Y. Koshihara and Y. Kaizu, *J. Am. Chem. Soc.*, 2003, **125**, 8694–8695.

[11] J. M. Frost, K. L. M. Harriman and M. Murugesu, *Chem. Sci.*, 2016, **7**, 2470–2491.

[12] O. Kahn and C. J. Martinez, *Science*, 1998, **279**, 44–48.

[13] A. Bousseksou, G. Molnar, L. Salmon and W. Nicolazzi, *Chem. Soc. Rev.*, 2011, **40**, 3313–3335.

[14] E. Coronado and K. R. Dunbar, *Inorg. Chem.*, 2009, **48**, 3293–3295.

[15] A. Cannizzo, C. J. Milne, C. Consani, W. Gawelda, C. Bressler, F. van Mourik and M. Chergui, *Coord. Chem. Rev.*, 2010, **254**, 2677–2686.

[16] W. Gawelda, A. Cannizzo, V. T. Pham, F. van Mourik, C. Bressler and M. Chergui, *J. Am. Chem. Soc.*, 2007, **129**, 8199–8206.

[17] J. Tribollet, G. Galle, G. Jonusauskas, D. Deldicque, M. Tondusson, J.-F. Letard and E. Freysz, *Chem. Phys. Lett.*, 2011, **513**, 42–47.

[18] M. Cammarata, R. Bertoni, M. Lorenc, H. Cailleau, S. Di Matteo, C. Mauriac, S. F. Matar, H. Lemke, M. Chollet, S. Ravy, C. Laulhé, J.-F. Létard and E. Collet, *Phys. Rev. Lett.*, 2014, **113**, 227402–227406.

[19] G. Auböck and M. Chergui, *Nature Chem.*, 2015, **7**, 629–633.

[20] B. Rösner, M. Milek, A. Witt, B. Gobaut, P. Torelli, R. H. Fink and M. M. Khusniyarov, *Angew. Chem. Int. Ed.*, 2015, **54**, 12976–12980.

[21] A. Marino, P. Chakraborty, M. Servol, M. Lorenc, E. Collet and A. Hauser, *Angew. Chem. Int. Ed.*, 2014, **53**, 3863–3867.

[22] R. Bertoni, M. Cammarata, M. Lorenc, S. F. Matar, J.-F. Létard, H. T. Lemke and E. Collet, *Acc. Chem. Res.*, 2015, **48**, 774–781.

[23] L. A. Fredin, M. Pápai, E. Rozsályi, G. Vankó, K. Wärnmark, V. Sundström and P. Persson, *J. Phys. Chem. Lett.*, 2014, **5**, 2066–2071.

[24] R. Sessoli, D. Gatteschi, A. Caneschi and M. A. Novak, *Nature*, 1993, **365**, 141–143.

[25] A. M. Ako, I. J. Hewitt, V. Mereacre, R. Clérac, W. Wernsdorfer, C. E. Anson and A. K. Powell, *Angew. Chem. Int. Ed.*, 2006, **45**, 4875–4875.

[26] C. J. Milios, A. Vinslava, W. Wernsdorfer, S. Moggach, S. Parsons, S. P. Perlepes, G. Christou, and E. K. Brechin, *J. Am. Chem. Soc.*, 2007, **129**, 2754–2755.

[27] D. N. Woodruff, R. E. P. Winpenny and R. A. Layfield, *Chem. Rev.*, 2013, **113**, 5110–5148.

[28] R. J. Blagg, L. Ungur, F. Tuna, J. Speak, P. Comar, D. Collison, W. Wernsdorfer, E. J. L. McInnes, L. F. Chibotaru and R. E. P. Winpenny, *Nat. Chem.*, 2013, **5**, 673–678.

[29] A. Hauser, in *Spin crossover in Transition Metal Compounds II*, ed. P. Gütlich and H. A. Goodwin, Springer-Verlag, 2004, vol. 234, pp. 155–198.

[30] A. Hauser, C. Enachescu, L. M. Lawson Daku, A. Vargas and N. Amstutz, *Coord. Chem. Rev.*, 2006, **250**, 1642–1652.

[31] H. Bethe, *Naturwissenschaften*, 1927, **15**, 786–788.

[32] H. Bethe, *Annalen der Physik*, 1928, **392**, 55–129.

[33] Y. Tanabe and S. Sugano, *J. Phys. Soc. Jpn.*, 1954, **9**, 753–766.

[34] Y. Tanabe and S. Sugano, *J. Phys. Soc. Jpn.*, 1954, **9**, 766–779.

[35] Y. Tanabe and S. Sugano, *J. Phys. Soc. Jpn.*, 1956, **11**, 864–877.

[36] J. S. Griffith and L. E. Orgel, *Q. Rev. Chem. Soc.*, 1957, **11**, 381–393.

[37] M. Takano, S. Nasu, T. Abe, K. Yamamoto, S. Endo, Y. Takeda and J. B. Goodenough, *Phys. Rev. Lett.*, 1991, **67**, 3267–3270.

[38] Z. Ropka and R. J. Radwanski, *Phys. Rev. B*, 2003, **67**, 172401–172404.

[39] L. Cambi and L. Szegö, *Ber. Deutsch. Chem. Ges.*, 1931, **64**, 2591.

[40] W. A. B. Jr. and H. M. Bobonich, *Inorg. Chem.*, 1964, **3**, 1184–1188.

[41] W. A. Baker and G. J. Long, *Chem. Commun. (London)*, 1965, 368–369.

[42] E. König and K. Madeja, *Chem. Commun. (London)*, 1966, 61–62.

[43] E. König and K. Madeja, *Inorg. Chem.*, 1967, **6**, 48–55.

[44] M. Sorai and S. Seki, *J. Phys. Chem. Solids*, 1974, **35**, 555–570.

[45] E. Müller, H. Spiering and P. Gütlich, *Chem. Phys. Lett.*, 1982, **93**, 567–571.

[46] S. Decurtins, P. Gutlich, C. P. Kohler and H. Spiering, *J. Chem. Soc., Chem. Commun.*, 1985, 430–432.

[47] J.-J. Lee, H. shuenn Sheu, C.-R. Lee, J.-M. Chen, J.-F. Lee, C.-C. Wang, C.-H. Huang, and Y. Wang, *J. Am. Chem. Soc.*, 2000, **122**, 5742–5747.

[48] M. Marchivie, P. Guionneau, J. A. K. Howard, G. Chastanet, J.-F. Létard, A. E. Goeta, and D. Chasseau, *J. Am. Chem. Soc.*, 2002, **124**, 194–195.

[49] S. Mebs, B. Braun, R. Kositzki, C. Limberg and M. Haumann, *Inorg. Chem.*, 2015, **54**, 11606–11624.

[50] P. J. van Koningsbruggen, Y. Garcia, O. Kahn, L. Fournès, H. Kooijman, A. L. Spek, J. G. Haasnoot, J. Moscovici, K. Provost, A. Michalowicz, F. Renz, and P. Gütlich, *Inorg. Chem.*, 2000, **39**, 1891–1900.

[51] J. Kusz, H. Spiering and P. Gütlich, *J. Appl. Cryst.*, 2001, **34**, 229–238.

[52] J. M. Holland, J. A. McAllister, Z. Lu, C. A. Kilner, M. Thornton-Pett and M. A. Halcrow, *Chem. Commun.*, 2001, 577–578.

[53] M. Nihei, T. Shiga, Y. Maeda and H. Oshio, *Coord. Chem. Rev.*, 2007, **251**, 2606–2621.

[54] Y. Garcia and P. Gütlich, in *Spin crossover in Transition Metal Compounds II*, ed. P. Gütlich and H. A. Goodwin, Springer-Verlag, 2004, vol. 234, pp. 49–62.

[55] J.-F. Létard, L. Capes, G. Chastanet, N. Moliner, S. Létard, J.-A. Real and O. Kahn, *Chem. Phys. Lett.*, 1999, **313**, 115–120.

[56] S. Marcén, L. Lecren, L. Capes, H. Goodwin and J.-F. Létard, *Chem. Phys. Lett.*, 2002, **358**, 87–95.

[57] J. J. McGarvey and I. Lawthers, *J. Chem. Soc., Chem. Commun.*, 1982, 906–907.

[58] S. Decurtins, P. Gütlich, C. P. Köhler, H. Spiering and A. Hauser, *Chem. Phys. Lett.*, 1984, **105**, 1–4.

[59] A. Hauser, *Chem. Phys. Lett.*, 1986, **124**, 543–548.

[60] C. de Graaf and C. Sousa, *Chem. Eur. J.*, 2010, **16**, 4550–4556.

[61] C. Sousa, C. de Graaf, A. Rudavskyi, R. Broer, J. Tatchen, M. Etinski and C. M. Marian, *Chem. Eur. J.*, 2013, **19**, 17541–17551.

[62] M. Pápai, G. Vankó, C. de Graaf and T. Rozgonyi, *J. Chem. Theory Comput.*, 2013, **9**, 509–519.

[63] C. Roux, J. Zarembowitch, B. Gallois, T. Granier and R. Claude, *Inorg. Chem.*, 1994, **33**, 2273–2279.

[64] J. S. Kolb, M. D. Thomson, M. Novosel, K. Sénéchal-David, É. Rivière, M.-L. Boillot and H. G. Roskos, *C. R. Chim.*, 2007, **10**, 125–136.

[65] Y. Hasegawa, S. Kume and H. Nishihara, *Dalton Trans.*, 2009, 280–284.

[66] S. Venkataramani, U. Jana, M. Dommaschk, F. D. Sönnichsen, F. Tuczek and R. Herges, *Science*, 2011, **331**, 445–448.

[67] G. Alcover-Fortuny, C. de Graaf and R. Caballol, *Phys. Chem. Chem. Phys.*, 2015, **17**, 217–225.

[68] A. Real, J. Zarembowitch, O. Kahn and X. Solans, *Inorg. Chem.*, 1987, **26**, 2939–2943.

[69] J. A. Real, I. Castro, A. Bousseksou, M. Verdaguer, R. Burriel, M. Castro, J. Linares and F. Varret, *Inorg. Chem.*, 1997, **36**, 455–464.

[70] S. Hayami, K. Inoue and Y. Maeda, *Mol. Cryst. Liq. Cryst. Sci. Technol., Sect. A*, 1999, **335**, 573–582.

[71] J.-F. Létard, J. A. Real, N. Moliner, A. B. Gaspar, L. Capes, O. Cador, and O. Kahn, *J. Am. Chem. Soc.*, 1999, **121**, 10630–10631.

[72] A. Bousseksou, G. Molnár, J. A. Real and K. Tanaka, *Coord. Chem. Rev.*, 2007, **251**, 1822–1833.

[73] J.-F. Létard, C. Carbonera, J. A. Real, S. Kawata and S. Kaizaki, *Chem. Eur. J.*, 2009, **15**, 4146–4155.

[74] D. Papanikolaou, S. Margadonna, W. Kosaka, S. ichi Ohkoshi, M. Brunelli, and K. Prassides, *J. Am. Chem. Soc.*, 2006, **128**, 8358–8363.

[75] S.-I. Ohkoshi, K. Imoto, Y. Tsunobuchi, S. Takano and H. Tokoro, *Nat. Chem.*, 2011, **3**, 564–569.

[76] T. Matsumoto, G. N. Newton, T. Shiga, S. Hayami, Y. Matsui, H. Okamoto, R. Kumai, Y. Murakami and H. Oshio, *Nat. Commun.*, 2014, **5**, year.

[77] K. S. Murray, *Eur. J. Inorg. Chem.*, 2008, **2008**, 3101–3121.

[78] A. B. Gaspar, M. C. Munoz and J. A. Real, *J. Mater. Chem.*, 2006, **16**, 2522–2533.

[79] V. Ksenofontov, A. B. Gaspar, V. Niel, S. Reiman, J. A. Real and P. Gütlich, *Chem. Eur. J.*, 2004, **10**, 1291–1298.

[80] H. Toftlund, *Coord. Chem. Rev.*, 1989, **94**, 67–108.

[81] S. Brooker, P. G. Plieger, B. Moubaraki and K. S. Murray, *Angew. Chem. Int. Ed.*, 1999, **38**, 408–410.

[82] H. Paulsen, L. Duelund, H. Winkler, H. Toftlund and A. Trautwein, *Inorg. Chem.*, 2001, **40**, 2201–2203.

[83] M. Reiher, O. Salomon and B. Artur Hess, *Theor. Chem. Acc.*, 2001, **107**, 48–55.

[84] M. Reiher, *Inorg. Chem.*, 2002, **41**, 6928–6935.

[85] M. Swart, A. W. Ehlers and K. Lammertsma, *Mol. Phys.*, 2004, **102**, 2467–2474.

[86] M. Swart, A. R. Groenhof, A. W. Ehlers and K. Lammertsma, *J. Phys. Chem. A*, 2004, **108**, 5479–5483.

[87] K. P. Kepp, *Inorg. Chem.*, 2016, **55**, 2717–2727.

[88] B. O. Roos, P. R. Taylor and P. E. M. Siegbahn, *Chem. Phys.*, 1980, **48**, 157–173.

[89] K. Andersson, P.-A. Malmqvist and B. O. Roos, *J. Chem. Phys.*, 1992, **96**, 1218–1226.

[90] S. Zein, and S. A. Borshch, *J. Am. Chem. Soc.*, 2005, **127**, 16197–16201.

[91] B. Bleaney and K. D. Bowers, *Proc. R. Soc. Lond. A*, 1952, **214**, 451–465.

[92] D. Gatteschi, A. Caneschi, L. Pardi and R. Sessoli, *Science*, 1994, **265**, 1054–1058.

[93] T. Lis, *Acta Crystallogr. B*, 1980, **36**, 2042–2046.

[94] E. Ruiz, J. Cirera, J. Cano, S. Alvarez, C. Loose and J. Kortus, *Chem. Commun.*, 2008, 52–54.

[95] R. J. Glauber, *J. Math. Phys.*, 1963, **4**, 294–307.

[96] R. Clérac, H. Miyasaka, M. Yamashita, and C. Coulon, *J. Am. Chem. Soc.*, 2002, **124**, 12837–12844.

[97] D. E. Freedman, W. H. Harman, T. D. Harris, G. J. Long, C. J. Chang and J. R. Long, *J. Am. Chem. Soc.*, 2010, **132**, 1224–1225.

[98] M. R. Pederson and S. N. Khanna, *Phys. Rev. B*, 1999, **60**, 9566–9572.

[99] D. Ganyushin and F. Neese, *J. Chem. Phys.*, 2006, **125**, 024103–024113.

[100] D. Ganyushin and F. Neese, *J. Chem. Phys.*, 2008, **128**, 114117–114129.

[101] S. Zein and F. Neese, *J. Phys. Chem. A*, 2008, **112**, 7976–7983.

[102] J. Cirera, E. Ruiz, S. Alvarez, F. Neese and J. Kortus, *Chem. Eur. J.*, 2009, **15**, 4078–4087.

[103] F. Aquino, N. Govind and J. Autschbach, *J. Chem. Theory Comput.*, 2011, **7**, 3278–3292.

[104] F. Neese and D. A. Pantazis, *Faraday Discuss.*, 2011, **148**, 229–238.

[105] C. de Graaf, F. Illas, R. Broer and W. C. Nieuwpoort, *J. Chem. Phys.*, 1997, **106**, 3287–3291.

[106] O. Vahtras, O. Loboda, B. Minaev, H. Ågren and K. Ruud, *Chem. Phys.*, 2002, **279**, 133–142.

[107] H. Nakano, R. Uchiyama and K. Hirao, *J. Comput. Chem.*, 2002, **23**, 1166–1175.

[108] E. Bordas, R. Caballol and C. de Graaf, *J. Mol. Struct-Theochem*, 2005, **727**, 173–179.

[109] E. Bordas, R. Caballol, C. de Graaf and J.-P. Malrieu, *Chem. Phys.*, 2005, **309**, 259–269.

[110] N. Queralt, D. Taratiel, C. de Graaf, R. Caballol, R. Cimiraglia and C. Angeli, *J. Comput. Chem.*, 2008, **29**, 994–1003.

[111] R. Maurice, R. Bastardis, C. de Graaf, N. Suaud, T. Mallah and N. Guihéry, *J. Chem. Theory Comput.*, 2009, **5**, 2977–2984.

[112] R. Maurice, N. Guihéry, R. Bastardis and C. de Graaf, *J. Chem. Theory Comput.*, 2010, **6**, 55–65.

[113] R. Maurice, A. M. Pradipto, N. Guihéry, R. Broer and C. de Graaf, *J. Chem. Theory Comput.*, 2010, **6**, 3092–3101.

[114] I. Negodaev, C. de Graaf and R. Caballol, *J. Phys. Chem. A*, 2010, **114**, 7553–7560.

[115] R. Maurice, K. Sivalingam, D. Ganyushin, N. Guihéry, C. de Graaf and F. Neese, *Inorg. Chem.*, 2011, **50**, 6229–6236.

[116] L. Chibotaru and L. Ungur, *J. Chem. Phys.*, 2012, **137**, 064112–064133.

[117] R. Maurice, P. Verma, J. M. Zadrozny, S. Luo, J. Borycz, J. R. Long, D. G. Truhlar and L. Gagliardi, *Inorg. Chem.*, 2013, **52**, 9379–9389.

[118] R. Ruamps, R. Maurice, C. de Graaf and N. Guihéry, *Inorg. Chem.*, 2014, **53**, 4508–4516.

[119] J.-P. Malrieu, R. Caballol, C. J. Calzado, C. de Graaf and N. Guihéry, *Chem. Rev.*, 2014, **114**, 429–492.

[120] L. Noodleman, *J. Chem. Phys.*, 1981, **74**, 5737–5743.

[121] L. H. Thomas, *Math. Proc. Cambridge Philos. Soc.*, 1927, **23**, 542–548.

[122] E. Fermi, *Z. Phys.*, 1928, **48**, 73–79.

[123] P. A. M. Dirac, *Proc. R. Soc. Lond. A*, 1928, **117**, 610–624.

[124] F. Bloch, *Z. Phys.*, 1929, **57**, 545–555.

[125] P. A. M. Dirac, *Math. Proc. Cambridge Philos. Soc.*, 1930, **26**, 376–385.

[126] J. C. Slater, *Solid-State and Molecular Theory: A Scientific Biography*, Wiley-VCH: New York, 1975, vol. 69, pp. 320–321.

[127] P. Hohenberg and W. Kohn, *Phys. Rev.*, 1964, **136**, B864–B871.

[128] W. Kohn and L. J. Sham, *Phys. Rev.*, 1965, **140**, A1133–A1138.

[129] S. H. Vosko, L. Wilk and M. Nusair, *Can. J. Phys.*, 1980, **58**, 1200–1211.

[130] G. L. Oliver and J. P. Perdew, *Phys. Rev. A*, 1979, **20**, 397–403.

[131] J. P. Perdew, S. Kurth, A. c. v. Zupan and P. Blaha, *Phys. Rev. Lett.*, 1999, **82**, 2544–2547.

[132] O. Salomon, M. Reiher and B. A. Hess, *J. Chem. Phys.*, 2002, **117**, 4729–4737.

[133] C. Lee, W. Yang and R. G. Parr, *Phys. Rev. B*, 1988, **37**, 785–789.

[134] A. D. Becke, *Phys. Rev. A*, 1988, **38**, 3098–3100.

[135] A. D. Becke, *J. Chem. Phys.*, 1996, **104**, 1040–1046.

[136] C. Adamo and V. Barone, *J. Chem. Phys.*, 1999, **110**, 6158–6170.

[137] E. Runge and E. K. U. Gross, *Phys. Rev. Lett.*, 1984, **52**, 997–1000.

[138] M. E. Casida, in *in Recent Advances in Density Functional Methods*, ed. D. E. Chong, World Scientific Singapore, 1998, pp. 152–192.

[139] S. Hirata and M. Head-Gordon, *Chem. Phys. Lett.*, 1999, **314**, 291–299.

[140] L. Noodleman and J. G. Norman, *J. Chem. Phys.*, 1979, **70**, 4903–4906.

[141] L. Noodleman and E. R. Davidson, *Chem. Phys.*, 1986, **109**, 131–143.

[142] K. Yamaguchi, H. Fukui and T. Fueno, *Chem. Lett.*, 1986, **15**, 625–628.

[143] P. A. Malmqvist, A. Rendell and B. O. Roos, *J. Phys. Chem.*, 1990, **94**, 5477–5482.

[144] K. Andersson, P.-Å. Malmqvist, B. O. Roos, A. J. Sadlej and K. Wolinski, *J. Phys. Chem.*, 1990, **94**, 5483–5488.

[145] V. Sauri, L. Serrano-Andrés, A. R. Moughal Shahi, L. Gagliardi, S. Vancoillie and K. Pierloot, *J. Chem. Theory Comput.*, 2011, **7**, 153–168.

[146] B. O. Roos and K. Andersson, *Chem. Phys. Lett.*, 1995, **245**, 215–223.

[147] N. Forsberg and P.-Å. Malmqvist, *Chem. Phys. Lett.*, 1997, **274**, 196–204.

[148] J. Miralles, J.-P. Daudey and R. Caballol, *Chem. Phys. Lett.*, 1992, **198**, 555–562.

[149] J. Miralles, O. Castell, R. Caballol and J.-P. Malrieu, *Chem. Phys.*, 1993, **172**, 33–43.

[150] N. Ben Amor and D. Maynau, *Chem. Phys. Lett.*, 1998, **286**, 211–220.

[151] S. F. Boys, *Quantum Theory of Atoms, Molecules and the Solid state*, New York: Academic Press, 2nd edn., 1966.

[152] J. Pipek and P. G. Mezey, *J. Chem. Phys.*, 1989, **90**, 4916–4926.

[153] D. Maynau, S. Evangelisti, N. Guihéry, C. J. Calzado and J.-P. Malrieu, *J. Chem. Phys.*, 2002, **116**, 10060–10068.

[154] A. Hauser, *J. Chem. Phys.*, 1991, **94**, 2741–2748.

[155] J.-F. Létard, *J. Mater. Chem.*, 2006, **16**, 2550–2559.

[156] M. A. Halcrow, *Chem. Soc. Rev.*, 2008, **37**, 278–289.

[157] C. Boilleau, N. Suaud and N. Guihéry, *J. Chem. Phys.*, 2012, **137**, 224304–224312.

[158] M. Kepenekian, B. Le Guennic and V. Robert, *J. Am. Chem. Soc.*, 2009, **131**, 11498–11502.

[159] D. Escudero and L. González, *J. Chem. Theory Comput.*, 2012, **8**, 203–213.

[160] L. M. Lawson Daku, A. Vargas, A. Hauser, A. Fouqueau and M. E. Casida, *ChemPhysChem*, 2005, **6**, 1393–1410.

[161] F. Weigend and R. Ahlrichs, *Phys. Chem. Chem. Phys.*, 2005, **7**, 3297–3305.

[162] C. Ochsenfeld, J. Gauss and R. Ahlrichs, *J. Chem. Phys.*, 1995, **103**, 7401–7407.

[163] A. Klamt and G. Schuurmann, *J. Chem. Soc., Perkin Trans. 2*, 1993, **0**, 799–805.

[164] M. Von Arnim and R. Ahlrichs, *J. Comput. Chem.*, 1998, **19**, 1746–1757.

[165] R. Ahlrichs, M. Bär, M. Häser, H. Horn and C. Kölmel, *Chem. Phys. Lett.*, 1989, **162**, 165–169.

[166] G. Karlström, R. Lindh, P.-Å. Malmqvist, B. O. Roos, U. Ryde, V. Veryazov, P.-O. Widmark, M. Cossi, B. Schimmelpfennig, P. Neogrady and L. Seijo, *Comput. Mater. Sci.*, 2003, **28**, 222–239.

[167] F. Aquilante, L. De Vico, N. Ferré, G. Ghigo, P.-Å. Malmqvist, P. Neogrady, T. B. Pedersen, M. Pitoňák, M. Reiher, B. O. Roos, L. Serrano-Andrés, M. Urban, V. Veryazov and R. Lindh, *J. Comput. Chem.*, 2010, **31**, 224–247.

[168] B. O. Roos, R. Lindh, P.-Å. Malmqvist, V. Veryazov and P.-O. Widmark, *J. Phys. Chem. A*, 2004, **108**, 2851–2858.

[169] B. O. Roos, R. Lindh, P.-Å. Malmqvist, V. Veryazov and P.-O. Widmark, *J. Phys. Chem. A*, 2005, **109**, 6575–6579.

[170] F. Aquilante, T. B. Pedersen and R. Lindh, *J. Chem. Phys.*, 2007, **126**, 194106–194116.

[171] F. Aquilante, P.-Å. Malmqvist, T. B. Pedersen, A. Ghosh and B. O. Roos, *J. Chem. Theory Comput.*, 2008, **4**, 694–702.

[172] B. A. Hess, *Phys. Rev. A*, 1986, **33**, 3742–3748.

[173] P.-Å. Malmqvist, B. O. Roos and B. Schimmelpfennig, *Chem. Phys. Lett.*, 2002, **357**, 230–240.

[174] B. O. Roos and P.-A. Malmqvist, *Phys. Chem. Chem. Phys.*, 2004, **6**, 2919–2927.

[175] K. Pierloot and S. Vancoillie, *J. Chem. Phys.*, 2006, **125**, 124303–124311.

[176] M. Álvarez-Moreno, C. de Graaf, N. López, F. Maseras, J. M. Poblet and C. Bo, *J. Chem. Inf. Model.*, 2015, **55**, 95–103.

[177] M. Cossi, G. Scalmani, N. Rega and V. Barone, *J. Chem. Phys.*, 2002, **117**, 43–54.

[178] S. Miertuš, E. Scrocco and J. Tomasi, *Chem. Phys.*, 1981, **55**, 117–129.

[179] R. Cammi and J. Tomasi, *J. Comput. Chem.*, 1995, **16**, 1449–1458.

[180] C. Angeli, R. Cimiraglia and J.-P. Malrieu, *J. Chem. Educ.*, 2008, **85**, 150–158.

[181] C. Angeli, C. J. Calzado, C. de Graaf and R. Caballol, *Phys. Chem. Chem. Phys.*, 2011, **13**, 14617–14628.

[182] A. Sadoc, R. Broer and C. de Graaf, *J. Chem. Phys.*, 2007, **126**, 134709–134717.

[183] S. Nozawa, T. Sato, M. Chollet, K. Ichiyanagi, A. Tomita, H. Fujii, S. Adachi and S. Koshihara, *J. Am. Chem. Soc.*, 2010, **132**, 61–63.

[184] M. Swart, *J. Chem. Theory Comput.*, 2008, **4**, 2057–2066.

[185] B. Ordejón, C. de Graaf and C. Sousa, *J. Am. Chem. Soc.*, 2008, **130**, 13961–13968.

[186] N. Suaud, M.-L. Bonnet, C. Boilleau, P. Labèguerie and N. Guihéry, *J. Am. Chem. Soc.*, 2009, **131**, 715–722.

[187] A. Domingo, M. A. Carvajal and C. de Graaf, *Int. J. Quantum Chem.*, 2010, **110**, 331–337.

[188] M.-E. Moret, I. Tavernelli, M. Chergui and U. Rothlisberger, *Chem. Eur. J.*, 2010, **16**, 5889–5894.

[189] A. Domingo, A. Rodríguez-Fortea and C. de Graaf, *J. Chem. Theory Comput.*, 2012, **8**, 235–244.

[190] A. Domingo, C. Sousa and C. de Graaf, *Dalton Trans.*, 2014, **43**, 17838–17846.

[191] M. Swart and M. Costas, *Spin States in Biochemistry and Inorganic Chemistry: Influence on Structure and Reactivity*, Wiley, Chichester, United Kingdom, 2016.

[192] P. J. van Koningsbruggen, Y. Maeda and H. Oshio, in *Spin crossover in Transition Metal Compounds I*, ed. P. Gütlich and H. A. Goodwin, Springer-Verlag, 2004, vol. 233, pp. 233–259.

[193] S. Hayami, Z.-z. Gu, M. Shiro, Y. Einaga, A. Fujishima and O. Sato, *J. Am. Chem. Soc.*, 2000, **122**, 7126–7127.

[194] G. Juhász, S. Hayami, O. Sato and Y. Maeda, *Chem. Phys. Lett.*, 2002, **364**, 164–170.

[195] S. Hayami, K. Hiki, T. Kawahara, Y. Maeda, D. Urakami, K. Inoue, M. Ohama, S. Kawata and O. Sato, *Chem. Eur. J.*, 2009, **15**, 3497–3508.

[196] T. Shimizu, Y. Komatsu, H. Kamihata, Y. Lee, A. Fuyuhiro, S. Iijima and S. Hayami, *J. Incl. Phenom. Macrocycl. Chem.*, 2011, **71**, 363–369.

[197] M. Clemente-León, E. Coronado, M. López-Jordà, J. C. Waerenborgh, C. Desplanches, H. Wang, J.-F. Létard, A. Hauser and A. Tissot, *J. Am. Chem. Soc.*, 2013, **135**, 8655–8667.

[198] K. D. Murnaghan, C. Carbonera, L. Toupet, M. Griffin, M. M. Dîrtu, C. Desplanches, Y. Garcia, E. Collet, J.-F. Létard and G. G. Morgan, *Chem. Eur. J.*, 2014, **20**, 5613–5618.

[199] C. Consani, M. Premont-Schwarz, A. ElNahhas, C. Bressler, F. van Mourik, A. Cannizzo and M. Chergui, *Angew. Chem. Int. Ed.*, 2009, **48**, 7184–7187.

[200] N. Huse, H. Cho, K. Hong, L. Jamula, F. M. F. de Groot, T. K. Kim, J. K. McCusker and R. W. Schoenlein, *J. Phys. Chem. Lett.*, 2011, **2**, 880–884.

[201] W. Zhang, R. Alonso-Mori, U. Bergmann, C. Bressler, M. Chollet, A. Galler, W. Gawelda, R. G. Hadt, R. W. Hartsock, T. Kroll, K. S. Kjær, K. Kubiček, H. T. Lemke, H. W. Liang, D. A. Meyer, M. M. Nielsen, C. Purser, J. S. Robinson, E. I. Solomon, Z. Sun, D. Sokarasa, T. B. van Driel, G. Vankó, T.-C. Weng, D. Zhu and K. J. Gaffney, *Nature*, 2014, **509**, 345–348.

[202] J. K. McCusker, K. N. Walda, R. C. Dunn, J. D. Simon, D. Magde and D. N. Hendrickson, *J. Am. Chem. Soc.*, 1993, **115**, 298–307.

[203] E. W. T. Yemeli, G. R. Blake, A. P. Douvalis, T. Bakas, G. O. R. Alberda van Ekenstein and P. J. van Koningsbruggen, *Chem. Eur. J.*, 2010, doi: 10.1002/chem.201002100.

[204] H. Ando, Y. Nakao, H. Sato and S. Sakaki, *J. Phys. Chem. A*, 2007, **111**, 5515–5522.

[205] M. Etinski, J. Tatchen and C. M. Marian, *J. Chem. Phys.*, 2011, **134**, 154105–154113.

[206] K. P. Kepp, *Coord. Chem. Rev.*, 2013, **257**, 196–209.

[207] F. Neese, *WIREs Comput. Mol. Sci.*, 2012, **2**, 73–78.

[208] R. Izsak and F. Neese, *J. Chem. Phys.*, 2011, **135**, 144105–144115.

[209] T. Petrenko, S. Kossmann and F. Neese, *J. Chem. Phys.*, 2011, **134**, 054116–054129.

[210] O. Treutler and R. Ahlrichs, *J. Chem. Phys.*, 1995, **102**, 346–354.

[211] F. Furche, R. Ahlrichs, C. Hättig, W. Klopper, M. Sierka and F. Weigend, *WIREs Comput. Mol. Sci.*, 2014, **1**, 91–100.

[212] *TURBOMOLE V6.6 2014, a development of University of Karlsruhe and Forschungszentrum Karlsruhe GmbH, 1989-2007, TURBOMOLE GmbH, since 2007; available from* `http://www.turbomole.com`.

[213] P.-Å. Malmqvist and B. O. Roos, *Chem. Phys. Lett.*, 1989, **155**, 189–194.

[214] M. Kepenekian, V. Robert, B. Le Guennic and C. de Graaf, *J. Comput. Chem.*, 2009, **30**, 2327–2333.

[215] A. Bousseksou, J. J. McGarvey, F. Varret, J.-A. Real, J.-P. Tuchagues, A. C. Dennis and M.-L. Boillot, *Chem. Phys. Lett.*, 2000, **318**, 409–416.

[216] S. Hayami, Z.-z. Gu, H. Yoshiki, A. Fujishima and O. Sato, *J. Am. Chem. Soc.*, 2001, **123**, 11644–11650.

[217] P. Gütlich, H. Köppen, R. Link and H. G. Steinhäuser, *J. Chem. Phys.*, 1979, **70**, 3977–3983.

[218] R. Boča and W. Linert, *Monatsh Chem.*, 2003, **134**, 199–216.

[219] J. Cirera and F. Paesani, *Inorg. Chem.*, 2012, **51**, 8194–8201.

[220] A. Rudavskyi, C. Sousa, C. de Graaf, R. W. A. Havenith and R. Broer, *J. Chem. Phys.*, 2014, **140**, 184318–184325.

[221] S. Alvarez, D. Avnir, M. Llunell and M. Pinsky, *New J. Chem.*, 2002, **26**, 996–1009.

[222] S. Alvarez, *J. Am. Chem. Soc.*, 2003, **125**, 6795–6802.

[223] S. Saureu and C. de Graaf, *Chem. Phys.*, 2014, **428**, 59–66.

[224] L. M. Lawson Daku, F. Aquilante, T. W. Robinson and A. Hauser, *J. Chem. Theory Comput.*, 2012, **8**, 4216–4231.

[225] M. F. Tweedle and L. J. Wilson, *J. Am. Chem. Soc.*, 1976, **98**, 4824–4834.

[226] S. Schenker, A. Hauser and R. M. Dyson, *Inorg. Chem.*, 1996, **35**, 4676–4682.

[227] A. Domingo, C. Sousa and C. de Graaf, *Dalton Trans.*, 2014, **43**, 17838–17846.

[228] S. Iuchi and N. Koga, *J. Chem. Phys.*, 2014, **140**, 024309–024319.

[229] B. A. Hess, C. M. Marian, U. Wahlgren and O. Gropen, *Chem. Phys. Lett.*, 1996, **251**, 365–371.

[230] S. Mai, P. Marquetand and L. González, *Int. J. Quantum Chem.*, 2015, **115**, 1215–1231.

[231] C. Daniel, *Coord. Chem. Rev.*, 2015, **282-283**, 19–32.

[232] C. Gourlaouen, J. Eng, M. Otsuka, E. Gindensperger and C. Daniel, *J. Chem. Theory Comput.*, 2015, **11**, 99–110.

[233] G. Capano, T. J. Penfold, U. Röthlisberger and I. Tavernelli, *Chimia*, 2014, **68**, 227–230.

[234] G. Capano, U. Rothlisberger, I. Tavernelli and T. J. Penfold, *J. Phys. Chem. A*, 2015, **119**, 7026–7037.

[235] L. Yu, C. Xu, Y. Lei, C. Zhu and Z. Wen, *Phys. Chem. Chem. Phys.*, 2014, **16**, 25883–25895.

[236] W. Ouyang, W. Dou and J. E. Subotnik, *J. Chem. Phys.*, 2015, **142**, 084109–084121.

[237] J. Dawson, *Science*, 1988, **240**, 433–439.

[238] M. T. Green, J. H. Dawson and H. B. Gray, *Science*, 2004, **304**, 1653–1656.

[239] P. R. O. de Montellano, *Cytochrome P450: Structure, Mechanism, and Biochemistry*, Springer International Publishing, 2005.

[240] J. Rittle and M. T. Green, *Science*, 2010, **330**, 933–937.

[241] D. Garfinkel, *Arch Biochem Biophys.*, 1958, **77**, 493–509.

[242] M. Klingenberg, *Arch Biochem Biophys.*, 1958, **75**, 376–386.

[243] T. Omura and R. Sato, *J Biol Chem.*, 1964, **239**, 2370–2378.

[244] Z. Gross and S. Nimri, *Inorg. Chem.*, 1994, **33**, 1731–1732.

[245] J. T. Groves, Z. Gross and M. K. Stern, *Inorg. Chem.*, 1994, **33**, 5065–5072.

[246] T. Ohno, N. Suzuki, T. Dokoh, Y. Urano, K. Kikuchi, M. Hirobe, T. Higuchi and T. Nagano, *J. Inorg. Biochem.*, 2000, **82**, 123–125.

[247] Y. Kang, H. Chen, Y. J. Jeong, W. Lai, E. H. Bae, S. Shaik and W. Nam, *Chem. Eur. J.*, 2009, **15**, 10039–10046.

[248] C. M. Krest, E. L. Onderko, T. H. Yosca, J. C. Calixto, R. F. Karp, J. Livada, J. Rittle and M. T. Green, *J. Biol. Chem.*, 2013, **288**, 17074–17081.

[249] A. B. McQuarters, M. W. Wolf, A. P. Hunt and N. Lehnert, *Angew. Chem. Int. Ed.*, 2014, **53**, 4750–4752.

[250] M. M. Palcic, R. Rutter, T. Araiso, L. P. Hager and H. Dunford, *Biochem. Biophys. Res. Commun.*, 1980, **94**, 1123–1127.

[251] R. Rutter, L. P. Hager, H. Dhonau, M. Hendrich, M. Valentine and P. Debrunner, *Biochemistry*, 1984, **23**, 6809–6816.

[252] T. Egawa, D. A. Proshlyakov, H. Miki, R. Makino, T. Ogura, T. Kitagawa and Y. Ishimura, *J. Biol. Inorg. Chem.*, 2001, **6**, 46–54.

[253] K. L. Stone, R. K. Behan and M. T. Green, *Proc. Natl. Acad. Sci. U. S. A.*, 2005, **102**, 16563–16565.

[254] G. H. Loew and Z. S. Herman, *J. Am. Chem. Soc.*, 1980, **102**, 6173–6174.

[255] D. L. Harris and G. H. Loew, *J. Am. Chem. Soc.*, 1998, **120**, 8941–8948.

[256] G. H. Loew, and D. L. Harris, *Chem. Rev.*, 2000, **100**, 407–420.

[257] G. Loew, *Int. J. Quantum Chem.*, 2000, **77**, 54–70.

[258] D. Harris, G. Loew and L. Waskell, *J. Inorg. Biochem.*, 2001, **83**, 309–318.

[259] M. T. Green, *J. Am. Chem. Soc.*, 1999, **121**, 7939–7940.

[260] F. Ogliaro, S. Cohen, M. Filatov, N. Harris and S. Shaik, *Angew. Chem. Int. Ed.*, 2000, **39**, 3851–3855.

[261] T. Ohta, K. Matsuura, K. Yoshizawa and I. Morishima, *J. Inorg. Biochem.*, 2000, **82**, 141–152.

[262] S. P. de Visser, F. Ogliaro, N. Harris and S. Shaik, *J. Am. Chem. Soc.*, 2001, **123**, 3037–3047.

[263] M. Radoń and E. Broclawik, *J. Chem. Theory Comput.*, 2007, **3**, 728–734.

[264] S. Vancoillie, H. Zhao, M. Radoń and K. Pierloot, *J. Chem. Theory Comput.*, 2010, **6**, 576–582.

[265] M. Radoń, E. Broclawik and K. Pierloot, *J. Chem. Theory Comput.*, 2011, **7**, 898–908.

[266] S. Shaik, D. Kumar, S. P. de Visser, A. Altun, and W. Thiel, *Chem. Rev.*, 2005, **105**, 2279–2328.

[267] M. Ghiasi, M. Tafazzoli and N. Safari, *J. Mol. Struct.*, 2007, **820**, 18–25.

[268] H. Chen, J. Song, W. Lai, W. Wu and S. Shaik, *J. Chem. Theory Comput.*, 2010, **6**, 940–953.

[269] S. Shaik, S. Cohen, Y. Wang, H. Chen, D. Kumar and W. Thiel, *Chem. Rev.*, 2010, **110**, 949–1017.

[270] J. E. Elenewski and J. C. Hackett, *J. Chem. Phys.*, 2012, **137**, 124311–124323.

[271] J. E. Elenewski and J. C. Hackett, *J. Comput. Chem.*, 2013, **34**, 1647–1660.

[272] C. M. Krest, A. Silakov, J. Rittle, T. H. Yosca, E. L. Onderko, J. C. Calixto and M. T. Green, *Nat. Chem.*, 2015, **7**, 696–702.

[273] P.-Å. Malmqvist, K. Pierloot, A. R. Moughal Shahi, C. J. Cramer and L. Gagliardi, *J. Chem. Phys.*, 2008, **128**, 204109–204118.

[274] C. J. Calzado, S. Evangelisti and D. Maynau, *J. Phys. Chem. A*, 2003, **107**, 7581–7588.

[275] J. Pitarch-Ruiz, S. Evangelisti and D. Maynau, *Int. J. Quantum Chem.*, 2005, **101**, 325–333.

[276] S. Hoyau, D. Maynau and J.-P. Malrieu, *J. Chem. Phys.*, 2011, **134**, 054125–054136.

[277] J.-P. Malrieu, N. Guihéry, C. J. Calzado and C. Angeli, *J. Comput. Chem.*, 2007, **28**, 35–50.

[278] C. J. Calzado, C. Angeli, D. Taratiel, R. Caballol and J.-P. Malrieu, *J. Chem. Phys.*, 2009, **131**, 044327–044340.

[279] J. Zapata-Rivera, R. Caballol and C. J. Calzado, *Phys. Chem. Chem. Phys.*, 2011, **13**, 20241–20247.

[280] A. Domingo, D. Specklin, V. Rosa, S. Mameri, V. Robert and R. Welter, *Eur. J. Inorg. Chem.*, 2014, **2014**, 2552–2560.

[281] A. Domingo, C. Angeli, C. de Graaf and V. Robert, *J. Comput. Chem.*, 2015, **36**, 861–869.

[282] S. Saureu and C. de Graaf, *Phys. Chem. Chem. Phys.*, 2016, **18**, 1233–1244.

[283] J. Terner, V. Palaniappan, A. Gold, R. Weiss, M. M. Fitzgerald, A. M. Sullivan and C. M. Hosten, *J. Inorg. Biochem.*, 2006, **100**, 480–501.

[284] T. Egawa, H. Miki, T. 0gura, R. Makino, Y. Ishimura and T. Kitagawa, *FEBS Lett.*, 1992, **305**, 206–208.

[285] F. Banse, J.-J. Girerd and V. Robert, *Eur. J. Inorg. Chem.*, 2008, **2008**, 4786–4791.

[286] C. de Graaf and C. Sousa, *Int. J. Quantum Chem.*, 2006, **106**, 2470–2478.

[287] K. Yamaguchi, Y. Takahara, T. Fueno and K. N. Houk, *Theor. Chim. Acta*, 1988, **73**, 337–364.

[288] C. Herring, in *Magnetism*, ed. G. T. Rado and H. Suhl, Academic Press, New York, 1963, vol. IIB, pp. 1–181.

[289] H. Tamaki, Z. J. Zhong, N. Matsumoto, S. Kida, M. Koikawa, N. Achiwa, Y. Hashimoto and H. Okawa, *J. Am. Chem. Soc.*, 1992, **114**, 6974–6979.

[290] M. Gruselle, C. Train, K. Boubekeur, P. Gredin and N. Ovanesyan, *Coord. Chem. Rev.*, 2006, **250**, 2491–2500.

[291] C. Train, R. Gheorghe, V. Krstic, L.-M. Chamoreau, N. S. Ovanesyan, G. L. J. A. Rikken, M. Gruselle and M. Verdaguer, *Nat. Mater.*, 2008, **7**, 729–734.

[292] C. Train, T. Nuida, R. Gheorghe, M. Gruselle and S. ichi Ohkoshi, *J. Am. Chem. Soc.*, 2009, **131**, 16838–16843.

[293] A. Alberola, E. Coronado, C. Giménez-Saiz, C. J. Gómez-García, F. M. Romero and A. Tarazón, *Eur. J. Inorg. Chem.*, 2005, **2005**, 389–400.

[294] D. Armentano, G. De Munno, F. Lloret and M. Julve, *CrystEngComm*, 2005, **7**, 57–66.

[295] H. Okawa, A. Shigematsu, M. Sadakiyo, T. Miyagawa, K. Yoneda, M. Ohba and H. Kitagawa, *Journal of the American Chemical Society*, 2009, **131**, 13516–13522.

[296] E. Pardo, C. Train, G. Gontard, K. Boubekeur, O. Fabelo, H. Liu, B. Dkhil, F. Lloret, K. Nakagawa, H. Tokoro, S. ichi Ohkoshi and M. Verdaguer, *J. Am. Chem. Soc.*, 2011, **133**, 15328–15331.

[297] E. Pardo, C. Train, H. Liu, L.-M. Chamoreau, B. Dkhil, K. Boubekeur, F. Lloret, K. Nakatani, H. Tokoro, S.-i. Ohkoshi and M. Verdaguer, *Angew. Chem. Int. Ed.*, 2012, **51**, 8356–8360.

[298] C. Maxim, S. Ferlay, H. Tokoro, S.-I. Ohkoshi and C. Train, *Chem. Commun.*, 2014, **50**, 5629–5632.

[299] C. Maxim, S. Ferlay and C. Train, *New J. Chem.*, 2011, **35**, 1254–1259.

[300] E. Pardo, C. Train, R. Lescouezec, K. Boubekeur, E. Ruiz, F. Lloret and M. Verdaguer, *Dalton Trans.*, 2010, **39**, 4951–4958.

[301] E. Pardo, C. Train, K. Boubekeur, G. Gontard, J. Cano, F. Lloret, K. Nakatani and M. Verdaguer, *Inorg. Chem.*, 2012, **51**, 11582–11593.

[302] E. Coronado, J. R. Galan-Mascaros, C. Marti-Gastaldo and A. M. Martinez, *Dalton Trans.*, 2006, 3294–3299.

[303] S. Ferlay and M. W. Hosseini, *Molecular Tectonics: Design of Hybrid Networks and Crystals Based on Charge-Assisted Hydrogen Bonds*, WILEY-VCH Verlag, 2011, pp. 195–232.

[304] C. Paraschiv, S. Ferlay, M. W. Hosseini, V. Bulach and J.-M. Planeix, *Chem. Commun.*, 2004, 2270–2271.

[305] P. Dechambenoit, S. Ferlay, B. Donnio, D. Guillon and M. W. Hosseini, *Chem. Commun.*, 2011, **47**, 734–736.

[306] G. Marinescu, S. Ferlay, N. Kyritsakas and M. W. Hosseini, *Chem. Commun.*, 2013, **49**, 11209–11211.

[307] J. H. Wachters and W. C. Niewpoort, in *Selected Topics Molecular Physics*, ed. E. Clementi, Verlag Chemie, Weinheim, 1972, p. 135.

[308] I. Negodaev, C. de Graaf, R. Caballol and V. Lukov, *Inorg. Chim. Acta*, 2011, **375**, 166–172.

[309] I. Negodaev, N. Queralt, R. Caballol and C. de Graaf, *Chem. Phys.*, 2011, **379**, 109–115.

[310] E. Coronado, J. R. Galán-Mascarós, C. Giménez-Saiz, C. J. Gómez-García and C. Ruiz-Pérez, *Eur. J. Inorg. Chem.*, 2003, **2003**, 2290–2298.

[311] C. J. Calzado, J. Cabrero, J.-P. Malrieu and R. Caballol, *J. Chem. Phys.*, 2002, **116**, 2728–2747.

[312] C. J. Calzado, J. Cabrero, J.-P. Malrieu and R. Caballol, *J. Chem. Phys.*, 2002, **116**, 3985–4000.

[313] J.-B. Rota, L. Norel, C. Train, N. B. Amor, D. Maynau and V. Robert, *J. Am. Chem. Soc.*, 2008, **130**, 10380–10385.

[314] J.-B. Rota, C. J. Calzado, C. Train and V. Robert, *J. Chem. Phys.*, 2010, **132**, 154702–154707.

[315] J. Miralies, R. Caballol and J.-P. Malrieu, *Chem. Phys.*, 1991, **153**, 25–37.

[316] M. Mödl, M. Dolg, P. Fulde and H. Stoll, *J. Chem. Phys.*, 1996, **105**, 2353–2363.

[317] D. Taratiel, J. Cabrero, C. de Graaf and R. Caballol, *Polyhedron*, 2003, **22**, 2409–2414.

[318] R. Bastardis, N. Guihéry and C. de Graaf, *J. Chem. Phys.*, 2008, **129**, 104102–104108.

[319] Z. Tabookht, X. López, M. Bénard and C. de Graaf, *J. Phys. Chem. A*, 2010, **114**, 12291–12298.

[320] R. Bastardis, N. Guihéry and C. de Graaf, *Phys. Rev. B*, 2007, **76**, 132412–132415.

[321] M. Kepenekian, B. Le Guennic and V. Robert, *Phys. Rev. B*, 2009, **79**, 094428–094432.

[322] B. L. Guennic, N. B. Amor, D. Maynau and V. Robert, *J. Chem. Theory Comput.*, 2009, **5**, 1506–1510.

[323] J. Bailar and E. Jones, *Inorg. Synth.*, 1939, **1**, 35–28.

[324] P. Dechambenoit, S. Ferlay, N. Kyritsakas and M. W. Hosseini, *J. Am. Chem. Soc.*, 2008, **130**, 17106–17113.

[325] P. Dechambenoit, S. Ferlay, N. Kyritsakas and M. W. Hosseini, *New J. Chem.*, 2010, **34**, 1184–1199.

[326] G. M. Sheldrick, *Programs for the Refinement of Crystal Structures*, University of Göttingen, 1996.

[327] D. Casanova, P. Alemany, J. M. Bofill and S. Alvarez, *Chem. Eur. J.*, 2003, **9**, 1281–1295.

[328] M. D. Ward, *Chem. Commun.*, 2005, 5838–5842.

[329] A. Herpin and L. Néel, *Théorie du magnétisme*, Saclay : Institut national des sciences et techniques nucléaires ; Paris : Presses universitaires de France, 1968.

[330] S.-I. Ohkoshi and K. Hashimoto, *Phys. Rev. B*, 1999, **60**, 12820–12825.

[331] M. Julve, M. Verdaguer, A. Gleizes, M. Philoche-Levisalles and O. Kahn, *Inorg. Chem.*, 1984, **23**, 3808–3818.

[332] L. Atovmyan, G. Shilov, R. Lubovskaya, E. Zhilyaeva, N. Ovanesyan, S. Pirumova, I. Gusakovskaya and Y. Morozov, *JETP Lett.*, 1993, **58**, 766–769.

“Science is a way of life. Science is a perspective. Science is the process that takes us from confusion to understanding in a manner that’s precise, predictive and reliable —a transformation, for those lucky enough to experience it, that is empowering and emotional.”

— Brian Greene